University of Alberta
Department of Civil Engineering

Structural Engineering Report No. 146

POSTBUCKLING BEHAVIOR OF THIN STEEL CYLINDERS UNDER TRANSVERSE SHEAR

By

V. G. ROMAN
and
A. E. ELWI

May 1987

RECENT STRUCTURAL ENGINEERING REPORTS

Department of Civil Engineering

University of Alberta

115. *End Connection Effects on the Strength of Concrete Filled HSS Columns* by S.J. Kennedy and J.G. MacGregor, April 1984.

116. *Reinforced Concrete Column Design Program* by C-K. Leung and S.H. Simmonds, April 1984.

117. *Deflections of Two-way Slabs under Construction Loading* by C. Graham and A. Scanlon, August 1984.

118. *Effective Lengths of Laterally Unsupported Steel Beams* by C.D. Schmitke and D.J.L. Kennedy, October 1984.

119. *Flexural and Shear Behaviour of Large Diameter Steel Tubes* by R.W. Bailey and G.L. Kulak, November 1984.

120. *Concrete Masonry Prism Response due to Loads Parallel and Perpendicular to Bed Joints* by R. Lee, J. Longworth and J. Warwaruk.

121. *Standardized Flexible End Plate Connections for Steel Beams* by G.J. Kriviak and D.J.L. Kennedy, December 1984.

122. *The Effects of Restrained Shrinkage on Concrete Slabs* by K.S.S. Tam and A. Scanlon, December 1984.

123. *Prestressed Concrete Beams with Large Rectangular Web Openings* by T. do M.J. Alves and A. Scanlon, December 1984.

124. *Tests on Eccentrically Loaded Fillet Welds* by G.L. Kulak and P.A. Timler, December 1984.

125. *Analysis of Field Measured Deflections Scotia Place Office Tower* by A. Scanlon and E. Ho, December 1984.

126. *Ultimate Behaviour of Continuous Deep Reinforced Concrete Beams* by D.R. Ricketts and J.G. MacGregor, January 1985.

127. *The Interaction of Masonry Veneer and Steel Studs in Curtain Wall Construction* by W.M. McGinley, J. Warwaruk, J. Longworth and M. Hatzinikolas, May 1985.

128. *Evaluation of Existing Bridge Structure by Nondestructive Test Methods* by L. Mikhailovsky and A. Scanlon, May 1985.

129. *Finite Element Modelling of Buried Structures* by D.K. Playdon and S.H. Simmonds, October 1985.

130. *Behaviour and Ultimate Strength of Transversely Loaded Continuous Steel Plates* by K.P. Ratzlaff and D.J.L. Kennedy, November 1985.

131. *Inelastic Lateral Buckling of Steel Beam-Columns* by P.E. Cuk, M.A. Bradford and N.S. Trahair, December 1985.

132. *Design Strengths of Steel Beam-Columns* by N.S. Trahair, December 1985.

133. *Behaviour of Fillet Welds as a Function of the Angle of Loading* by G.S. Miazga and D.J.L. Kennedy, March 1986.

134. *Inelastic Seismic Response of Precast Concrete Large Panel Coupled Shear Wall Systems* by M.R. Kianoush and A. Scanlon, March 1986.

135. *Finite Element Prediction of Bin Loads* by A.H. Askari and A.E. Elwi, June 1986.

136. *Shear Behavior of Large Diameter Fabricated Steel Cylinders* by J. Mok and A.E. Elwi, June 1986.

137. *Local Buckling Rules for Structural Steel Members* by S. Bild and G.L. Kulak, May 1986.

138. *Finite Element Prediction of Reinforced Concrete Behavior* by S. Balakrishnan and D.W. Murray, July 1986.

139. *Behavior and Strength of Masonry Wall/Slab Joints* by T.M. Olatunji and J. Warwaruk, July 1986.

140. *Bayesian Analysis of In-Situ Test Data for Estimating the Compressive Strength of Concrete in Existing Structures* by G.J. Kriviak and A. Scanlon, July 1986.

141. *Shear-Moment Transfer in Slab-Column Connections* by S.D.B. Alexander and S.H. Simmonds, July 1986.

142. *Minimum Thickness Requirements for Deflection Control of Two-Way Slab Systems* by D.P. Thompson and A. Scanlon, November 1986.

143. *Shrinkage and Flexural Tests of Two Full-Scale Composite Trusses* by A. Brattland and D.J.L. Kennedy, December 1986.

144. *Combined Flexure and Torsion of I-Shaped Steel Beams* by R.G. Driver and D.J.L. Kennedy, March 1987.

145. *Cyclic and Static Behaviour of Thin Panel Steel Plate Shear Walls* by E.W. Tromposch and G.L. Kulak, April 1987.

146. *Postbuckling Behavior of Thin Steel Cylinders Under Transverse Shear* by V.G. Roman and A.E. Elwi, May 1987.

POSTBUCKLING BEHAVIOR OF THIN STEEL CYLINDERS UNDER TRANSVERSE SHEAR

by

V.G. ROMAN

A.E. ELWI

Structural Engineering Report No. 146

Department of Civil Engineering

University of Alberta

Edmonton, Alberta, Canada

May 1987

ABSTRACT

The behavior of thin steel cylinders under transverse shear is investigated using a 16-node three dimensional degenerated plate shell element in the context of the nonlinear finite element analysis program NISA80, with an elastic-perfectly plastic material model.

The analysis is carried out along the prebuckling and the postbuckling equilibrium paths for cylinders with initial measured imperfections, initial residual stresses due to longitudinal seam weld shrinkage and initial locked-in stresses due to the cold forming.

The presence of an ultimate strength plastic mechanism in the postbuckling range is investigated. The ultimate strength mechanism is analogous to a truss panel with the diagonal fully yielded. The top and bottom parts of the cylinder are the chords of the truss panel and the tension field is the diagonal. An analytical theory for the tension field contribution to the total shear is developed. An upper and a lower bound are defined for the extent of the development of the tension field on the cylinder under transverse shear as well as the effect of cross bending moments within the buckles.

ACKNOWLEDGEMENTS

This study was funded under the Natural Sciences and Engineering Research Council of Canada Operating Grant No. A5877. The authors wish to express their gratitude to D. Nickel for drafting the figures and to P.M. Collins for permission to use program SAPMESH.

Table of Contents

List of Tables

List of Figures

LIST OF SYMBOLS

a	:	measure of postbuckling asymmetric response
b	:	measure of the imperfection sensitivity of the postbuckling response, or axial or circumferential dimension of a panel under transverse shear
C, dC	:	horizontal projection and elementary horizontal projection of the tension field
C_T, C_B	:	forces in top or bottom chords of a truss panel
D	:	$\frac{Et^3}{12(1-\nu^2)}$ flexural stiffness of a plate per unit length
E	:	modulus of elasticity
I_y	:	moment of inertia around y axis of a cross section
K	:	empirical constant in the power law relationship between the true stress and the true strain
k_s	:	Batdorf's coefficient
L	:	length of cylinder or truss panel
M	:	bending moment
M_R, M_L	:	bending moments at the ends of a truss panel calculated for an equivalent beam.
M_y^*	:	apparent shrinkage moment
n	:	empirical constant in the power law relationship between the true stress and the true strain

P_c	:	classical buckling load
P_x^*	:	apparent shrinkage force
R	:	radius
R_0	:	die radius plus half thickness of sheet
R_f	:	radius of curvature of sheet mid-section after springback
T	:	tension force of a diagonal in a truss panel
t	:	shell thickness
V	:	total shear force
V_t, dV_t	:	shear and elementary shear due to the tension field
dW	:	elementary width of the tension field
Z	:	Batdorf's curvature parameter for a curved panel
α	:	thermal expansion coefficient or angle
γ	:	angle of top or bottom chord with a horizontal line
δ	:	buckling mode amplitude
$\bar{\delta}$	:	amplitude of the imperfection described by a buckling mode shape
ϵ_s, ϵ_r	:	strains in the s and r directions
ϵ_{smax}	:	maximum strain in the s direction
ϵ_{sy}	:	strain at yield in the s direction
$\epsilon_x^{"}$	:	incompatible strain in the x direction
ζ	:	angle of a diagonal of a truss panel with a horizontal line or angle of the tension field measured on the cylinder surface

η	:	factor to account for the variation of the tension stress across the tension field width
χ	:	angle related to the helix shape of the tension strips
μ	:	factor to account for the cross bending moment effect
ν	:	Poisson's ratio
σ_r, σ_s	:	stresses in the r and s directions
σ_b	:	stress due to the bending moments
σ_{max}	:	maximum stress
σ_{ry}	:	yield stress in the r direction
σ_{sy}	:	yield stress in the s direction
σ_t	:	tension stress across the tension field width
σ_{t1}, σ_{t2}	:	average yield stresses across the tension bands
σ_{t3}	:	average yield stress across the tension bands
σ_x	:	stress in the x direction
σ_y	:	static yield stress
τ_{cr}	:	critical shear stress
τ_p	:	critical plastic shear stress
τ_y	:	shear yield stress
ϕ, $d\phi$	:	angle and elementary angle corresponding to an elementary width of the tension field

1. Introduction

1.1 Background

The use of fabricated thin walled tubular steel members and structures is growing in civil engineering applications. Structural specifications do not give complete design information on the buckling of these members. This study focuses on one particular aspect which is the behavior of these shell structures under transverse shear. Tests on the shear behavior of large diameter fabricated steel tubes were carried out by Bailey and Kulak(1984). Numerical investigation of the behavior of cylinders under transverse shear was initiated by Mok and Elwi(1986). The study reported, herein, is a continuation of the numerical investigation. This phase focuses on the effects of the measured imperfections, residual stresses and locked-in stresses on the critical loads and on the response of the shell in the pre- and postbuckling ranges.

1.2 Stability Concepts of Shells

Since the 1800's a large effort has been dedicated to the study of thin cylindrical shells. Lorentz(1911) presented a solution for axially loaded cylinders. Southwell (1913) and Von Mises(1914) published solutions for buckling of cylinders under uniform lateral pressure. In 1932, Flügge developed a treatment of cylindrical shells under axial loading, pure bending and combined loading. Response to

torsion was studied by Schwerrin (1925) and Donnell(1933).

Bushnell(1985) gives an extended description of the instabilty phenomena related to shells. A general feature of thin shells is that because of the curvature, the membrane stiffness is much larger than the bending stiffness. Shell action implies that most of the strain is due to membrane compression. Shell failure by buckling is attributed to loss of membrane carrying capacity. The process results in large deflection patterns called buckling configurations.

The behavior of a structure is well described by the load-deflection plots which are obtained by increasing the external load slowly from zero. Each point represents an equilibrium configuration of the structure. Load deflection plots are representations of the stucture's equilibrium path, Fig. 1.1. The point on the equilibrium path at which the load is a relative maximum is a limit point and the point at which two or more equilibrium paths intersect is called a bifurcation point.

At early stages of loading a geometrically perfect structure is in a prebuckled state of equilibrium characterized by a single primary path on a load displacement plot (Fig. 1.1b). With the increase of loading the structure reaches a bifurcation point after which it follows the secondary path because the primary path is no longer stable. The nature of the equilibrium on the secondary path is described by the stiffness. Depending upon whether the stiffness is positive or negative the equilbrium

is stable or unstable, respectively, and if the stiffness is zero the equilibrium is neutral.

Prior to and at bifurcation the displacements are relatively small and a theory based on infinitesimal displacements is usually appropriate to predict the behavior up to and including the bifurcation point.

If the primary equilibrium path reaches a relative maximum before a secondary path is intersected one can say that the structure is at the limit point corresponding to a limit load, Fig. 1.1a. After the limit load is reached the structural deformation involves finite displacements. In this case, only a large displacement theory is able to describe the equilibrium on the postbuckling path. The possibility of bifurcation from a nonlinear primary path is not excluded (Fig. 1.1a).

Having defined the concepts of equilibrium path, bifurcation points and limit points one can define the critical load as the smallest load on the primary equilibrium path at which the equilibrium of the structure fails to be stable.

1.2.1 Behavior of Perfect Shells

Von Karman and Tsien (1941) described the behavior of an axially loaded perfect cylinder (Fig. 1.2). When the axial load P increases gradually from zero the equilibrium path follows a straight line. At load level P_c of Fig. 1.2, the elastic buckling load is reached and an adjacent

equilibrium configuration exists with infinitesimal lateral deflections but with the same end shortening. However, for smaller postbuckling loads there exists an elastic equilibrium configuration involving finite lateral deflections. In the deflected configuration the total potential energy of the shell can be smaller than that in the undeflected configuration. The equilibrium of the shell is highly unstable and small perturbations can cause the shell to change into a configuration of lower energy (Flügge 1973).

Brush and Almroth (1975) affirmed that the equilibium path for an axially compressed cylinder (Fig. 1.2) is similar for other methods of loading, namely, torsion, uniform lateral pressure, and hydrostatic pressure.

1.2.2 Behavior of Imperfect Shell

Imperfect shells are those with small deviations from the assumed initial shape. Brush and Almroth (1975) state the following characteristics of loaded cylindrical shells:

1. The limit load represents the ultimate strength of the structure.
2. The limit load of the imperfect shell may be substantially lower than the bifurcation point load of the perfect one.

These characteristics, shown in Fig. 1.2 are applicable to different loading models, namely, axial compression, torsion, uniform lateral pressure, and hydrostatic pressure.

In general, whether the limit load of the imperfect structure is close to the bifurcation load of the perfect structure depends on the shape of the secondary equilibrium path and the magnitude of the imperfections (Brush and Almroth 1975).

Bushnell (1985) also maintains that in the case of a real (imperfect) structure, there is no such thing as bifurcation buckling. The actual structure follows a load deflection path with a limit point (Fig. 1.2).

1.2.3 Pre- and Postbuckling States of Shells

Many shell - loading combinations are found to exhibit a small displacement linear (or nearly linear) prebuckling path. On this basis early theoretical studies treated the buckling of these shells as a linear eigenvalue problem. This analysis leads to the value P_c of the Fig. 1.1b. The value of P_c is refered to as the classical buckling load.

Hutchinson and Koiter(1970) in their review of buckling theory have shown that the classical buckling load is a reasonably good approximation of the load level at which an imperfect structure begins to undergo significant buckling deflection, only if the structure has a fully stable postbuckling regime, Fig. 1.3b. Later work focused on finding the minimum load in the buckled state on the secondary path, Fig. 1.2, because this load was held to be significant as a possible design load on the grounds that the structure could always support at least this load and

that even imperfections would not reduce the buckling load below this value. This concept is not universal because a minimum may not exist (Hutchinson and Koiter 1970, Esslinger and Geir 1975).

The buckling behavior of elasto - plastic structures under loading is the result of a complex interaction between geometric and material nonlinearities. Hutchinson and Koiter (1970) published a survey related to the buckling analysis in the elasto - plastic range.

1.2.4 Imperfection Sensitivity

Koiter (1945) explained the discrepancies between experiments and theoretical predictions of the buckling load by the introduction of the imperfections in the mathematical buckling formulations. Perfect shell - loading combinations having a linear elastic response and possessing a unique postbuckling path exhibit one of three types of initial postbuckling behavior (Fig. 1.3). In Fig. 1.3 δ represents a measure of the buckling mode amplitude, t is the shell thickness, and P_c, the classical buckling load. In the symmetrical cases (a) and (b) the postbuckling response is independent of the sign of the initial imperfections. Many shell loading combinations pertain to this category. The path AB can be represented in an asymptotic sense ($\frac{\delta}{t}$ approaches zero) by the series

$$\frac{P}{P_c} = 1 + a\,\frac{\delta}{t} + b\,(\frac{\delta}{t})^2 + \ldots\ldots, \qquad [1.1]$$

where "a" is a measure of asymmetric response, Fig. 1.3c. For symmetric buckling behavior, where the sign of the imperfections is of no importance, "a" is zero. The coefficient "b" is a measure of imperfection sensitivity. If "b" is positive, postbuckling behavior is stable, Fig. 1.3b. If "b" is negative, postbuckling behavior is imperfection sensitive, Fig. 1.3a. Koiter used the modal buckling shape, with an amplitude $\bar{\delta}$, to describe the imperfections. For this description of the imperfection and for the symmetrical case (a) of Fig. 1.3, Koiter derived the following asymptotic relation (Brush and Almroth, 1975)

$$(1 - \frac{P_s}{P_c})^{3/2} = \frac{3\sqrt{3}}{2} \sqrt{-b} \left|\frac{\bar{\delta}}{t}\right| \frac{P_s}{P_c} \qquad [1.2]$$

where P_s is the critical load, P_c is the classical buckling load, $\bar{\delta}$ is the amplitude of the imperfection, and, t is the thickness of the shell.

Koiter showed that a value "b" approximately equal to -1 simulates the experimental behavior of axially loaded cylinders successfully. Therefore, it can be said that a shell-loading combination having a value of "b" near -1.0 implies that it is as imperfection sensitive as the axially loaded cylinder. It is recognized that the axially loaded cylinder is a severe imperfection sensitive shell-loading combination.

1.3 Behavior of thin Cylinders under Transverse Shear

The only theoretical bifurcation solution for curved panels subjected to pure shear has been developed by Batdorf et al (1947). The critical shear stress is given by

$$\tau_{cr} = k_s \frac{\pi^2 D}{b^2 t} \qquad [1.3]$$

where b is the axial or circumferential dimension of the panel, t is the thickness and D is the classical flexural plate stiffness per unit length. The parameter k_s is a buckling coefficient which Batdorf derived as

$$k_s = f(Z) \qquad [1.4]$$

where Z is a function dependent on the radius, thickness and panel dimensions as well as Poisson's ratio of the cylinder material. Batdorf's solution compares well with the experimental work done by Chiarito (1945), Rafael (1943), Rafael and Sandlin (1945), and Kuhn and Levin (1945). These experiments were practically free of initial imperfections.

Lundquist (1932,1933,1935) conducted tests on thin aluminum cylindrical shells under pure torsion, pure bending, and combined transverse shear and bending. In his study on combined transverse shear and bending, it is assumed that ordinary beam theory applies. From purely physical considerations the shear and the moment relative to the size of the cylinder was considered in the analysis of

the results. Lundquist has shown that for large values of $\frac{M}{RV}$ ($3<\frac{M}{RV}<12$), failure occurs in a bending buckling mode similar to that of pure bending buckling mode, and the bending strength approaches that of a cylinder of the same dimensions in pure bending. For small values of $\frac{M}{RV}$ ($0<\frac{M}{RV}<2$) failure occurs in a shear buckling mode by the formation of diagonal buckles on the sides of the cylinder. The size and form of the buckles are the same with those buckles due to pure torsion for a cylinder of the same dimension. At the limit when $\frac{M}{RV}$ approaches zero the calculated shear stress by ordinary beam theory is approximately 1.25 times the allowable shear stress in torsion. This is due to the gradient effect present in transverse shear and absent in torsional shear. For intermediate values of M/RV, there is a transition from failure by bending to failure by shear buckling that is accompanied by a reduction in strength. Lundquist (1935) developed a design chart for the strength of the thin - walled cylinders in combined transverse shear and bending.

Schilling (1965) investigated a considerable number of tubes under combined loading conditions. He suggested that for elastic buckling, the critical shear stress in transverse shear be taken as 1.25 times the critical shear stress in pure torsion.

Yamaki et al (1979) conducted studies on the elastic buckling loads of thin cylinders made of polyester sheets loaded laterally as well as with internal pressures. The

load deflection curves showed shear bifurcation buckling, followed by a drop in load and increased displacements. The range of Batdorf's Z values for the test cylinders was between 20 and 20,000. He suggested that a good approximation to the maximum elastic critical shear stress under lateral load would be the elastic critical stress under torsion. The critical shear stress is given as

$$\tau_{cr} = 0.74\ E\ (\frac{R}{L})^{0.5}\ (\frac{t}{R})^{1.25} \qquad [1.5]$$

where E is Young's modulus, L is the panel length, and R and t are the radius and thickness respectivelly.

Galletly and Blachut (1985) carried out investigations of short thin cylindrical shells under lateral loading. They reported that the plastic buckling load is not imperfection sensitive. They suggested a critical plastic shear stress

$$\tau_p = \tau_Y\ (1 + (\frac{\tau_Y}{\tau_{cr}})^2\ )^{-1/2} \qquad [1.6]$$

where τ_Y is the shear yield stress and τ_{cr} is the critical shear stress of a perfect cylinder in pure torsion given by Eq. (1.5)

Bailey and Kulak (1984) tested two cylinders under lateral loading. They reported the possibility of a developed tension field similar to that developed by flat plates in shear and suggested an approach similar to that of Basler (1961) as well as the main frame for future

developement of design specifications of cylinders under lateral loading. The load deflection curves obtained show the behavior of the imperfect shell. As a limit point is reached the shell buckles, showing finite displacements.

Mok and Elwi (1986) carried out a numerical investigation of thin cylinders under lateral loading with a radius to thickness ratio equal to 250 and a length to radius ratio equal to 2. The investigation was carried out in the nonlinear range with various sizes of imperfections. The imperfections were modeled using the first mode buckling shape obtained for the perfect shell in shear.

The bifurcation buckling results are in good agreement with the theoretical values obtained from Batdorf's graphs for small sizes of the imperfections (1/100 of the thickness of the shell). The linear buckling analysis carried out parallel to the numerical analysis showed that it is a good approximation for the bifurcation point. For bigger values of the imperfections the bifurcation load is smaller. In this case the linear buckling analysis is not a good approximation of the limit loads. In all cases with different sizes of imperfections the structure showed practically the same stiffness for the vertical displacement of the top middle point of the cylinder.

1.4 Statement of the Problem and Objectives

The numerical investigation of Elwi and Mok (1986) is clearly limited to modelling the imperfections using buckling modes of perfect shells. In addition the effects of residual stresses are entirely neglected. There are two types of residual sresses involved in these cylinders. The first is the residual stress due to cold rolling while the second is due to welding. Rolling stresses may or may not result in yielding of the shell plate. The yielded stress pattern may or may not be released before welding is applied. If the former, a pattern of residual stresses is developed. If the latter, the stress pattern is locked in. There are, also, two types of welds, longitudinal seam welds and cicumferential welds. Weld shrinkage and local heating cause different patterns of residual stresses in the neighbourhood of the weld seam.

The objectives of this study, then, are summarized as,

1. To study the influence of measured imperfections on the transverse critical shear.
2. To investigate the influence of different residual stress distributions combined with different degrees of measured imperfection on the transverse critical shear.
3. To investigate the behavior of laterally loaded thin cylinders beyond the critical load and to investigate the existence and the developement of the tension fields after buckling occcurs.

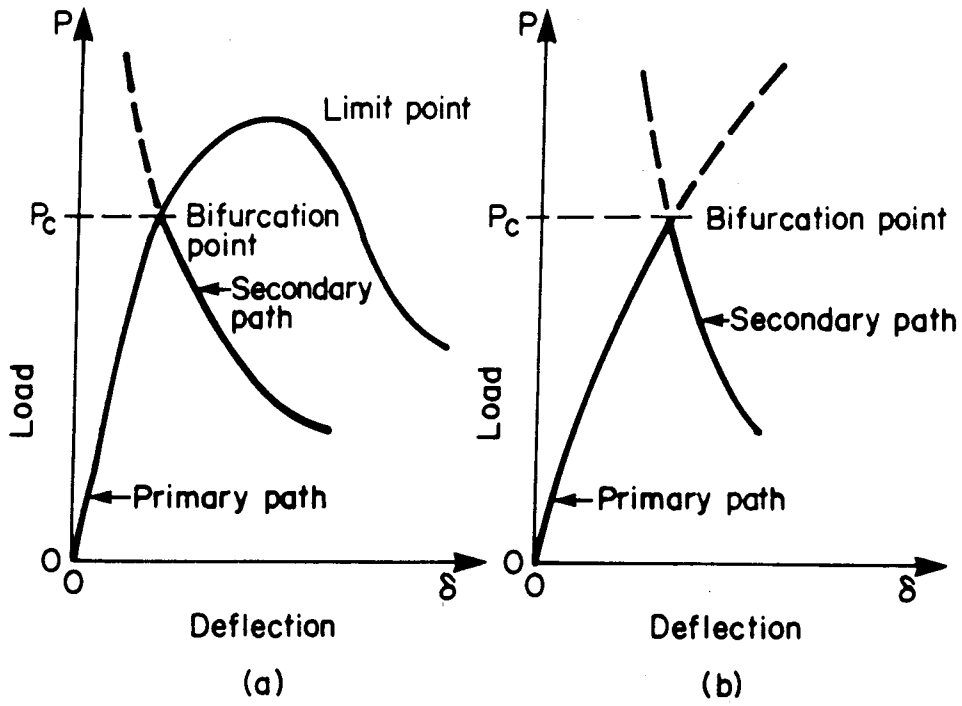

Figure 1.1 Generalized Load Displacement Behavior

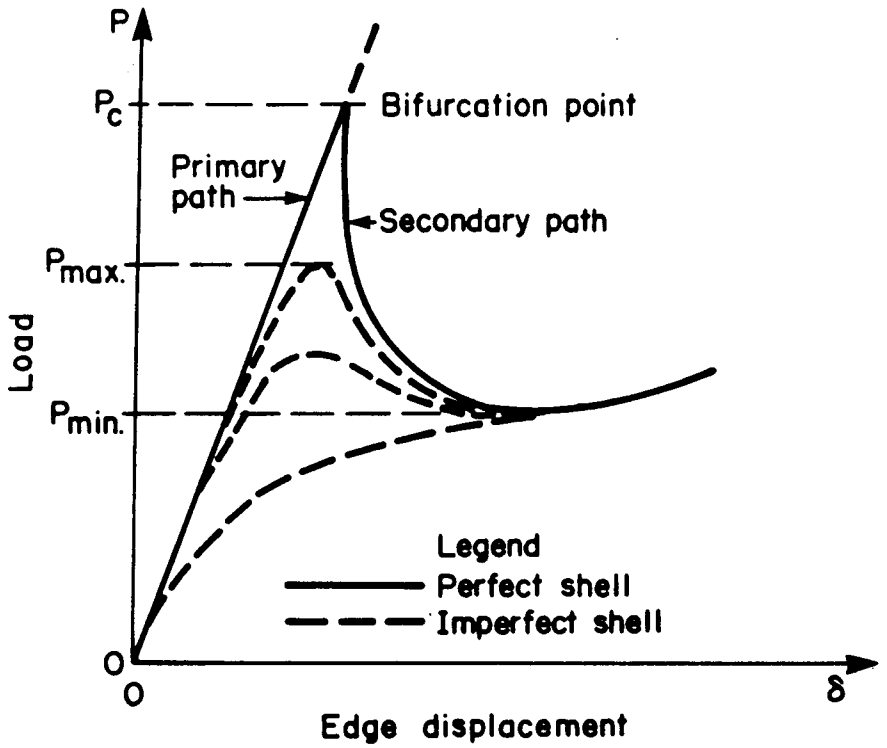

Figure 1.2 Load Displacement Curves for Axially Loaded Cylinder.

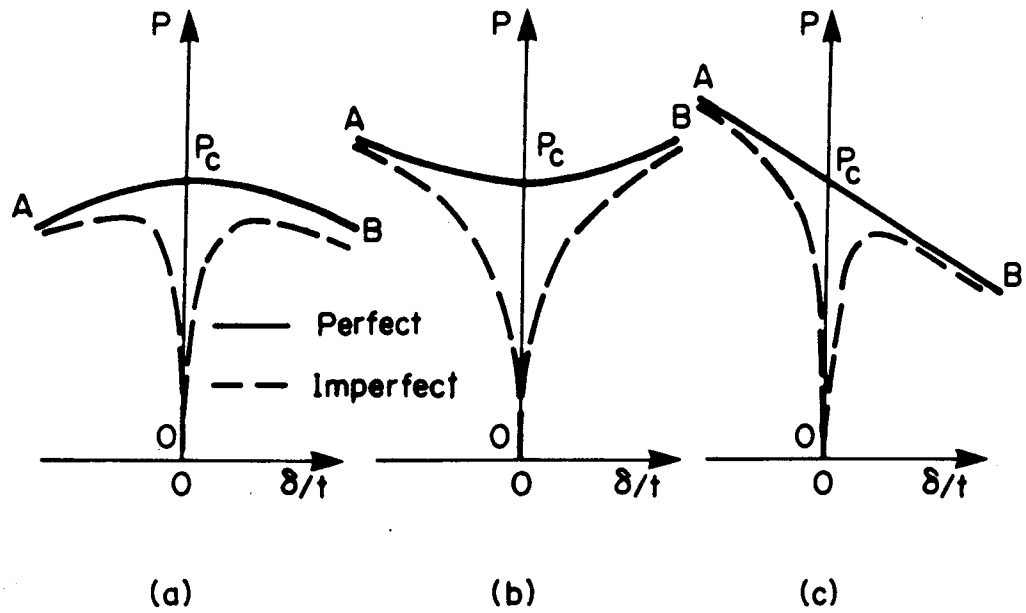

Figure 1.3 Postbuckling Response of Shells

2. Effect of Modelling Imperfections on Buckling and Limit Loads

2.1 Introduction

There are different approaches in the implementation of the initial imperfection in buckling analysis or nonlinear analysis. Koiter (1945) used the first buckling mode shape to model the imperfection in the mathematical model of cylindrical shell buckling. The minimum eigenvalue obtained is supposed to be an "upper bound" for the critical load parameter.

Arbocz and Babcock (1976) used Fourier series containing both axisymmetric and nonsymmetric components to describe the measured imperfection. Their conclusion is that using multimode analysis makes it possible to predict, with a good approximation, the buckling load of axially compressed cylinders.

Esslinger and Geir (1975) conducted experiments on cylinders loaded under external pressure. They identified different postbuckling patterns of stable equilibrium by inducing patterns with a smaller number of circumferential waves. Concomitantly with finding different stable patterns they found a minimum load in the postbuckling region, smaller than that obtained spontaneously in experiments. The theoretical development of these experiments has shown that the buckling load obtained for a smaller number of circumferential waves is bigger than that obtained for a

higher number of circumferential waves. Their conclusion is that cylinders with small imperfections buckle following the postbuckling characteristics of a perfect cylinder, obtained spontaneously, and cylinders with large imperfections buckle following the postbuckling pattern of a perfect cylinder with a smaller number of circumferential waves. In the case of deep imperfections, it is possible not to get buckling at all and the total load carrying capacity is determined by the material yielding. Also in the postbuckling region the deformations are so large that the initial imperfection is negligible by comparison and the equilibrium path follows the postbuckling path of the perfect cylinder.

Fersht (1974) used a random description of the small initial imperfection in the buckling analysis of the axially loaded cylinders.

Morton, et. al. (1979) performed experiments on spheres under external pressure with different induced imperfection shapes. Parallel to the experiment, a numerical analysis was carried out. Three different types of imperfection described as a local flat, increased radius, and a bulge were used. The range of the ratio of the maximum imperfection to shell thickness is large (up to 55). It was concluded that Koiter's imperfection sensitivity equation (Eq 1.2) is good enough to predict the buckling load well outside the imperfection range of the shell thickness but only for flat and increased radius types of imperfection. For the bulge type of imperfection the values of the experimental buckling

load cannot be explained by Koiter's treatment. The same observation was made by Sabir (1964). The buckling loads are lower than those predicted by Koiter's equation, particularly for imperfection to thickness ratios under 10. Although different meshes were tried it was not possible to reproduce the experimental buckling loads for the bulge imperfection shape.

One can infer that there may be other imperfection shapes, different from the buckling shapes, able to give lower buckling loads for the same imperfection to thickness ratio.

In this study two types of analyses have been attempted. The first is based on flute type imperfections such as those that may result from a rolling process. The second is based on the actual imperfections measured by Bailey and Kulak (1984).

2.2 Description of the Models

The geometry of the Bailey and Kulak (1984) first shear test specimen forms the base of the analysis presented herein and in subsequent chapters. The same overall geometry formed the basis of series S (Mok and Elwi, 1986). The models presented here are referred to as series SR. The basic model simulates half of the test specimen and consists of a cylinder formed by three cans. The shell is 808.5 mm long and has a midsurface radius of 190 mm. Each model is made up of two end portions and a test span. The test span

is 0.76 mm thick and, consequently the radius to thickness ratio is 250. The end portions are two times thicker than the test span, see Fig. 2.1. The cylinder is fixed at the left end. At the right end translations in the Z and X directions are separately coupled to simulate a gliding - fixed plane of symmetry condition. All other degrees of freedom are free. At the loading edge the displacements in the Z direction are coupled to avoid the distortion of the cylinder due to the concentrated loads. The vertical external load is equally distributed to the mesh nodes at the loading edge(Fig. 2.1).

The material considered is rolled sheet steel with an elasticity modulus E = 204,400 MPa, a Poisson's ratio ν = 0.33, static yielding stress σ_{ys} = 301 MPa and a thermal expansion coefficient α = 11.7 X 10^{-7} / ^{0}C.

The test series differ by the size and shape of the imperfection. The imperfection used in this study is that measured by Bailey and Kulak(1984) on the first shear specimen. The test cylinder was rotated about the longitudinal axis and, using a gauge installed on a fixed straight channel, readings were taken along the arcs. The arc distance was 37 mm, corresponding to an arc of 11.25 degrees and gave 32 radial measurements. These readings were taken at 25 mm intervals along the length of the test spans, except in the vicinity of the circumferential welds where the readings were taken at a smaller distance. The measurements were taken at 41 longitudinal arc locations

giving a total of 1312 measurements of initial imperfection.

The finite element mesh used is a 6 X 6 nonuniform mesh as shown in Fig. 2.1. The elements are 16 node Lagrangian 3D degenerated shell elements (Ramm 1977). The numbering of the elements and the nodes is given in a developed view of the mesh, Fig. 2.2. The analysis shown in this chapter and in subsequent chapters was carried out using the Program N I S A (Ramm, 1977, Häfner et al, 1981, Stegmüller, 1984). A brief description of the program and the solution strategy adopted in this study are included in Appendix A.

2.3 Analysis with Flute Imperfections

First attempt to model the imperfections was to consider the arc with the maximum radial deviation and assign the same shape to all arcs. Thus the imperfection takes the form of longitudinal flutes, superimposed on the cylinder. The imperfection is scaled as a function of the shell thickness.

First series of analyses are designated SR1, SR2 and SR3, with the maximum size of the imperfection equal to 1/100 t, 1/10 t and t, where t is the shell thickness.

All three models have practically the same load deflection curve and the same critical load in spite of the different size of the imperfections (see Fig. 2.3). The prebuckling path is linear up to 33.0 kN. The analysis of the SR1 model was continued after reaching the critical load and first plastifications occured in the elements located on

the tension diagonal of the test span. A stable equilibrium path in postbuckling at a lower load level was attained. In far postbuckling range of the SR1 model an elastic unloading to 17.45kN followed by a reloading on the same path was obtained. The stiffness of the cylinder on this unloading and reloading path is 5.78kN/mm. This value of the stiffness is close to the stiffness value, 5.03kN/mm, obtained on the ascending equilibrium path by Bailey and Kulak (1984) on their first shear experiment. The buckling load calculated at a low load level is a good approximation of the critical load. Practically all the models behaved like perfect shells showing no imperfection sensitivity for the range of the flute imperfection less than or equal to the shell thickness.

At a load level of 33.95 kN the cylinder buckles in a shear mode shape. The buckling modal shape and the deformed mesh are plotted in Fig. 2.4 a,b respectively. One can see the configurations are similar showing a shear buckling mode shape. The load level of 33.95 kN is the critical load because the lateral displacements at the points located in the buckled region have relatively large displacements for small increases in the load level (Fig. 2.5) and the equilibrium path at the loading edge shows an abrupt descent (Fig. 2.3), indicating the incapacity of the structure to sustain the load.

2.4 Analysis with Measured Imperfection

The data related to the imperfection are the data obtained by Bailey and Kulak (1984) from the first shear specimen. The following procedure was used to get the average of the measurements along each arc. The average was considered to be the perfect cylinder. The radial deviations from the average were determined at each node of the mesh. The mesh used to measure the imperfection was close to the mesh used in the finite element analysis and the mapping did not need interpolation. The average over the arcs only was used to avoid the false imperfection which might be induced by the nonparallelism of the test cylinder centerline and the measuring datum. The resulting imperfect mesh is plotted together with the perfect mesh at a magnified scale in Fig. 2.6. The imperfection was scaled to give different ratios of the maximum size of the radial deviation to the shell thickness. Two analyses were carried out; the first with small imperfections of the order of the shell thickness, and the second has large imperfections of the full magnitude of measured imperfections.

2.5 Small Measured Imperfection Analysis

The model used in this analysis is refered to hereinafter as SR4 and the size of the scaled imperfection is one times the thickness of the thinner part of the cylinder. The load response is practically linear up to 32.0 kN as one can see in Fig. 2.7., reaching the critical

load at 33.18 kN and following a sharp descending path thereafter. At the maximum load the cylinder fails in a shear buckling mode. The presence of buckling can be seen also in Fig. 2.8 which shows the lateral (Y) displacement versus load of the points located in the buckled area. The displacements at the maximum load show a jump and are considerably larger than the previous displacements. The loading was continued beyond 33.18 kN when first plastifications appeared on the elements located on the test span diagonal and the lateral displacements in this region showed that buckling took place. Maximum load attained at 33.18 kN is smaller than that of the model SR1 due to the shape of the imperfection used in the model SR4. The deflected shape at maximum load is similar to the modal shape obtained by buckling analysis at the load levels 3.02 kN and 15.10 kN, as one can see in Fig. 2.9.

No bending compression buckles were noticed at the top of the cylinder in the compression areas.

2.6 Large Measured Imperfection Analysis

Model SR5, used in this analysis, contains the full size measured imperfection. The maximum deviation from the perfect cylinder is 6.5 times the cylinder thickness.

The load response is practically linear up to 25.0 kN. Maximum attained load level is 29.61 kN (see Fig. 2.10). At 29.61 kN buckling takes place and is associated with the first plastifications on the elements located on the main

diagonal of the thinner cylinder.

The numerical analysis was carried out further in the postbuckling range. A significant stress redistribution takes place concomitant with a reduction in the external load and an increase in vertical and lateral displacements. After buckle formation on the lateral side of the test span the tensioned membrane diminishes in area, because the valleys of the buckles move inwards and shorten, thereby unloading the tensile stresses.

In Figs. 2.11 to 2.14 one can see from the shape of the equilibrium paths and from the size of the deflections at some nodal points on the side of the test span that buckling takes place. The most representative is the equilibrium path of node 217 which is similar in shape to the dotted line of Fig. 1.1a.

Another area of interest is the compressed top part of the shell as a result of bending. By plotting the equilibrium path of the points located in that area one can find out if bending buckling is present from the relative displacements of the points. In Fig. 2.15 one can see that bending buckling starts developing well in the postbuckling branch. There is a clear trend of moving up and down for the points in the compressed area.

The deflected shapes and the buckling modes on the prebuckling equilibrium path are plotted in Fig. 2.16. The similarity of shapes between the buckling mode and the deformed shape at the critical load can be easily seen.

In the postbuckling branch the lateral deflection increases much faster than the vertical deflection at the top middle point of the cylinder. The deformed meshes look almost identical to those obtained for the buckling mode shape in the analysis carried out on the prebuckling branch (Fig. 2.17).

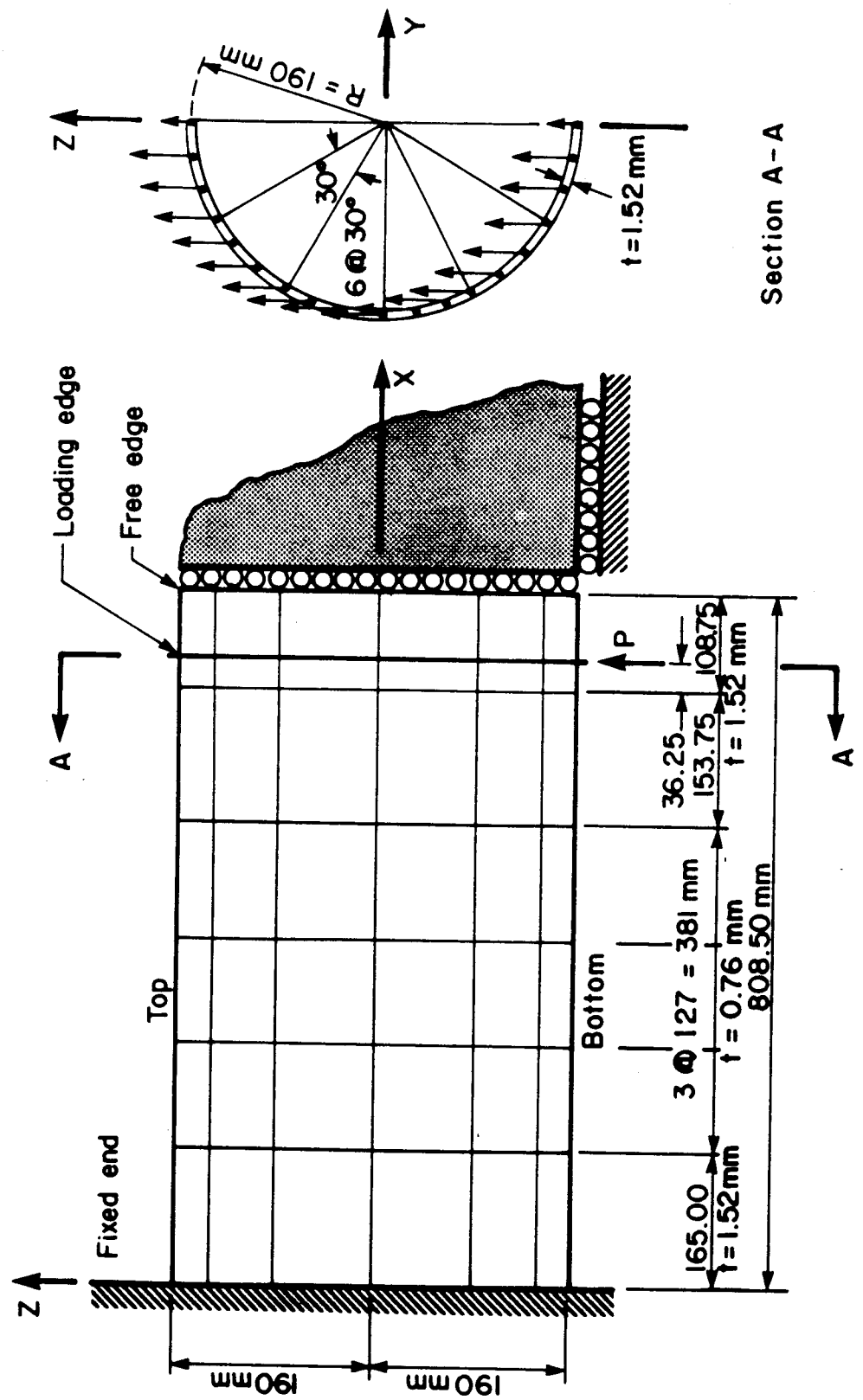

Figure 2.1 Boundary Conditions, Loads and Mesh for the SR Models

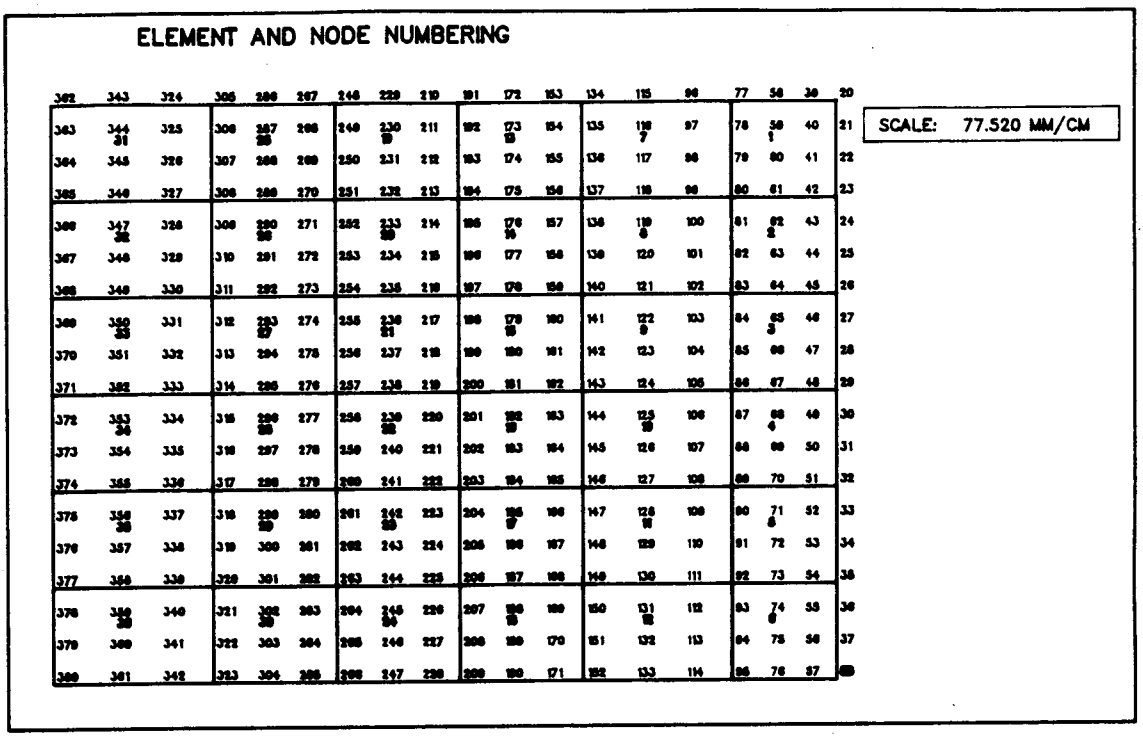

Figure 2.2 Element and Node Numbering for the SR Models

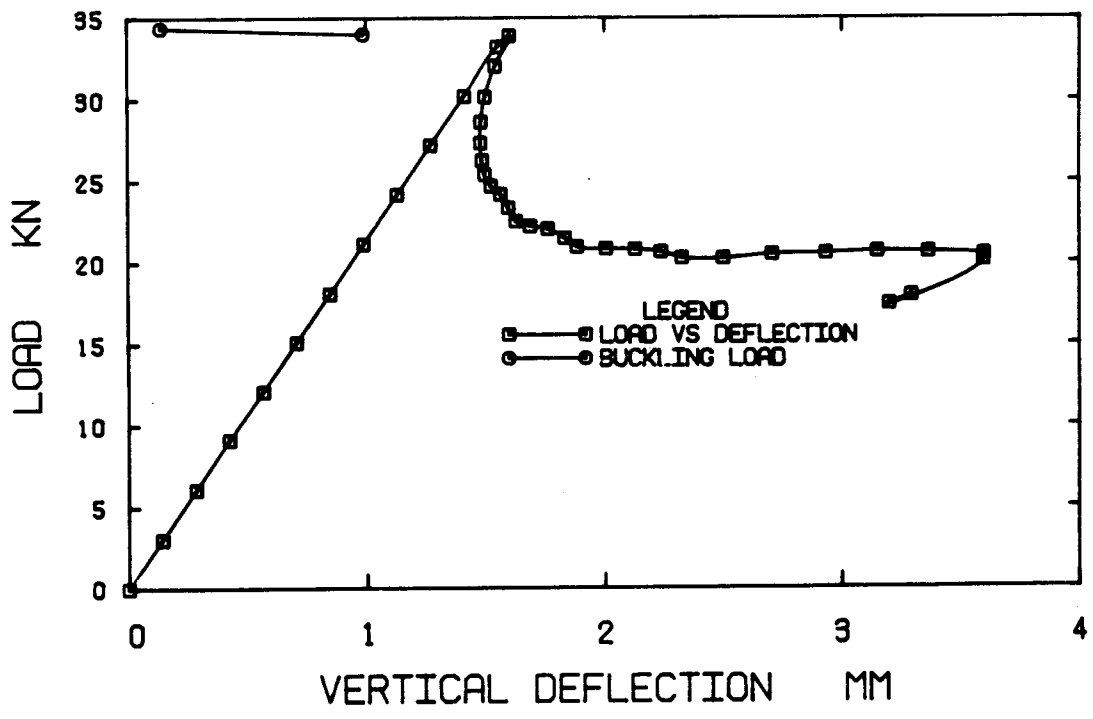

Figure 2.3 Model SR1 - Load vs Deflection

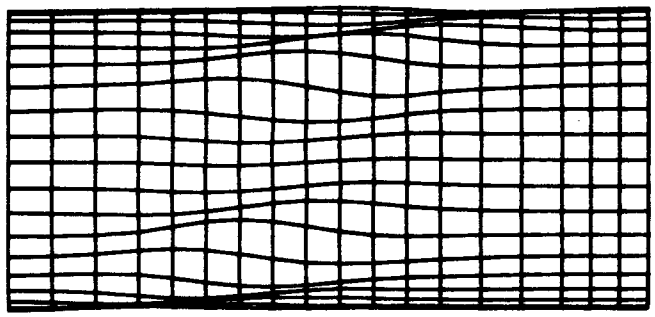

Buck. Shape at 3.02kN
in Prebuckling Range
Buckling Load=34.0kN
Magn. Factor=8000

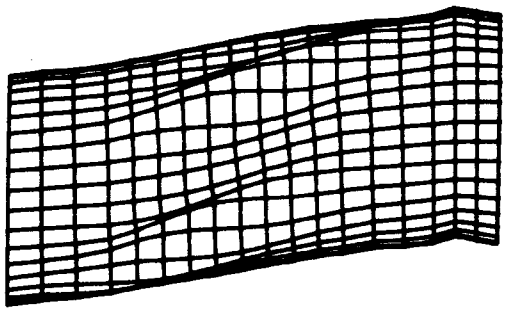

Def. Shape at 33.91kN
in Prebuckling Range
Magn. Factor=50

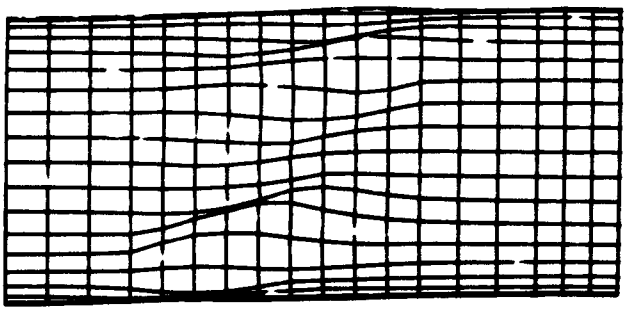

Buck. Shape at 21.16kN
in Prebuckling Range
Buckling Load=34.0kN
Magn. Factor=8000

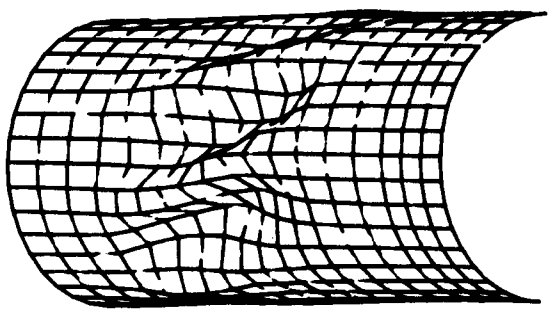

Def. Shape at 20.15kN
in Postbuckling Range
Magn. Factor=5

Figure 2.4 Deformed Shapes and Buckling Modes of model SR1 on the Pre- and Postbuckling Paths

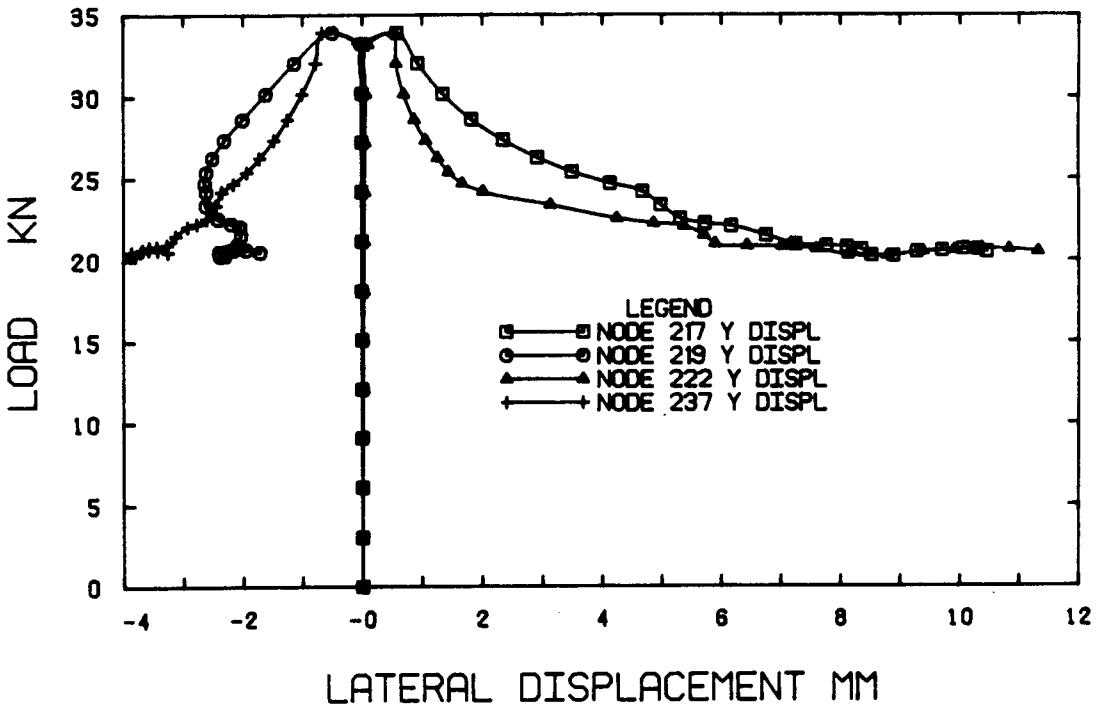

Figure 2.5 Load vs Lateral Displacement

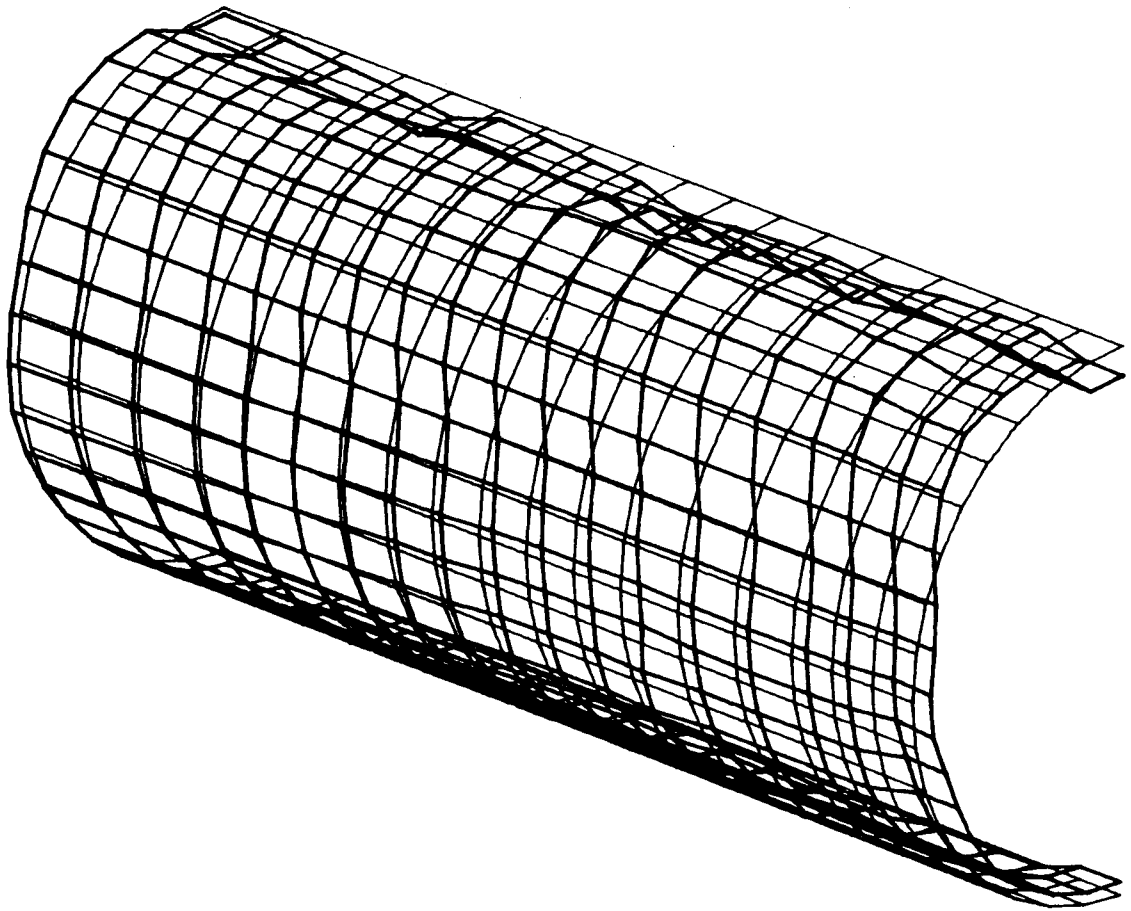

Figure 2.6 Perfect and Measured Imperfect Meshes

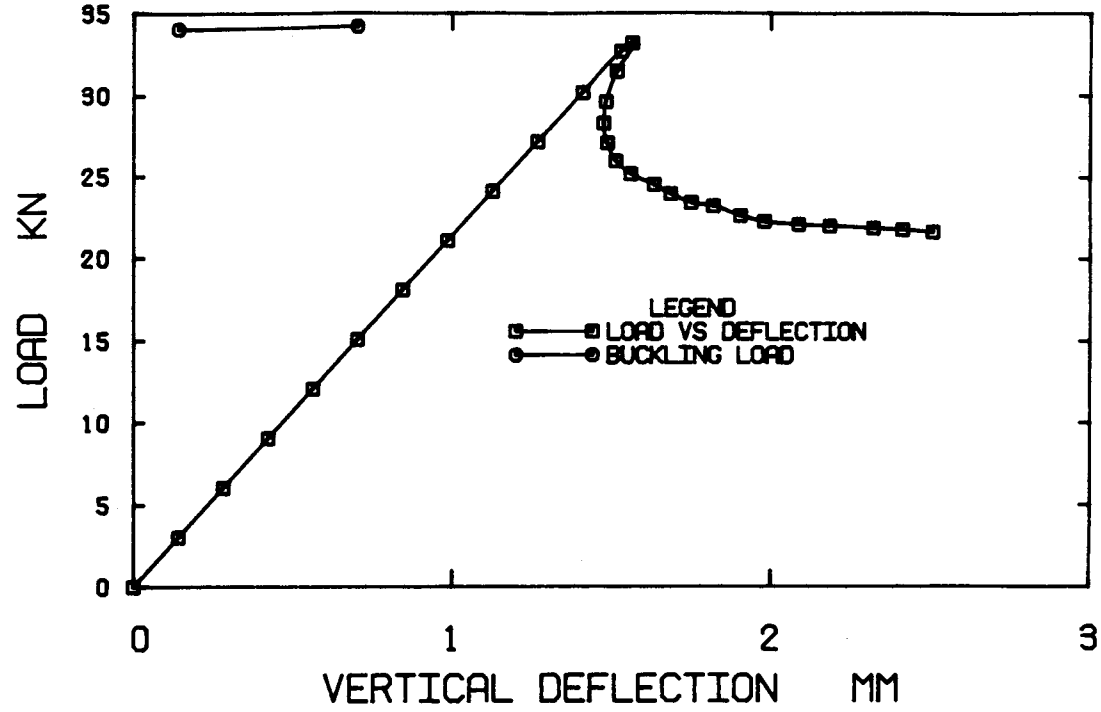

Figure 2.7 Model SR4 - Load vs Deflection

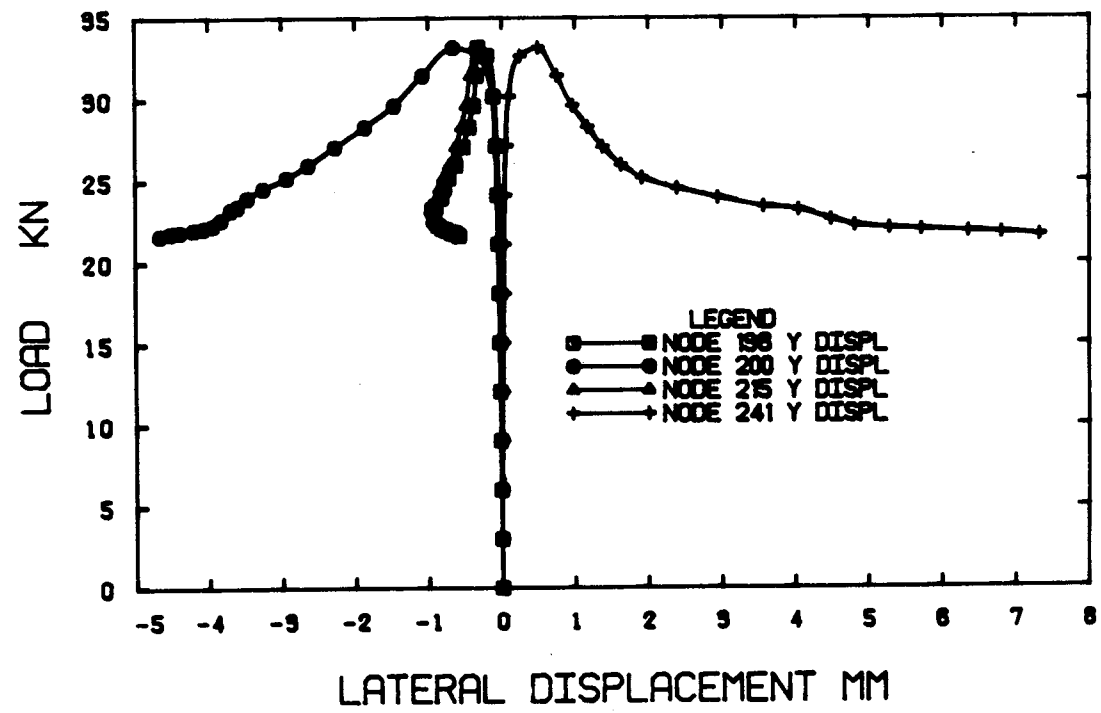

Figure 2.8 Load vs Lateral Displacements

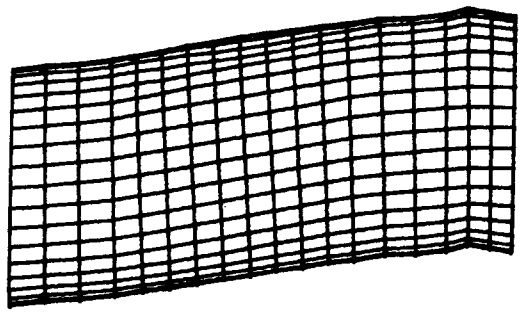

Def. Shape at 18.12kN

Magn. Factor=100

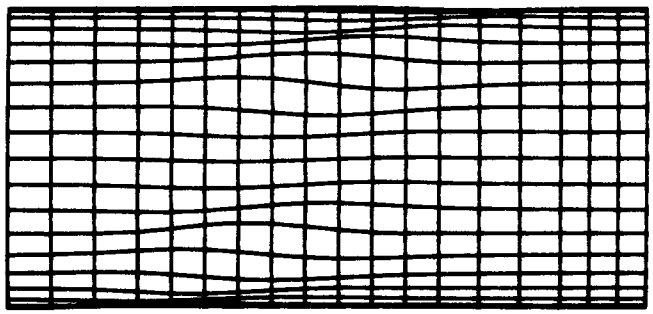

Buck. Shape at 15.1kN

Buckling Load=34.0kN

Magn. Factor=2250

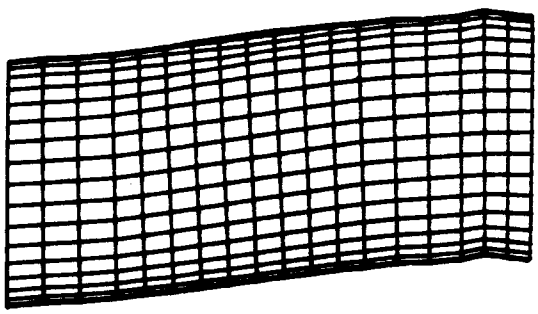

Def. Shape at 15.1kN

Magn. Factor=100

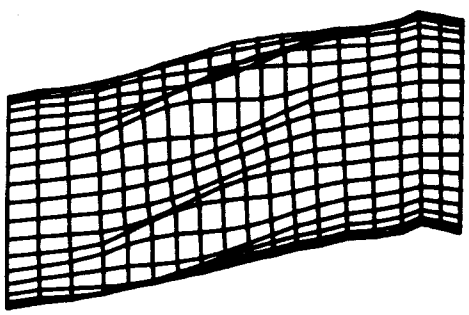

Def. Shape at 33.18kN

Magn Factor=100

Figure 2.9 Deformed Shapes and Buckling Modes of Model SR4 on the Prebuckling Path

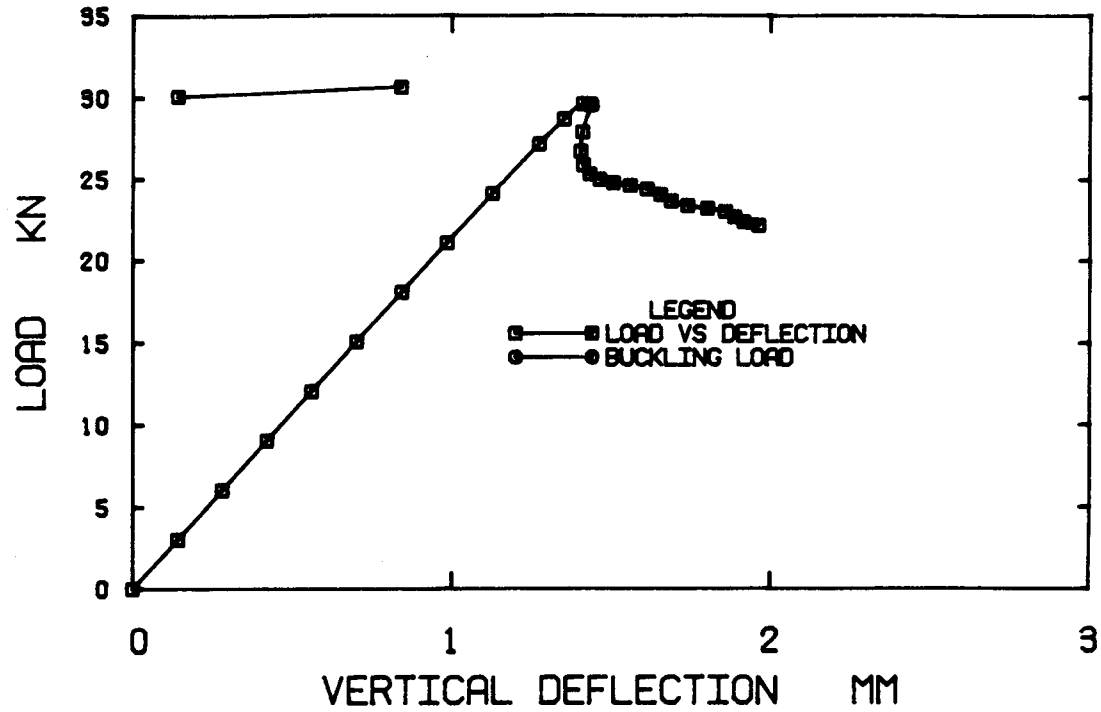

Figure 2.10 Model SR5 - Load vs Deflection

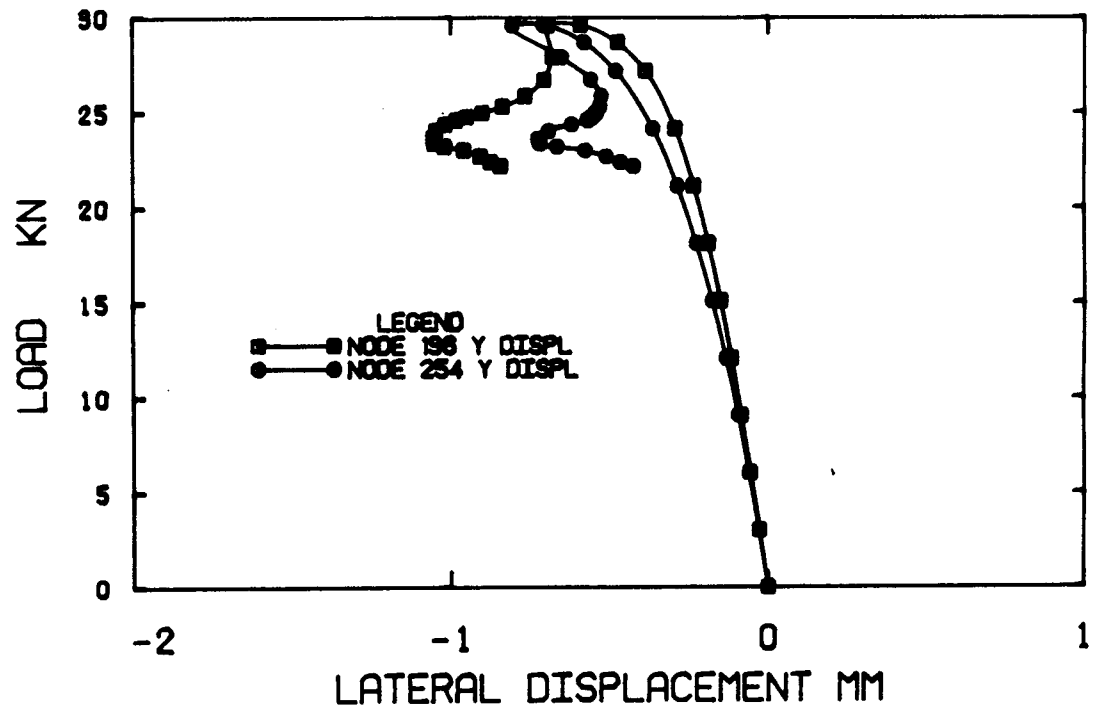

Figure 2.11 Load vs Lateral Displacements

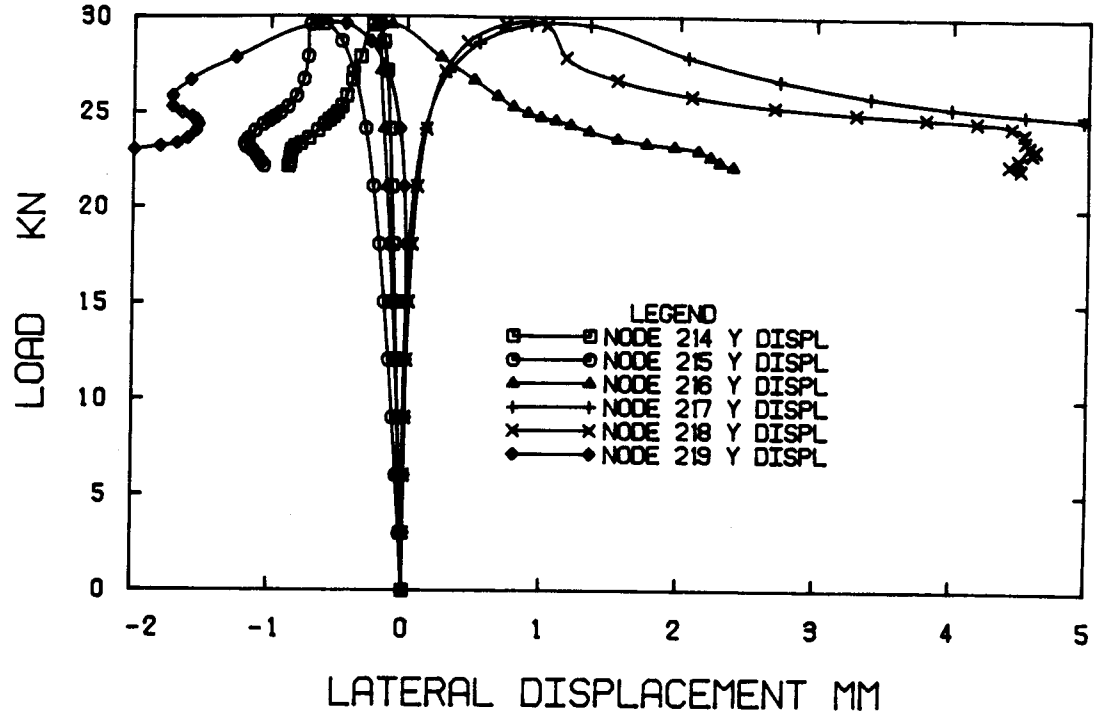

Figure 2.12 Load vs Lateral Displacements

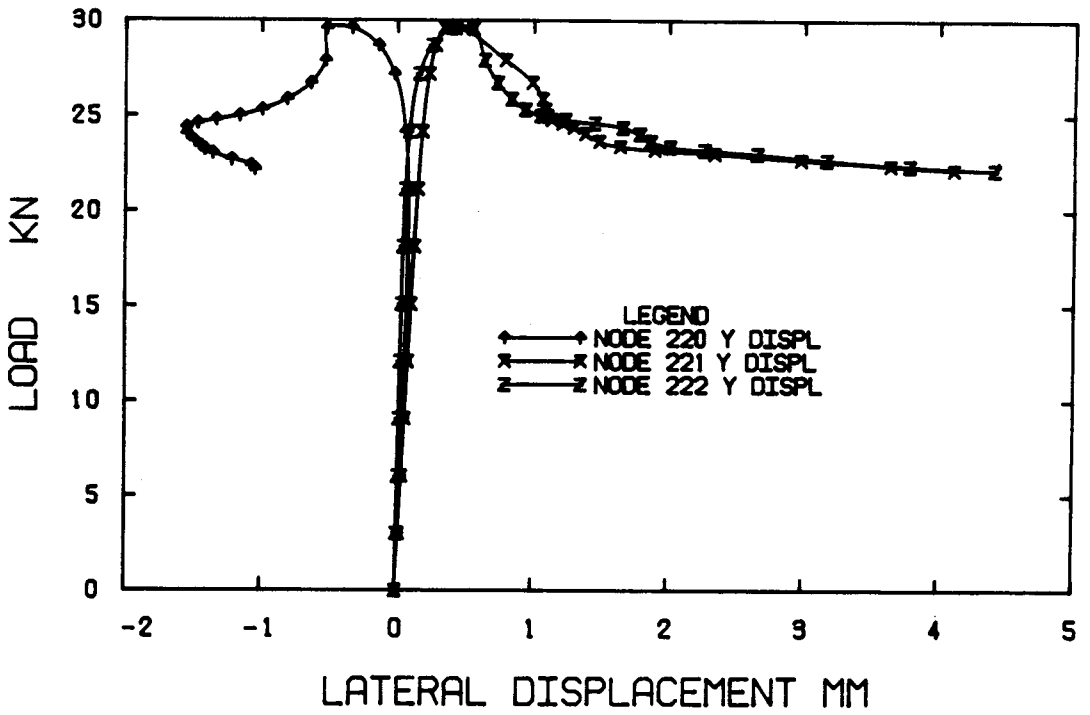

Figure 2.13 Load vs Lateral Displacements

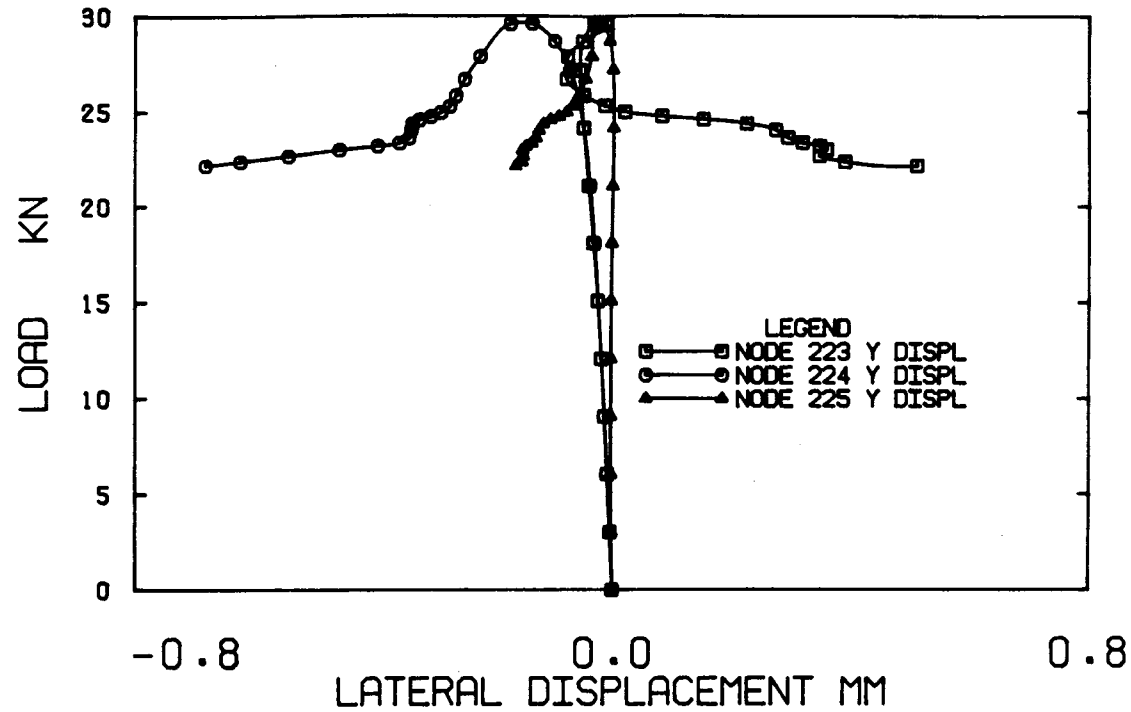

Figure 2.14 Load vs Lateral Displacements

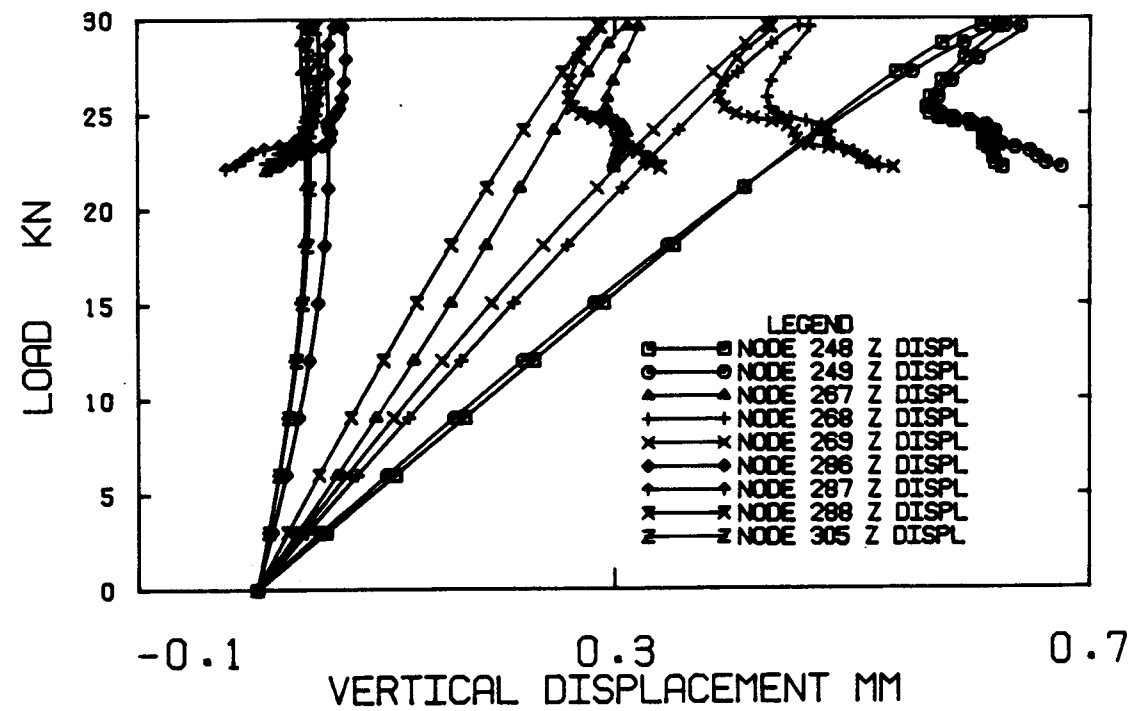

Figure 2.15 Load vs Lateral Displacements

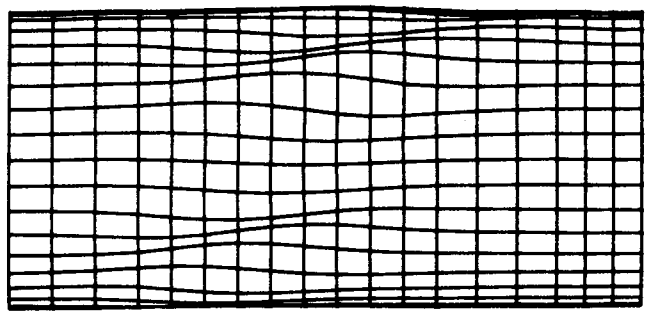

Buckl. Shape at 3.00kN

Buckling Load=30.1kN

Magn Factor=10000

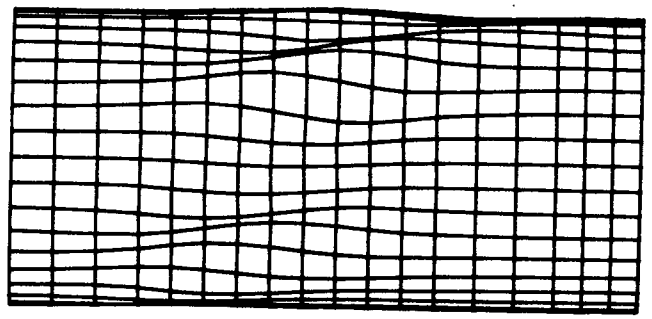

Buckl. Shape at 18.07kN

Buckling Load=30.67kN

Magn Factor=10000

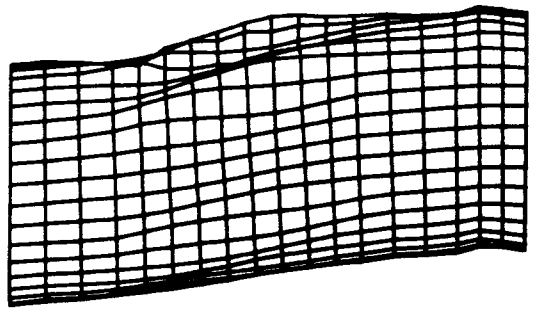

Def. Shape at 26.82kN

Magn Factor=75

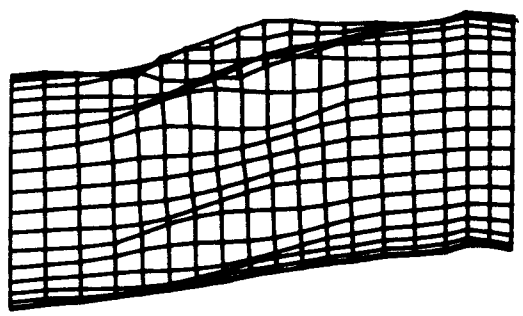

Def. Shape at 29.61kN

Magn Factor=75

Figure 2.16 Deformed Shapes and Buckling Modes of Model SR5 on the Prebuckling Path

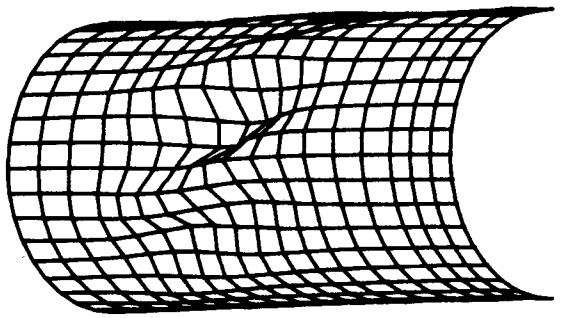

Def. Shape at 24.39kN

Magn Factor=10

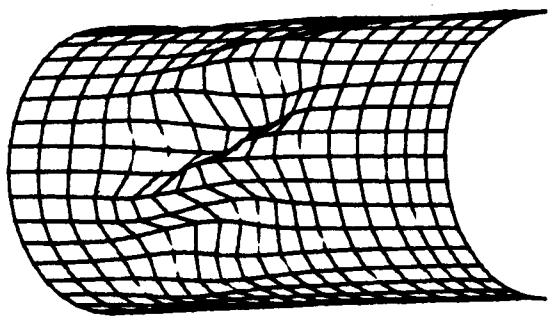

Def. Shape at 22.70kN

Magn Factor=10

Figure 2.17 Postbuckling Deformed Shapes of Model SR5

3. Effect of Cold Forming

3.1 Introduction

Cold forming is possible only with plastic or elasto-plastic materials. Lay (1982) gives indications and examples related to the evaluation of residual stresses resulting from cold rolling used in pipe manufacturing. Chen and Han (1985) present distributions of residual stresses caused by longitudinal welds and cold bending used to fabricate tubular columns. Their results were used in an investigation of the behavior of fabricated tubes under axial forces and bending moments.

Queener and De Angelis (1968) and Bushnell (1985) show analytical techniques to calculate the radius of bending of a flat sheet metal to get a final cylinder of a particular radius. Concomitantly, the evaluation of the residual stress distribution over the thickness and how these results are used in computer programs to evaluate the buckling loads are also given.

It was determined that bending residual stresses have the greatest weakening effect for cylindrical shells in which the effective stress is close to the proportional limit. The reduction in the buckling load could be over 30% (Bushnell 1985).

Cold forming creates a permanent strain field distributed over the structure. In this chapter the cold forming process, used to manufacture the cylinder under

consideration, is simulated by using suitable temperature gradients across the cylinder thickness. Model SR5TS used in this analysis has the geometry, mesh, boundary conditions and external load described in Section 2.2 for the SR series. It also has the full imperfection of model SR5.

3.2 Cold Forming Stresses

For a tube with a thickness t and radius R , an element on the surface of the tube has the local directions s and r shown in Fig. 3.1.

Bending of a flat plate to form a cylinder introduces a strain gradient in the s direction such that

$$\epsilon_s = \frac{z}{R}, \qquad [3.1]$$

$$\epsilon_{smax} = \frac{t}{2R}, \qquad [3.2]$$

$$\epsilon_r = - \nu \epsilon_s \qquad [3.3]$$

Eq. 3.3 implies that as the plate is bent to form a circle, a curvature is developed in the r direction if the plate is narrow (Fig. 3.2).

But if the plate is wide enough, a state of plain strain is enforced in the r direction. Therefore, barring some end effects, suppression of the longitudinal strain, ϵ_r, results in longitudinally constant self-equilibrating moments.

The values of the stress are derived from a yield condition. Assuming a von Mises yield condition,

$$\sigma_s^2 + \sigma_r^2 - \sigma_s \sigma_r = \sigma_y^2 \qquad [3.4]$$

and that at yield

$$\sigma_s = \epsilon_{sy} \frac{E}{1 - \nu^2} \qquad [3.5]$$

$$\sigma_r = \nu \epsilon_{sy} \frac{E}{1 - \nu^2} \qquad [3.6]$$

in which ϵ_{sy} is the yield strain in the s direction. Substituting for σ_s and for σ_r from Eqs. 3.5 and 3.6, Eq. 3.4 is written as

$$\frac{1}{(1 - \nu^2)^2} (\epsilon_{sy}^2 E^2 + \nu^2 \epsilon_{sy}^2 E^2 - \nu \epsilon_{sy}^2 E^2) = \sigma_y^2 \qquad [3.7]$$

or,

$$\epsilon_{sy} = \frac{\sigma_y}{E} (1 - \nu^2) (1 - \nu + \nu^2)^{-1/2}, \qquad [3.8]$$

and,

$$\sigma_{sy} = \sigma_y (1 - \nu + \nu^2)^{-1/2}, \qquad [3.9]$$

$$\sigma_{ry} = \nu \sigma_y (1 - \nu + \nu^2)^{-1/2}, \qquad [3.10]$$

where σ_{sy}, σ_{ry} are the stresses in the circumferential and longitudinal directions respectively at yield, σ_y is the uniaxial yielding stress, ϵ_{sy} is the value of circumferential strain at yield, ν is Poisson's ratio, and E is Young's modulus. It is important to note that σ_s and σ_r (Eqs. 3.5, 3.6) have the same sign.

For the material used in the SR models (having E = 204,400 MPa, σ_y = 301 MPa and ν = 0.33), the yield strain, ϵ_{sy}, equals 0.001486.

The stresses which would be achieved if a springback is not allowed and, consequently there is a locked - in state of stress in the tube, are

σ_{sy} = 341.1 MPa

σ_{ry} = 112.5 MPa

For a plate with t = 0.76 mm, and R = 190 mm, the maximum circumferential strain ϵ_s, equals 0.002. The stress and strain distributions are those shown in Fig. 3.3, second row. The values of M_r and M_s calculated using these distributions are 13.3 N.mm/mm and 40.2 N.mm/mm, respectively, where M_s is the edge moment used to induce the curvature, Fig. 3.1, and M_r are longitudinal internal moments resulting from suppressing ϵ_r gradient. For a plate with t = 1.52 mm, and R = 190 mm, the maximum circumferential strain is 0.004, and the stress and strain distributions are those shown in Fig. 3.3, first row. The

calculated values for M_r and M_s are 62.0 N.mm/mm and 188.0 N.mm/mm. These values are summarized in Table 3.1.

In the manufacturing process of cold formed tubes the plates are cold bent using rollers at a smaller radius than the desired radius, and, then, are allowed to springback. This procedure is repeated until the desired cylinder radius is obtained after springback. It is assumed that this procedure has been used in the manufacturing process of the Bailey and Kulak(1984) first shear specimen and the following development is restricted to this specimen which has the same geometry as the SR series.

Queener and De Angelis (1968) show how to calculate the bending radius of sheet metal to get a desired cylinder radius after springback. According to their formula,

$$\frac{R_0}{R_f} = 1 - \frac{3K(1-\nu^2)}{E(2+n)(3/4)^{(1+n)/2}} \left(\frac{2R_0}{t}\right)^{1-n} + \left\{\left(\frac{2R_0}{t}\right)\left(\frac{K}{E}\right)^{1/(1-n)}\right\}^3 x$$

$$\left\{\frac{3(1-\nu^2)^{3+n}}{(2+n)(3/4)^{(1+n)/2}(1-\nu+\nu^2)^{(2+n)/2}} - \frac{(1-\nu^2)^3}{(1-\nu+\nu^2)^{3/2}}\right\} \qquad [3.11]$$

where R_0 is the die radius plus half-thickness of sheet, R_f is the radius of curvature of sheet mid-section after springback, t is the thickness of sheet, E is the elasticity modulus, ν is Poisson's ratio (elastic case), and K, n are empirical constants in the power law relationship between the true stress and the true strain in a simple tension test (stress=K(strain)^n), for a 1.52 mm thick plate and for a 0.76 mm thick plate, (made of steel with the material

characteristics previously described, and K=341.1 MPa, and n=0.08) the necessary bending radii are 135 mm and 84 mm, respectively.

The elastic springback moment for the thick plate is 8 times bigger than that of the thin plate and, therefore, one can consider that the thin part plate follows the displacements of the thick part plate. In this situation the welded plate, composed of both the thick and thin parts, is bent to a radius equal to 134 mm and allowed to freely springback to the desired radius equal to 190 mm.

For the thick part the strain and stress distribution (in the condition of plain strain problem) are those shown in Fig. 3.4a,b,c, first row. The maximum moment needed to bend the thick plate at a radius equal to 134 mm is equal to 192.47 N.mm/mm based on the stress distribution of Fig. 3.4b, first row. The springback is equivalent to the action of an equal and opposite bending moment and the residual stress distribution (Fig. 3.4e, first row) is that obtained by superposition of the stresses of Figs. 3.4b and d, first row.

The stresses due to the springback moment are calculated using the elementary elastic plate theory. According to the elementary plate theory (plain strain problem, Timoshenko and Woinowsky (1959)) the bending moment is

$$M = \frac{2}{3} \frac{E}{(1 - \nu^2)R} \left(\frac{t}{2}\right)^3 \qquad [3.12]$$

where E is Young's modulus, ν is Poisson's ratio, R is the bending radius and t is the plate thickness. Consequently the maximum elastic stress due to this moment is

$$\sigma_{max} = \frac{3}{2} \frac{M}{(t/2)^2} \qquad [3.13]$$

where M is the elastic bending moment and t is the plate thickness. Using this equation one may obtain the distribution shown in Fig. 3.4d, first row. Adding the stress diagram due to rolling and that due to springback, the residual stress distributions of Fig 3.4e, first row are obtained.

The thin part is bent at the same radius, 134 mm, which is larger than the radius of 84 mm needed to get free springback at the 190 mm radius. For this case the stress and strain distributions before springback are those shown in Fig. 3.4a,b,c, second row. The back movement from a radius equal to 134 mm to a radius equal to 190 mm gives a strain variation $\Delta\epsilon$ shown in Fig. 3.4d, second row. By superposition of the stresses of Figs.3.4b and 3.4e, second row, the locked-in stress distribution of Fig. 3.4f, second row, is obtained. Since the bound of the behavior of the cylinder is provided by the thin part and because the difference between the partially released stresses of Figs. 3.4f and g, second row and the locked-in stresses of Figs. 3.3c and d, second row, it was decided to simulate the more severe case of Figs. 3.3c and d.

In the analysis of the model SR5TS only the locked-in state of stress was considered together with an imperfection equal to 6.5 times the shell thickness (equal to the measured imperfections). This initial state of stress was simulated using a temperature distribution which is active only in the s direction, has a linear gradient across the thickness t, and is constant along the r direction of the tube.

Using Eq. 3.2, one can derive the value of the maximum strain to be achieved in a cylinder over the circumferential direction, s, when a flat plate is transformed to a cylinder of radius R, without springback. For the thin part (thickness t = 0.76 mm) and for the thick part (thickness t = 1.52 mm) the values for the maximum strains, using a radius, R, of 190.00 mm, are 0.002 and 0.004, respectively. These values are considerably larger than the yield strain ϵ_{sy}. Consequently, for the expansion coefficient of steel α = 11.7 X 10^{-7} / ^{0}C, the maximum temperatures needed to simulate the initial strains are 171 ^{0}C and 342 ^{0}C for the thin part and for the thick parts, respectively. The temperature distribution gradients used are described in Fig. 3.5 both for the thin and for the thick tube parts.

In Fig. 3.6 are shown the locked-in stress distribution of Fig 3.3c, second row, the obtained initial stress distribution using NISA80 with temperature gradient alone, and the locked-in stress distribution obtained in the thin part as a result of the forming process of the cylinder with

both the thick and the thin plates welded together before rolling, and with free springback.

3.3 Analysis with Locked - in Transversal Stresses and Full Imperfections

Model SR5TS used in this analysis contains full size measured imperfections (6.5 times the thickness) and a locked - in transverse stress distribution due to cold rolling without springback allowed (Fig. 3.3). Due to cold forming, 62.8% and 25.8% of the shell thickness is plastified in the thick and in the thin parts, respectively. These locked-in transverse stresses were obtained by using the temperature distribution shown in Fig. 3.5 in an initial step without any external load. After the locked - in state of stress of Fig. 3.3c,d was obtained, the process of loading with external forces was started.

The loading response is linear up to 9 kN, as one can see in Fig. 3.7 where the load deflection curve is plotted for node 58 located at the top of the loading edge. An important reduction in stiffness takes place above 18.73 kN and the structure attains its critical load at 19.80 kN. At this level of loading the structure buckles in a shear mode as one can see in the deformed mesh plots of Fig. 3.8. The deformed mesh in the postbuckling range is shown in Fig. 3.9. Along the postbuckling path the buckles increasingly deepen.

In the postbuckling range the lateral displacements increase at a larger rate than the vertical displacement at the loading edge and the level of tensile principal stresses in the thin test span increases at some Gaussian points in spite of the reduced external load level. This aspect is fully discused in chapter 5.

At a very small load level local unloading and increasing strains are observed at many Gaussian points. With the increase of the load level, the degree of plastification increases at many Gaussian points. It is interesting to note that full plastification is attained only in the postbuckling range in elements located on the diagonals of the thin shell both in tension and compression.

Lateral displacements in the shear buckled area plotted in Fig. 3.10 to 3.12, show that buckling takes place. The most representative plot is the lateral displacement (the amplitude of a buckle) at node 217 which is very similar to the buckling path for imperfect structures plotted in Fig. 1.3a.

The top compressed area was investigated to see the presence of the bending buckles (compression buckles). The plots of Fig. 3.13 show the start of the development of the compression buckles in the postbuckling range. This is inferred from the fact that the points in a small area have up and down relative displacements.

The load deflection path in the postbuckling range (Fig. 3.7), shows a constant load at a lower level. A very

small relative increase in load was noted in the postbuckling range.

Table 3.1 Summary of Locked-in Stress-Strain State at 190 mm Bending Radius

Model	Thickness mm	Radius mm	Long. Yield Stress MPa	Circumf. Yield Stress MPa	Maximum Long. Strain mm/mm	Maximum Circumf. Strain mm/mm	Long. Bending Moment N.mm/mm	Circumf. Bending Moment N.mm/mm
SR	0.76	190	112.5	341.1	0.00066	0.002	13.30	40.20
SR	1.52	190	112.5	341.1	0.00133	0.004	62.00	188.00

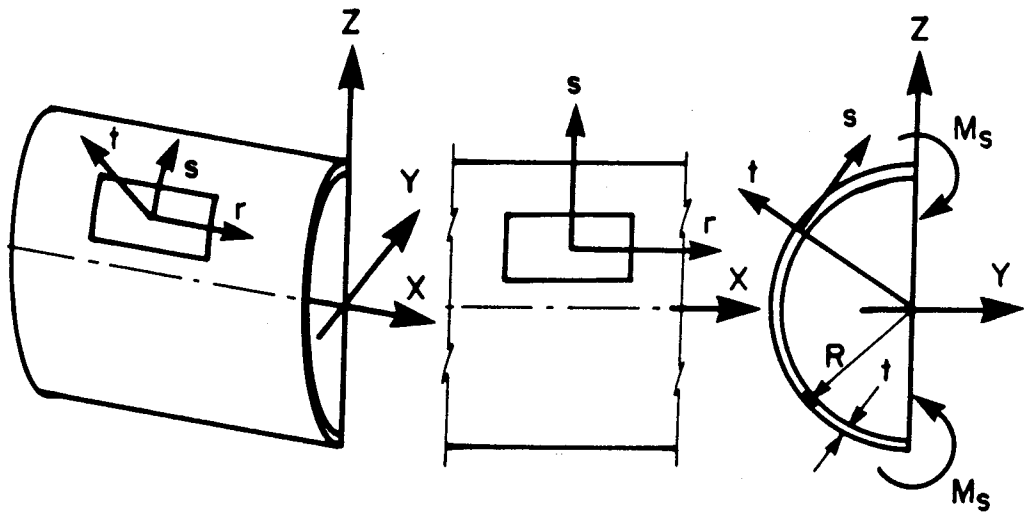

Figure 3.1 Coordinate Description for a Surface Element

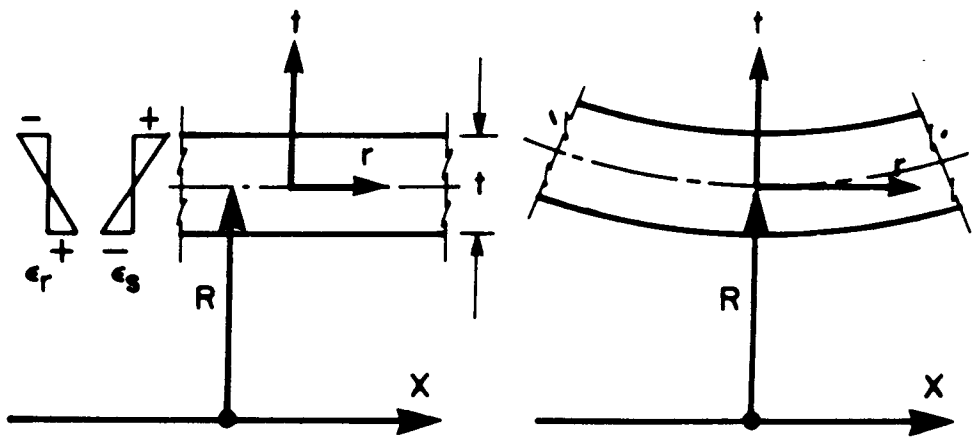

Figure 3.2 Coordinate Description and Strain Distribution

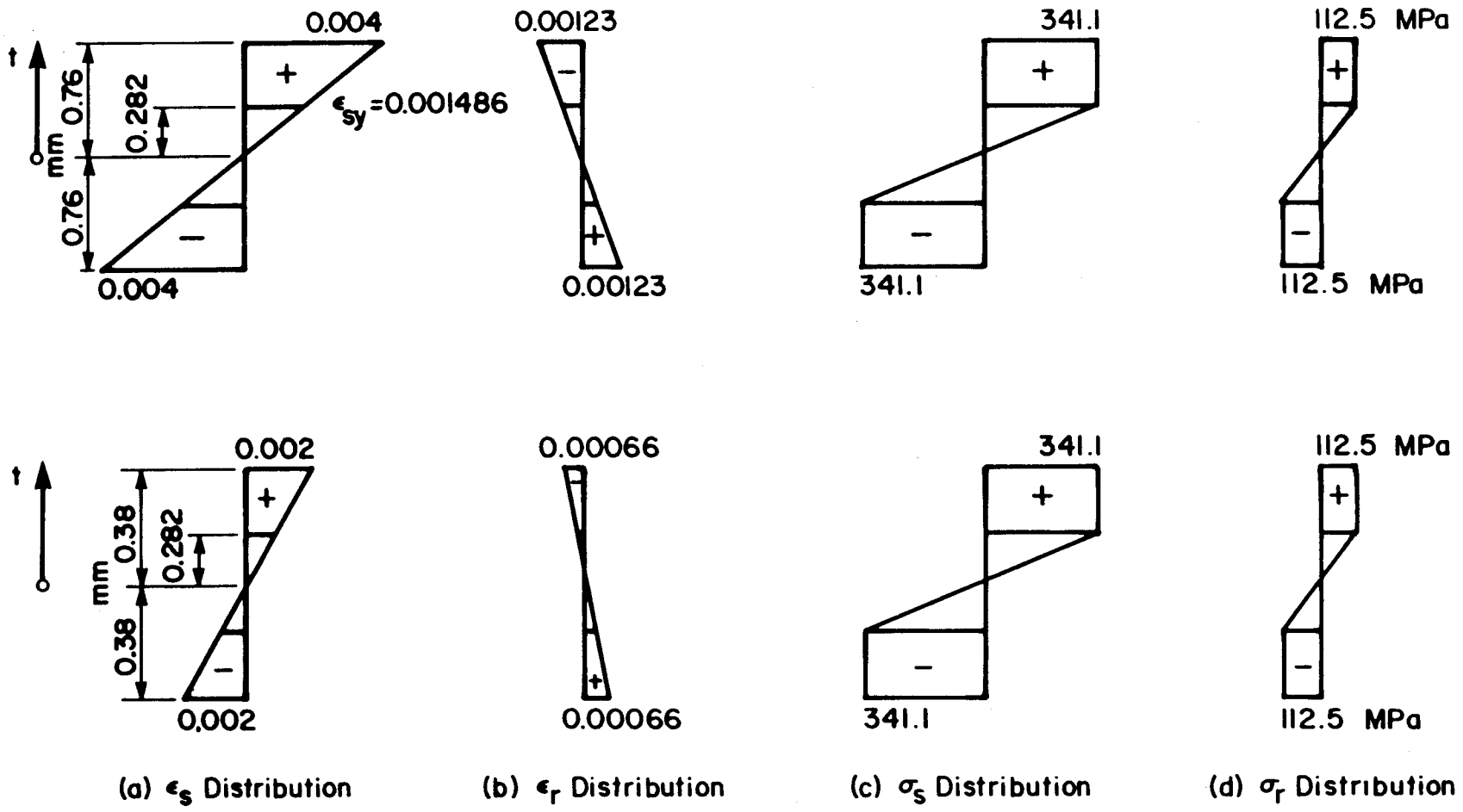

(a) ϵ_s Distribution (b) ϵ_r Distribution (c) σ_s Distribution (d) σ_r Distribution

Figure 3.3 Stress and Strain Distribution due to Cold Forming

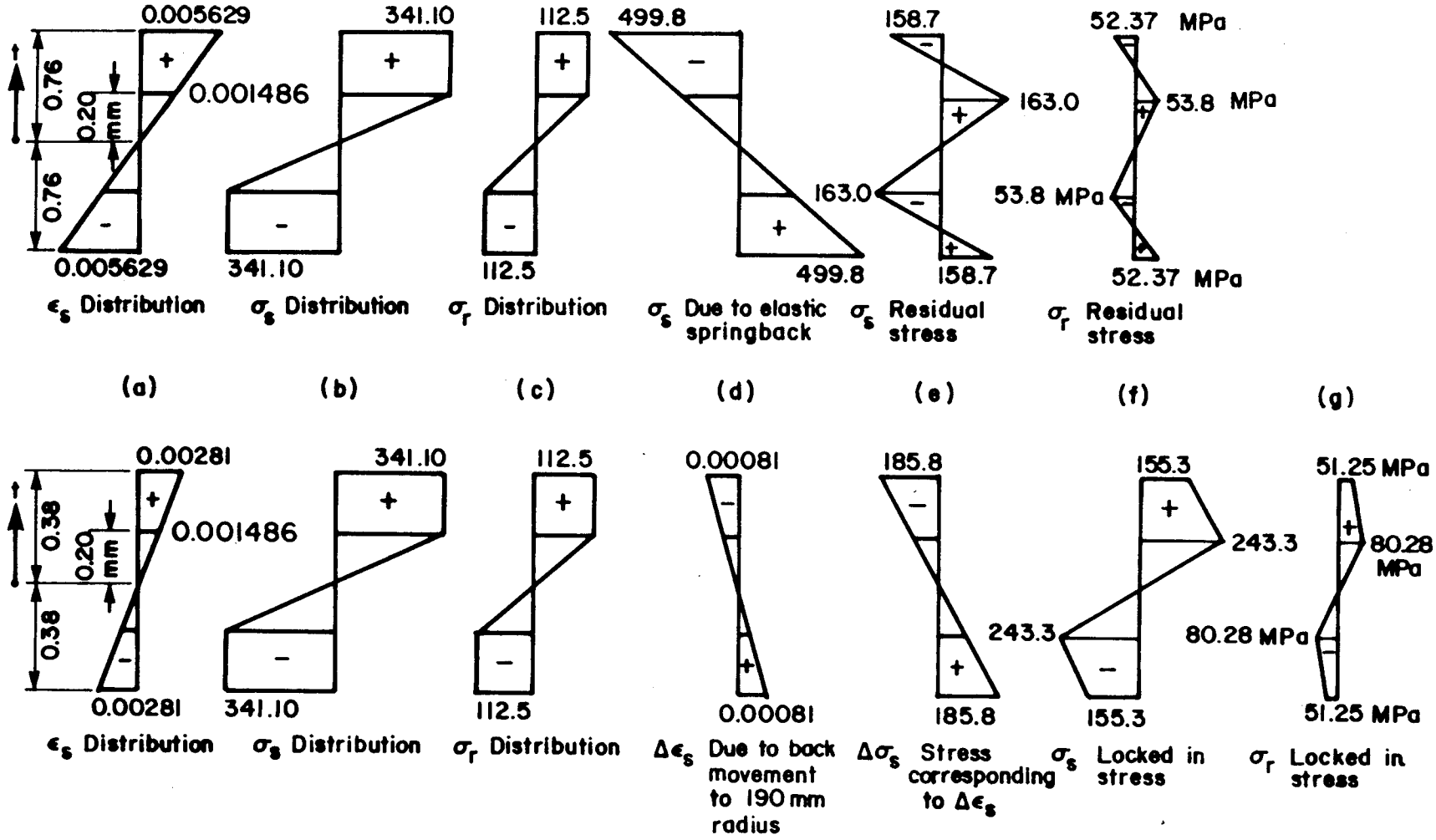

Figure 3.4 Stress and Strain due to Cold Forming with Free Springback to 190 mm radius

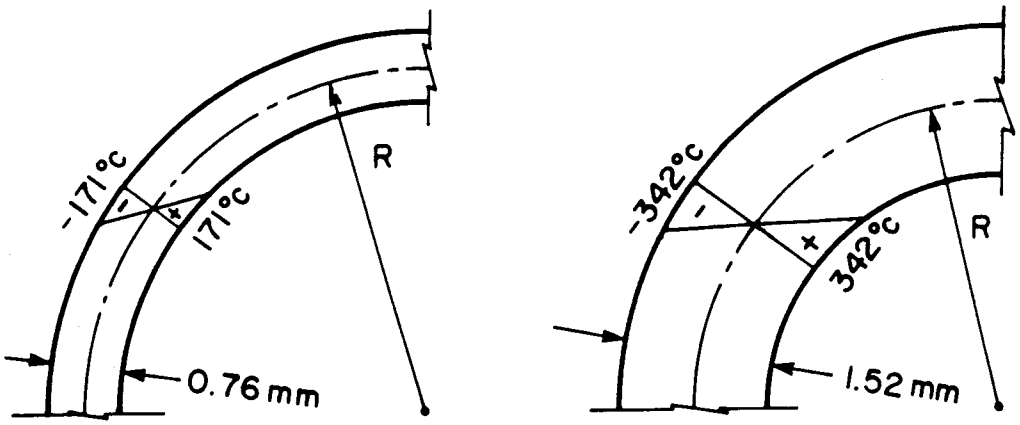

Figure 3.5 Temperature Gradients used in Model SR5TS

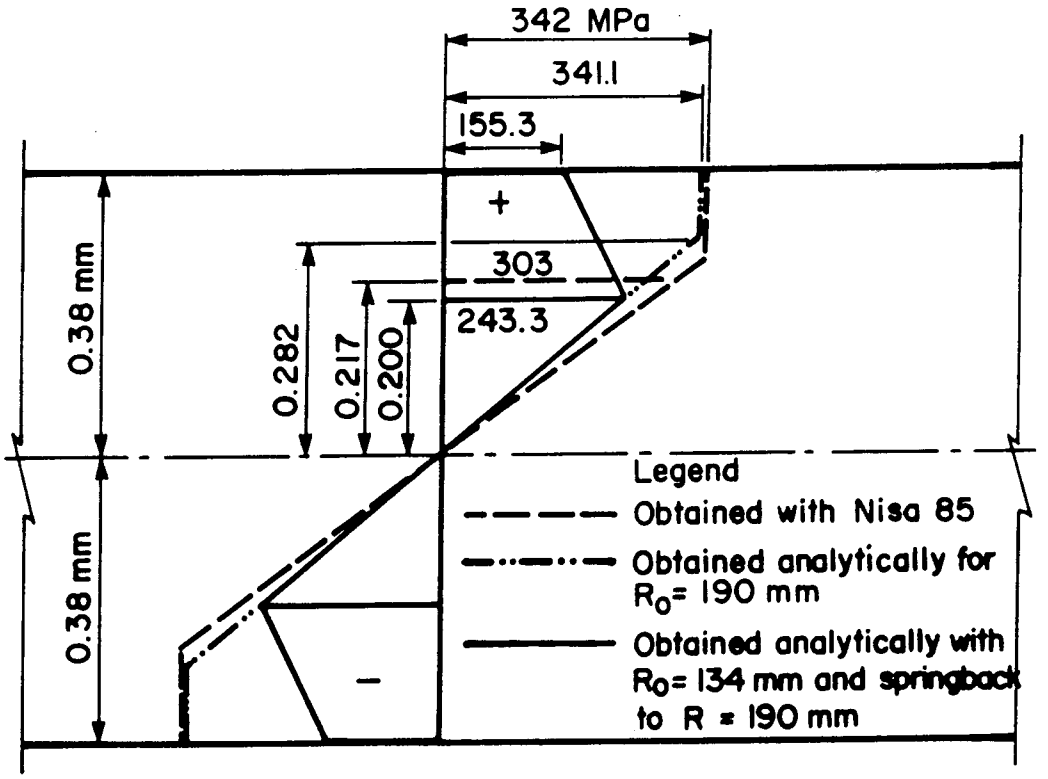

Figure 3.6 Stress Distribution in the Thin Cylinder

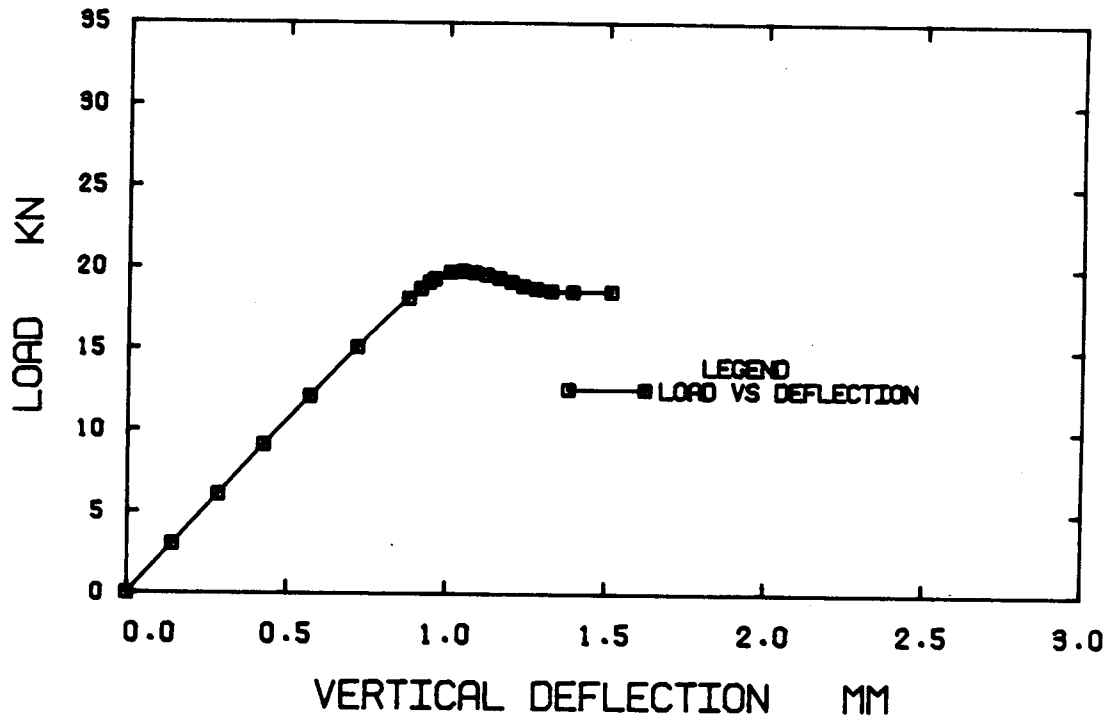

Figure 3.7 Model SR5TS - Load vs Deflection

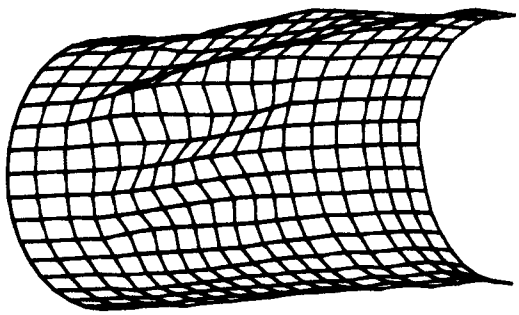

Def. Shape at 18.73kN

Magn Factor=50

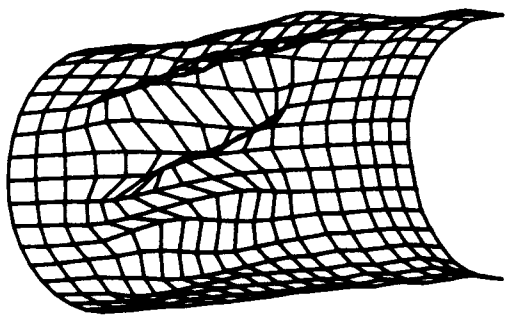

Def. Shape at 19.80kN

Magn Factor=50

Figure 3.8 Deformed Meshes at Different Load Levels on the Prebuckling Path of the Model SR5TS

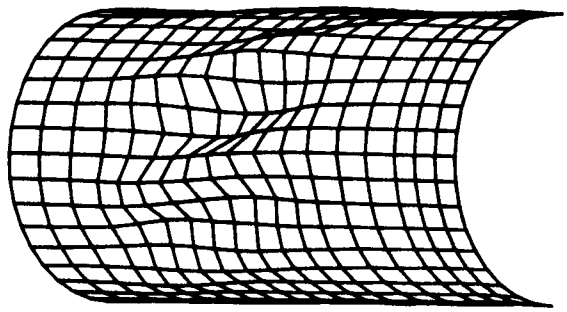

Def. Shape at 18.70kN

Magn Factor=10

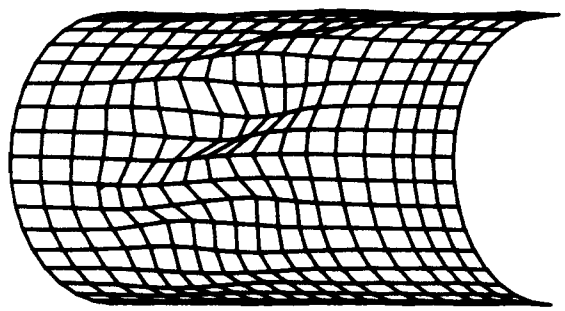

Def. Shape at 18.59kN

Magn Factor=10

Figure 3.9 Deformed Meshes in Postbuckling Range of the Model SR5TS

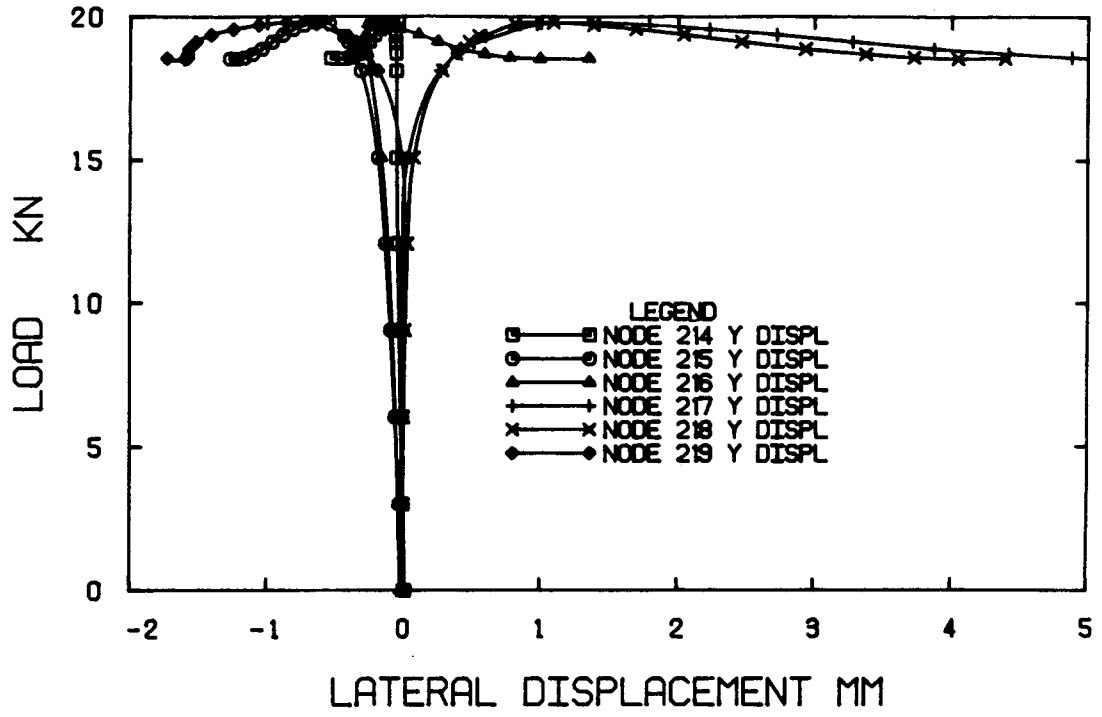

Figure 3.10 Load vs Lateral Displacements

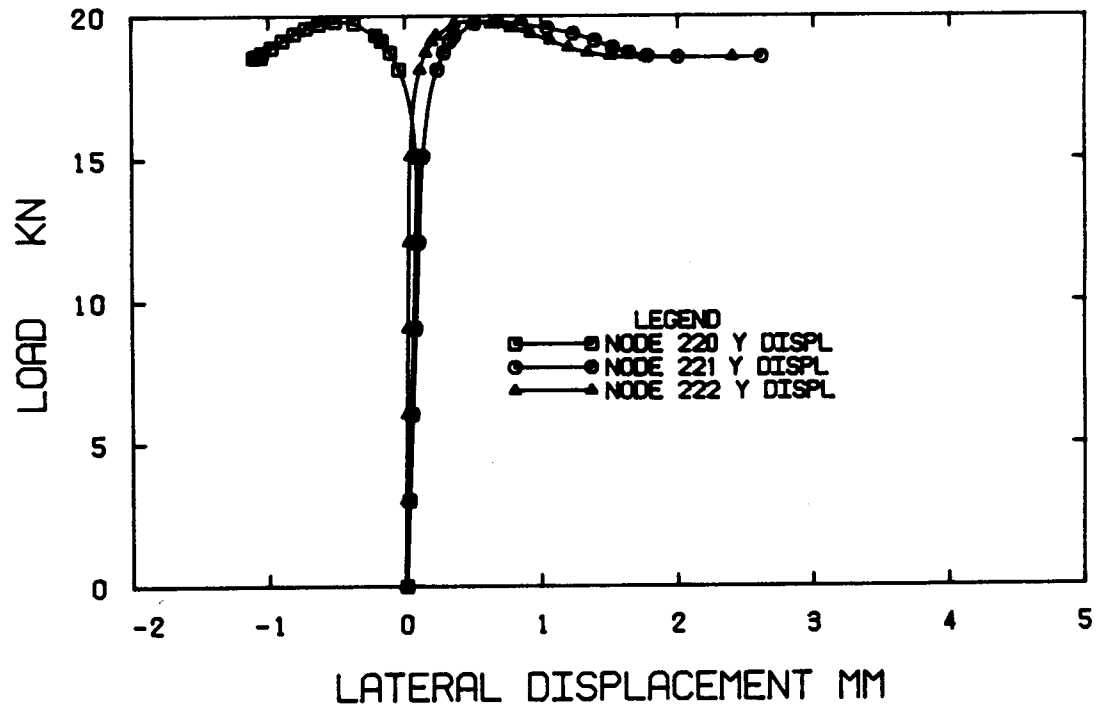

Figure 3.11 Load vs Lateral Displacement

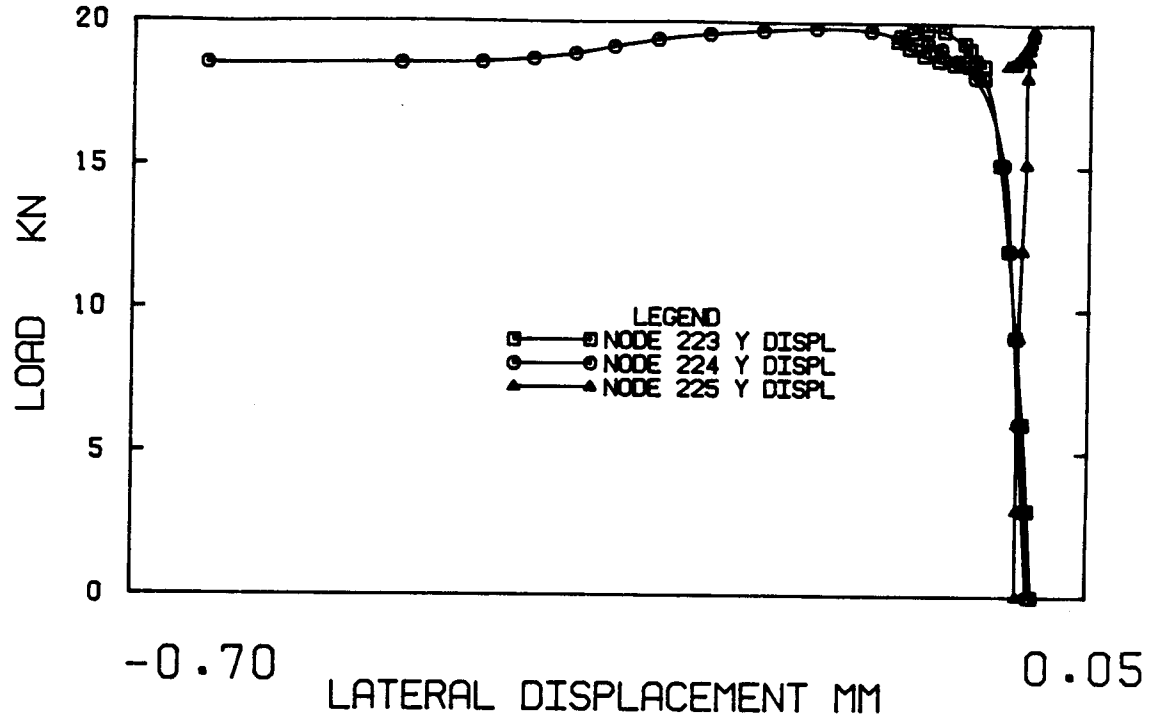

Figure 3.12 Load vs Lateral Displacements

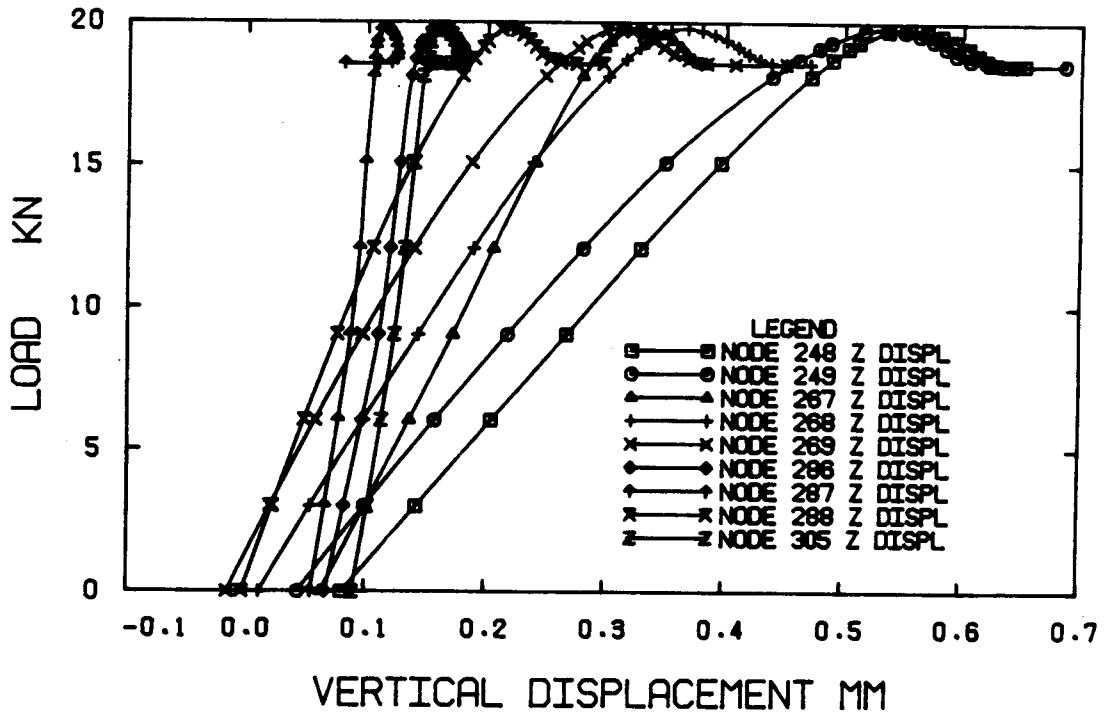

Figure 3.13 Load vs Vertical Displacements

4. Effect of Weld Residual Stresses

4.1 Introduction

Residual stresses are induced in fabricated steel structures by various causes such as welding, cold forming, machining, local heating, and differential cooling after hot rolling.

Strong variable temperature gradients induced in structures and plasticity of the materials are the cause of residual stresses due to welding. Masubuchi (1980) published an ample survey related to the residual stresses induced by welding. He described several analytical and experimental procedures to evaluate the residual stress patterns. The results presented by Masubuchi (1980) are generally obtained by using sophisticated programs and a good experimental data base.

For a reliable analysis of residual stresses and distortion in welds, Masubuchi suggests the following steps in analysis:

1. Heat flow analysis,
2. Analysis of transient thermal stresses during welding,
3. Determination of the incompatible strains after the weldments cool to the initial temperature,
4. Determination of the residual stresses and distortion due to the enforcement of strain compatibility. The incompatible strains are confined to small regions near the weld zone. Therefore, using simple distributions of

incompatible strains may provide reasonably-accurate results (Masubuchi 1960,1980).

The welds used in the fabrication of the cylinders are longitudinal and cicumferential. Weld shrinkage gives a tensile stress equal or close to the yield stress in the weld and in a small area of the base metal, and compressive stresses over the rest of the cross section.

Bushnell (1985) states that the residual stresses due to circumferential shrinkage are able to reduce the buckling load by about 10%. An explanation is that the circumferential weld induces an axisymmetric imperfection besides the initial stress.

Model SR6LS used in this analysis has the geometry, boundary conditions, and the external load of series SR, described in Section 2.2. The mesh is also 6 X 6, but irregular in both the x and z directions. In the x direction the mesh has the same pattern of the SR series, but in the z direction it has the pattern shown in Fig. 4.2. A narrow row of elements was used at the top cylinder to allow describing of the tension yield stress in the longitudinal weld and the adjacent base metal. The model contains also the full imperfection of model SR5.

4.2 Longitudinal Welding Residual Stresses

Masubuchi (1960) described the procedure used to derive the residual stresses due to welding shrinkage. The core of this procedure is to approximate the distribution of the

incompatible strains produced in a region near the weld due to the weld shrinkage.

Model SR6LS considered in this analysis has a longitudinal seam at the top meridian. The width of the affected zone, where there is yield in weld and base metal, is found to be 0.13 R, where R is the tube radius, according to the plot of Fig. 2.15 of Chen and Han (1985). Nagaraja and Tall (1961) conducted experiments on the residual stress in welded plates. According to their findings for a steel plate having a thickness of 6 mm the width of the yielded zone along the welding is approximately 25 mm.

It is assumed in this study that considering an incompatible longitudinal strain over this width is close to the real conditions. Consequently, a constant distribution of the incompatible strain was considered along the s direction on a width equal to 25.4 mm.

Once more this is a plain strain problem. Therefore, to have yielding in the weld and adjacent base metal it is necessary to consider a yield strain value of 0.001486 as given by Eq. 3.8. Fig. 4.1 shows the assumed distribution of the incompatible strain.

According to Masubuchi (1960) the residual stress can be obtained using the equation

$$\sigma_x = - E \, \epsilon_x^{"} + \frac{M_y^*}{I_y} z + \frac{P_x^*}{A} \qquad [4.1]$$

in which x, y, and z are the global axes, σ_x is the residual

stress, E is the Young's modulus, $\epsilon_x^{"}$ is the incompatible strain in the x direction, A is the cross sectional area, I_y is the moment of inertia of the section around the neutral axis, P_x^* is the apparent shrinkage force given by

$$P_x^* = \int\int E \epsilon_x^{"} dy\, dz \ , \qquad [4.2]$$

and M_y^* is the apparent shrinkage moment given by

$$M_y^* = \int\int E \epsilon_x^{"} Z\, dy\, dz \qquad [4.3]$$

For the thick part of the cylinder (for half the section) the area, A, equals 911 mm^2 and the moment of inertia, I_y, equals 16,574 X 10^6 mm^4.

Using all the above data and equations one obtains the residual stress distribution of Fig. 4.1. These initial residual stresses were implemented in the calculation using initial strains due to a constant unidirectional temperature along the r direction and a stepped variation along the s direction as can be seen in Fig. 4.2.

The numerical analysis gives the residual stress distribution shown in Fig. 4.3 for the thin part as well as for the thick part. It can be seen that there is a good correlation between the analytical and numerical distributions, especially in the thin part of the cylinder which is of interest in the analysis.

4.3 Analysis with Longitudinal Residual Stresses and Full Imperfections

Model SR6LS used in this analysis contains full size measured imperfections and a longitudinal residual stress induced by the longitudinal weld shrinkage. The distribution of the residual stress is shown in Fig. 4.2 together with the temperature distribution used to simulate the longitudinal residual stress in the cylinder. The first run, with only longitudinal temperature, resulted in the stress distribution in the cylinder shown in Fig. 4.3. It is noted that the magnitude of the displacements due to the temperature distribution is of the order of the shell thickness and that the initial imperfection pattern was changed. The stress distribution obtained by numerical analysis is close to that obtained analytically (Fig. 4.2). The external load was then applied and the attained critical load was 31.83 kN, which is bigger than the critical load of model SR5, which has only the full imperfection. This is due to the change in the initial imperfection distribution caused by the assumed temperature distribution. The equilibrium path of the top loading edge (node 58) is practically linear up to 31.0 kN (Fig. 4.4) in spite of the first plastification appearance at 29.61 kN load level, on one of the diagonal elements.

A buckling analysis carried out at an advanced load level (18 kN) gave a buckling load equal to 28.28 kN, which is lower than the achieved critical load (31.83 kN). This

reduction in the calculated buckling load is due to the residual stress and the initial imperfection. The structure was able to carry a larger load than the buckling load, though. The buckling shape (Fig. 4.5) shows a failure by local bending buckling at the middle top of the test cylinder. In spite of this predicted failure mechanism the deformed shape at the critical load (Fig. 4.5) shows a failure by shear buckling, which is more emphasized in the postbuckling range (Fig. 4.6). The lateral displacements in the shear buckling zone show clearly that buckling takes place, especially the equilibrium path of node 219 (Figs. 4.7 and 4.8).

The equilibrium paths of the top nodes are shown in Figs. 4.9 to 4.12. These figures show the vertical displacements of the nodes at top of the cylinder and at successive longitudinal rows. Because of the absence of a clear wave formation with inward and outward motion one can infer that local bending buckling does not take place. This may be explained by the high level of tension stress induced by the weld shrinkage in this area, which allows a higher level of loading in compression due to the external loading and consequently postpones the bending buckling to a higher level of deformation in the postbuckling range.

4.4 Circumferential Welding Residual Stresses

The weld shrinkage is thought in literature to be around two times the yielding strain (Lay, 1982). Unlike the case of longitudinal shrinkage the resistance of the cylinder to circumferential shrinkage is small. In this situation, larger initial axisymmetrical deformations can be expected with their consequences on the critical load level. The same approach used for longitudinal welds can be applied. A constant unidirectional negative temperature (constant over the thickness) over the s direction would be able to simulate the circumferential weld shrinkage. This feature was not investigated in this study.

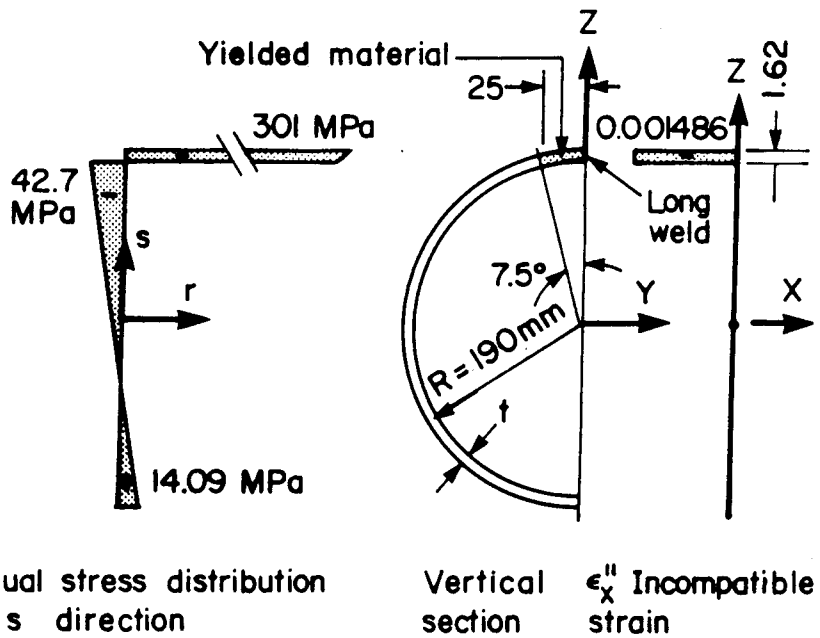

Figure 4.1 Residual Stress Distribution from Longitudinal Weld Shrinkage

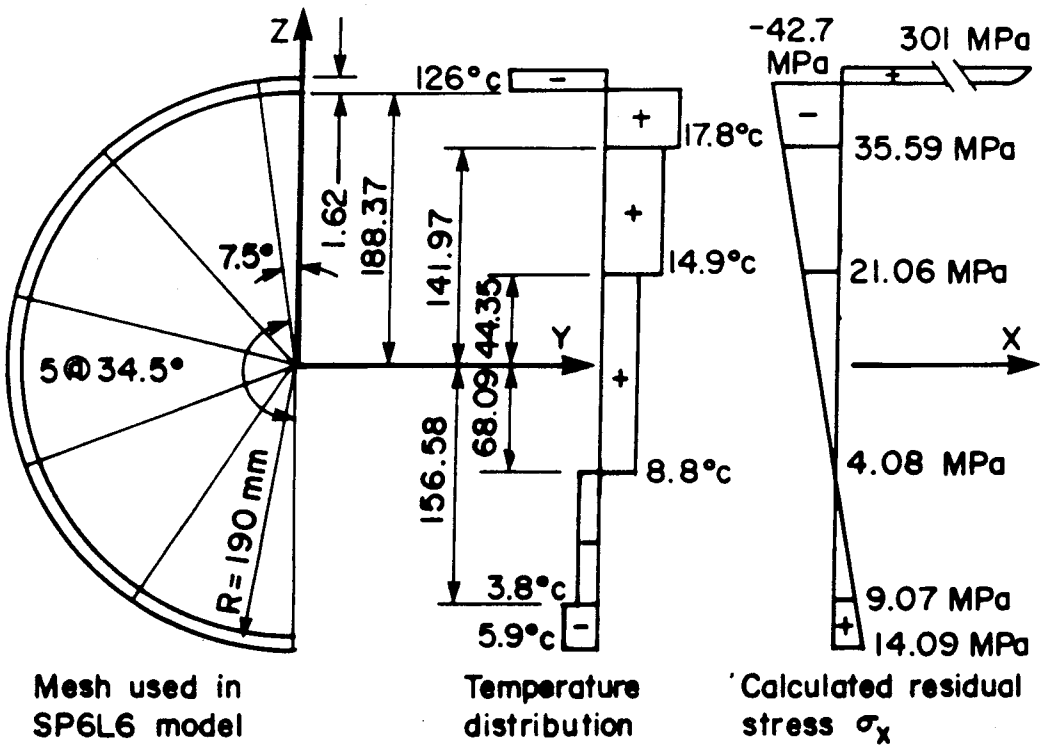

Figure 4.2 Residual Stress and Temperature Distribution

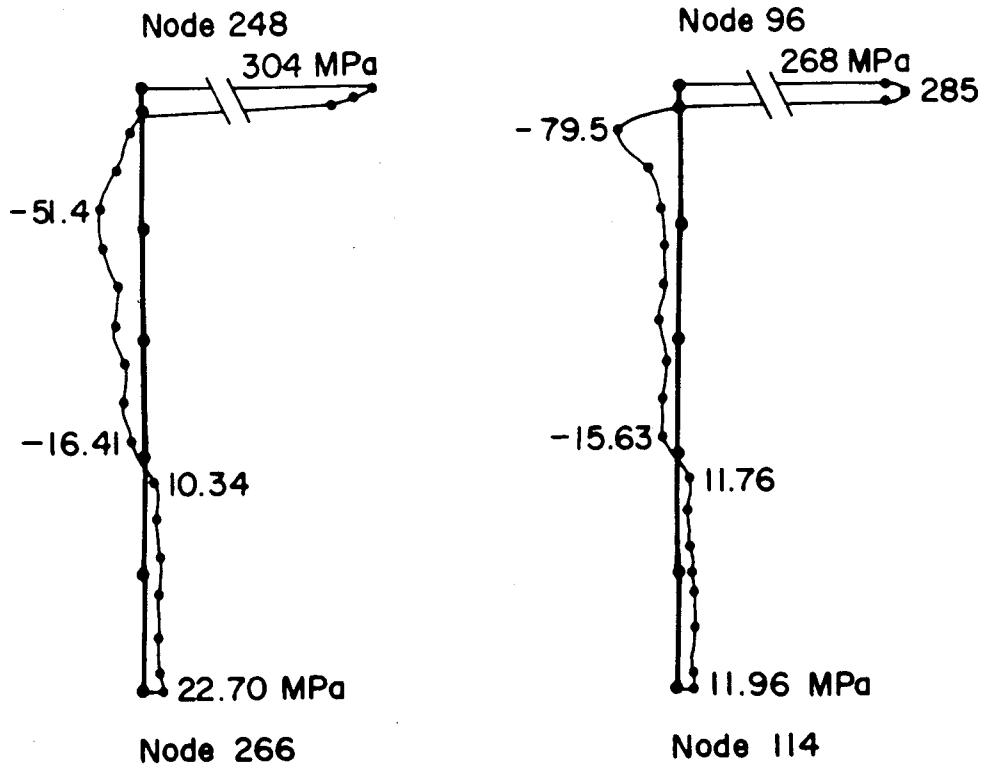

Figure 4.3 Stress Distribution for Temperature Distribution of Fig. 4.2

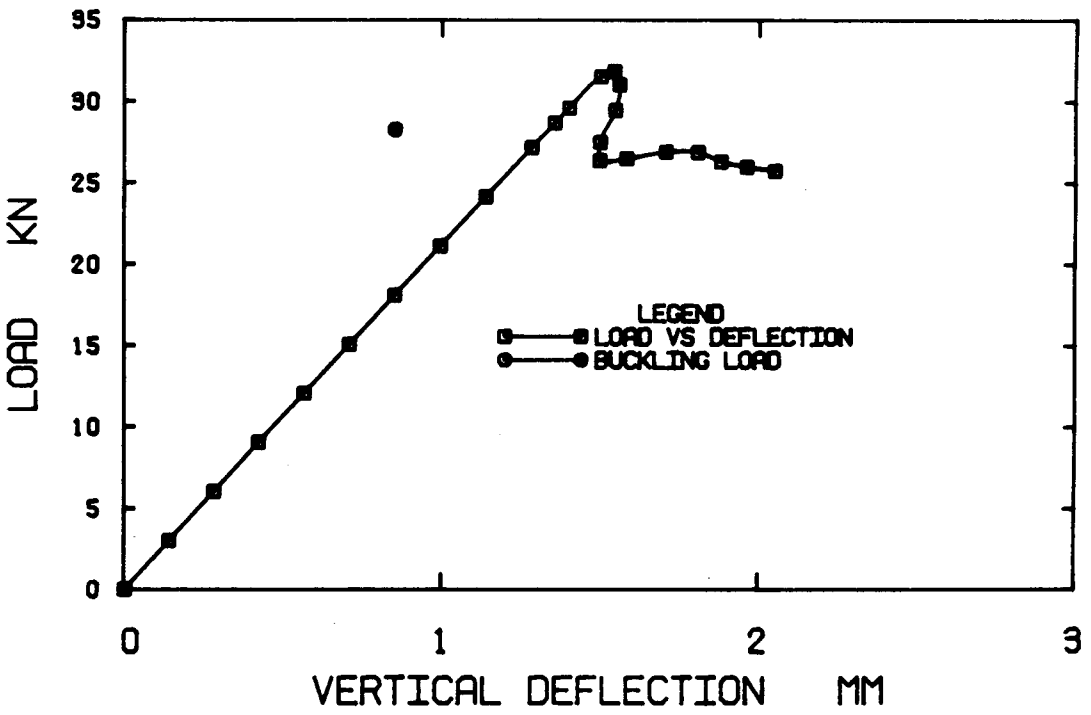

Figure 4.4 Model SR6LS - Load vs Deflection

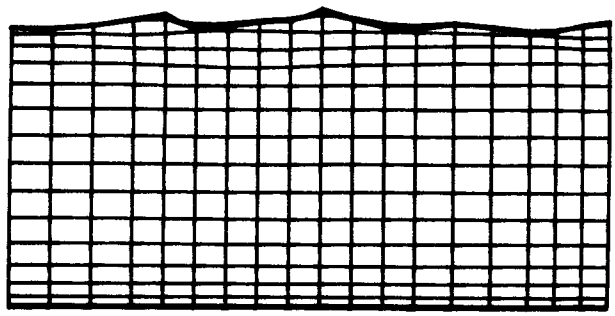

Def. Shape from Temp.
Magn Factor=200

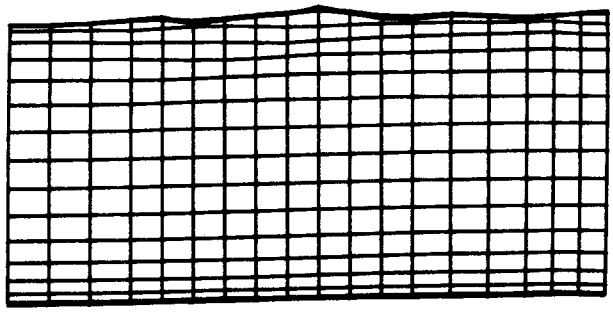

Def. Shape at 18.12kN
Magn Factor=100

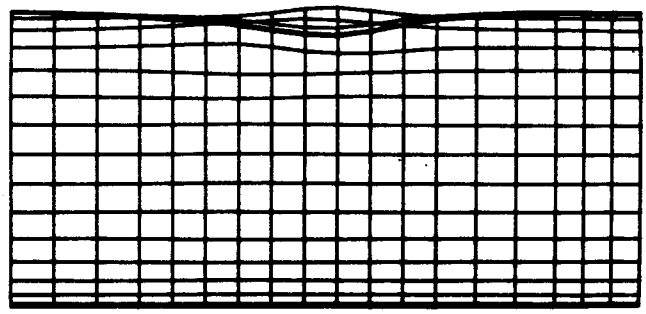

Buckl. Shape at 18.0kN
Buckling Load=28.8kN
Magn Factor=500

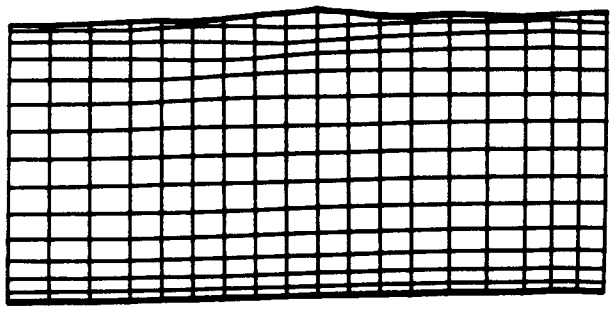

Def. Shape at 29.61kN
Magn Factor=100

Figure 4.5 Deformed Shapes and Buckling Modes of Model SR6LS on the Prebuckling Path

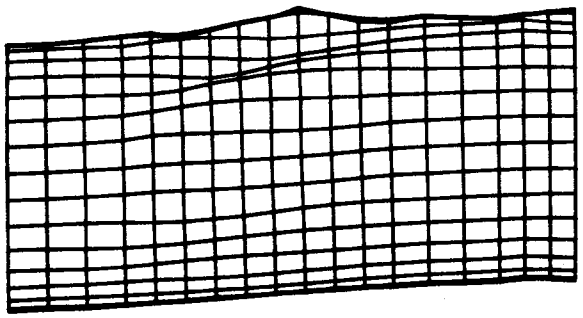

Def. Shape at 31.85kN

Magn Factor=50

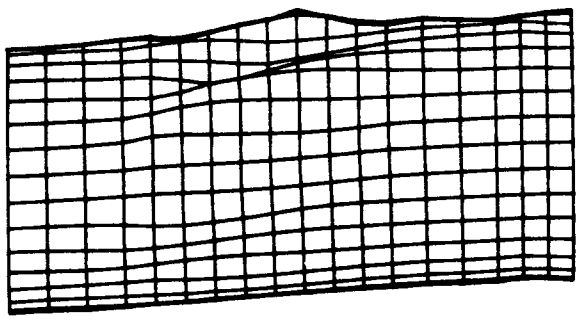

Def. Shape at 31.03kN

Magn Factor=50

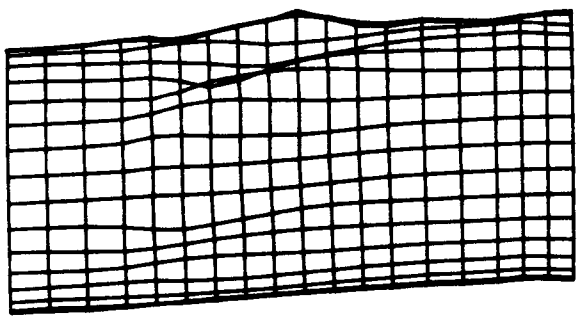

Def. Shape at 29.47kN

Magn Factor=50

Figure 4.6 Deformed Shapes in the Postbuckling Range of the Model SR6LS

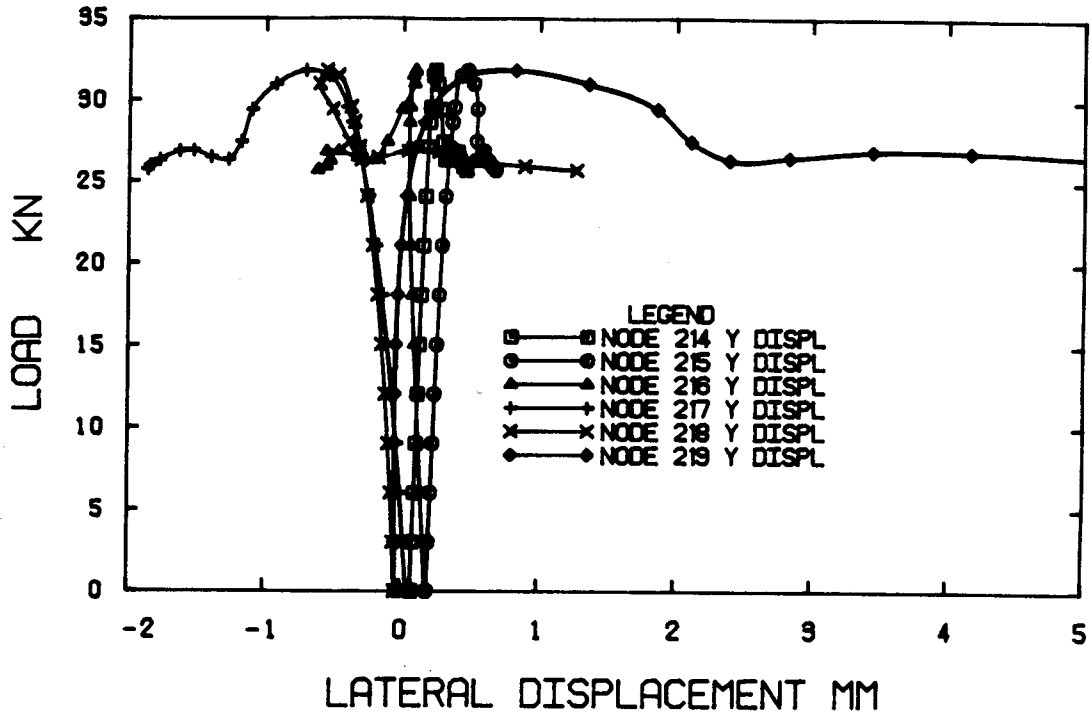

Figure 4.7 Load vs Lateral Displacements

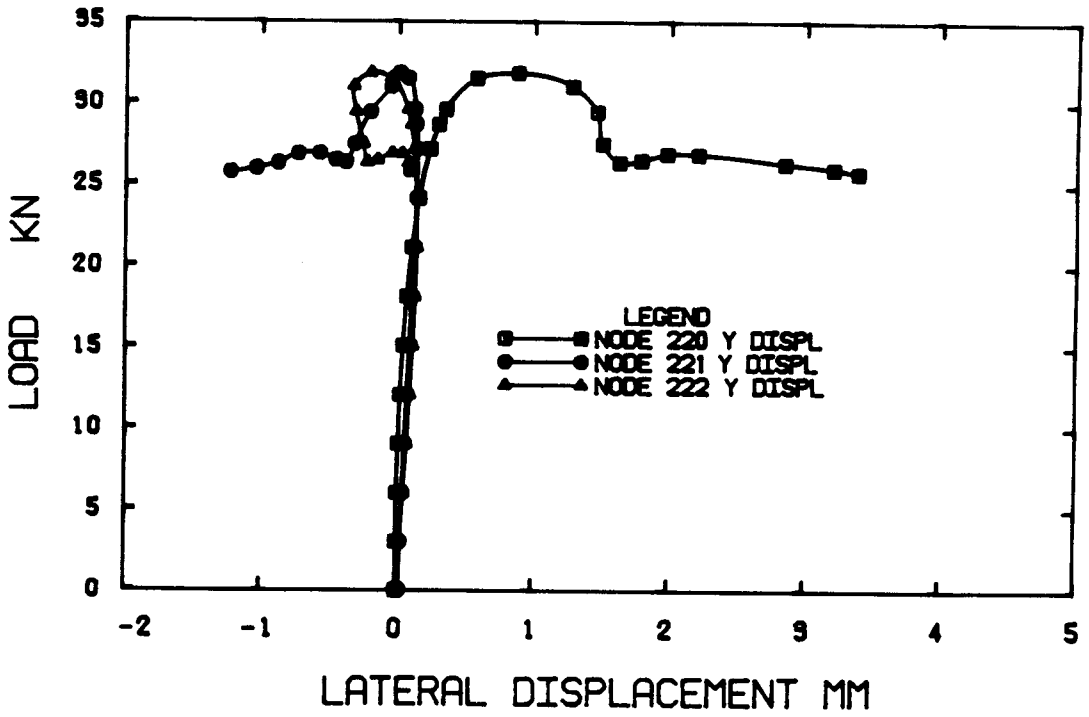

Figure 4.8 Load vs Lateral Displacements

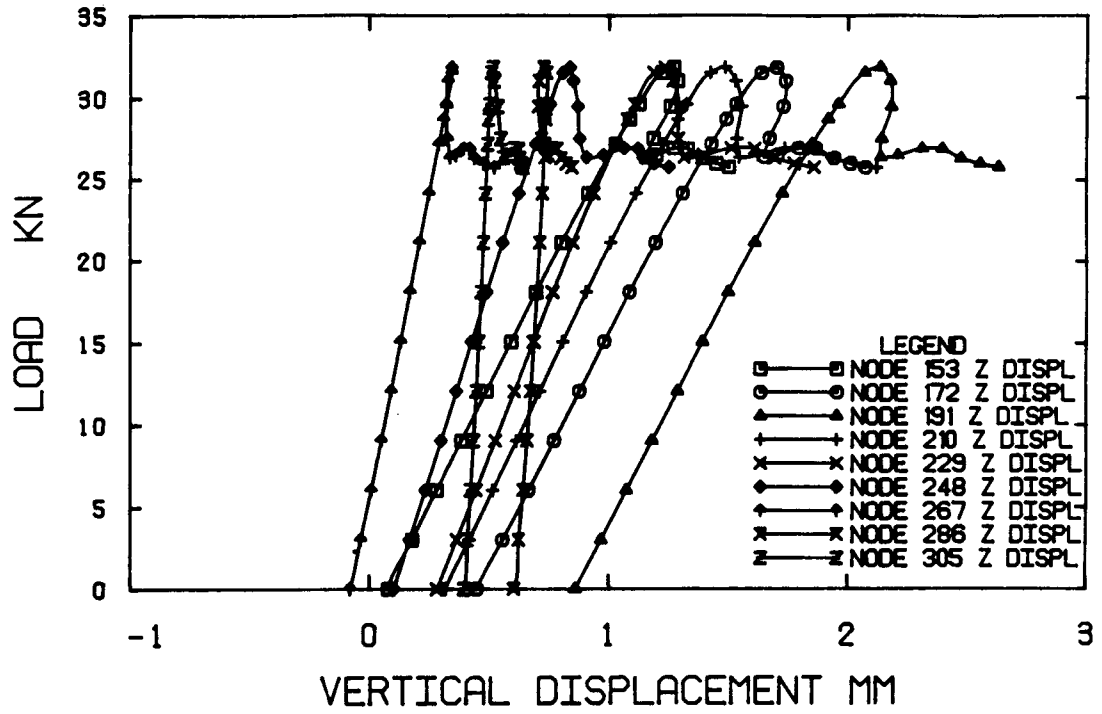

Figure 4.9 Load vs Vertical Displacements

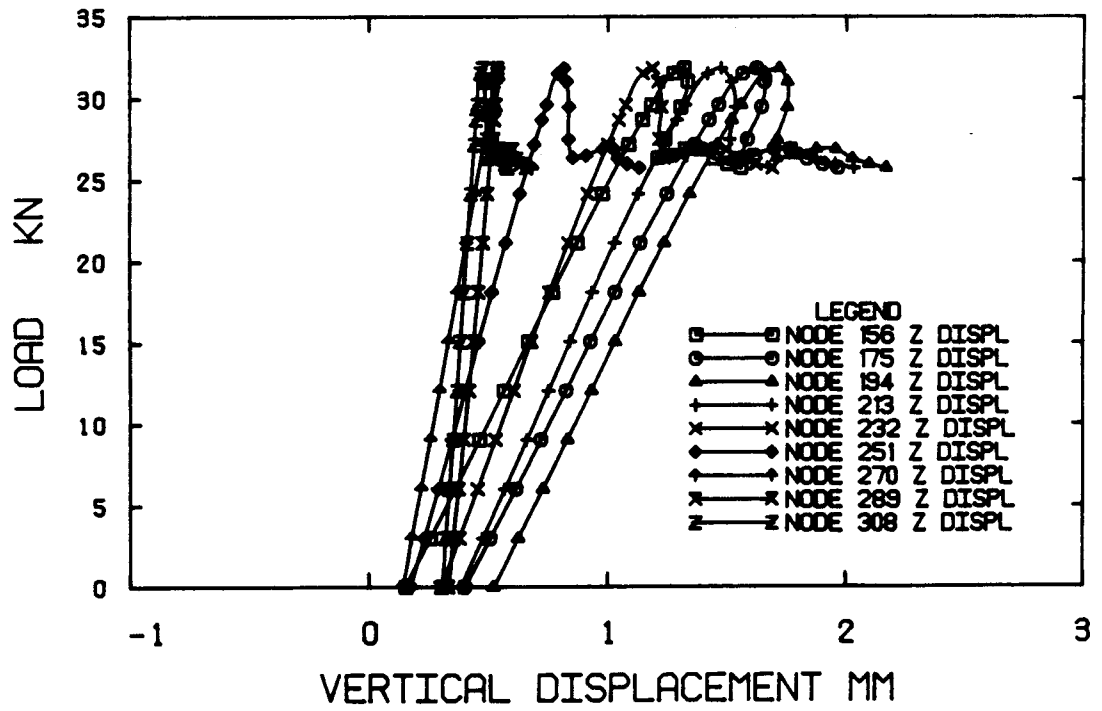

Figure 4.10 Load vs Vertical Displacements

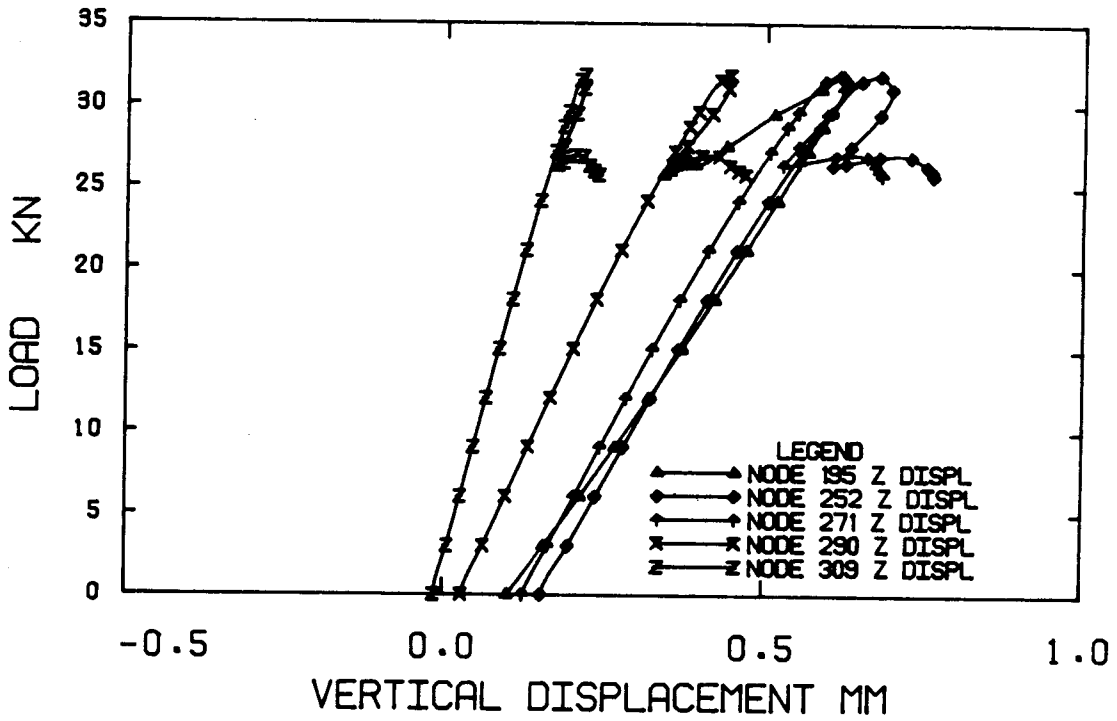

Figure 4.11 Load vs Vertical Displacements

5. Discussion

5.1 Introduction

In this study, the effect of measured imperfections on the shear response of large diameter steel cylinders has been investigated by itself as well as in the presence of cold bend fabrication stresses and longitudinal seam weld residual stresses. In all cases it was found that shear buckling occurs followed by sharp unloading, except in the case of cold bend locked-in stresses; model SR5TS, section 3.3. The postbuckling behavior, however, for all models is characterized by a load deformation response which maintains a constant load at large deformations; three or four times the buckling deformation.

Determination of the postbuckling stable load level and its carrying mechanism is important for design purposes as well as for determination of the ultimate failure mechanisms.

Bailey and Kulak (1984) suggested the presence of a tension field in cylinders under transverse shear in the postbuckling range provided the following assumptions hold:

1. The longitudinal stress in the tension field is that corresponding to the stress at which the cylinder would buckle in flexure.
2. The angle of the tension field inclination is found using plate girder equations.
3. The shape of the tension strips is assumed to be

elliptical.

4. The stress in the tension field strips is constant.

They considered a continuum tension field, and using Basler's hypotheses (Basler, 1961) and procedures, an expression for the angle of the tension field was obtained.

Elwi and Mok (1986) carried out an investigation of the tension field development using the available data from prebuckling analyses of the cylinders under shear. Their develcpment is based on Basler's hypotheses and procedures, considering an elliptic shape for the continuum tension field strips. They obtained an expression for the allowable tension stress in the tension field, based on the von Mises' yield criterion, and the critical shear expression given by Batdorf(1947). Their process is not unlike that of Bailey and Kulak (1984).

In this chapter a similar approach is developed but based on slightly different assumptions, and on postbuckling behavior of the cylinders under shear.

5.2 Summary of the Behavior of the Cylinders under Shear

The dominant features of the behavior of the cylinders under transverse shear based on the numerical analyses of the SR models, described in detail in chapters 2,3, and 4, are summarized in the following.

The stiffness of the prebuckling paths for all models, regardless of the size or shape of the initial imperfections, and of the residual or locked-in initial

stresses, are practically the same as one can see in Fig. 5.1. After reaching the critical load sharp unloading takes place, except for the model SR5TS, which simulates the behavior of a locked-in state of stress.

The postbuckling paths tend to follow a common path in the postbuckling range. The model SR5TS, with locked-in stresses, shows a soft peak. The postbuckling path decreases with rapid stabilization on a practically constant lower load level, Fig. 5.1.

At the critical load a shear buckling mode is displayed by all SR models. The best description of buckling is given by the equilibrium paths of the points located on the shear waves. In Fig. 5.2 the lateral displacements versus loads for these characteristic points (node 217 for models SR1, SR4, SR5, SR5TS, and node 215 for SR6LS), are plotted. From these equilibrium paths, which practically describe the variation of the buckle amplitude versus load, one can infer that the postbuckling response of the cylinder under shear is that described by Fig. 1.3a. It is largely accepted (Brush and Almroth, 1975) that imperfect shells follow the postbuckling path of the perfect shell in the postbuckling range. In Fig. 5.2 one can see that the equilibrium path of the nearly perfect shell SR1(0.01t initial imperfection) (dotted line) is closely followed by all the other models which have initial imperfections only. The initial measured imperfections have a moderate influence on the magnitude of the critical loads. Galletly and Blachut (1985) carried out

experiments on buckling of cylinders under shear and obtained a similar conclusion. In Fig. 5.3 the ratio of the critical load, obtained by numerical analysis, to the classical buckling load (obtained by buckling analysis of the cylinder with very small initial imperfections and with low load level) is plotted versus the maximum size of the imperfections scaled to shell thickness. The minimum load in the postbuckling range is not sensitive to imperfections or initial longitudinal seam weld residual stresses.

The variation of the ratio of principal tension stress to the principal compression stress is plotted for some Gauss points located in the middle of the thin cylinder, Figs. 5.4 and 5.5. One can see that the ratio, calculated for model SR5, is almost constant, from zero load to a close range of the critical load. This means that the behavior is linear or almost linear up to the critical load and that the shells in the prebuckling path behave like beams. After the critical load is reached and buckling takes place the tension stress for the Gauss points located on the tension bands increases rapidly. Similar conlusions may be drawn from Figs. 5.6 and 5.7 where the ratio of principal stresses is plotted for SR5TS model. One can also see that the initial locked-in stress changes the ratio only at low load levels.

Prebuckling deformations continue to grow under decreasing load at almost all points of the thin cylinder part, except at some of the points located in the shear

buckling area where the buckles deepen and the motion is reversed. Beyond the critical point a significant stress redistribution takes place, especially in the thin part of the cylinder. The principal stresses and membrane forces separate into tensile bands roughly parallel to the buckles. The buckle crests continue to load in tension, while the valleys unload as the buckles deepen. Plastification across the thickness takes place at most points located on the tension bands.

5.3 Tension Field Investigation

The tension field concept is related to the behavior of plate girders under shear. Plate girders under shear develop stable postbuckling equilibrium configurations at higher loads than the critcal loads. Their postbuckling behavior is well described by Fig. 1.3b. The explanation for this favorable behavior is that buckling helps develop a carrying mechanism based on a tensioned membrane which forms the diagonal of a truss panel bounded by the flanges and vertical stiffeners. The load carried in the postbuckling range is much larger than the critical load and is limited by the material yield stress, geometry, and the strength capacity of the flanges and vertical stiffeners.

As mentioned in section 5.1 a similar tension field may appear in cylinders, after shear buckling takes place. The principal stress or membrane force trajectories are close to helix shapes on the prebuckling paths, including the

critical points, for all models as one can see in Figs. 5.8, and 5.10 to 5.13, top plots. One can imagine as a supporting structure, for a thin cylinder in the prebuckling range the helix strips in compression and those in tension, anchored in the vertical sides, created by the thick part of the cylinder. Buckling takes place in the compressed strips and as a consequence, the length of the tension strips diminishes where the inward buckles develop. Consequently, the tension strips are divided into parallel tension bands separated by unloaded bands. This phenomenon is obvious for all models as one can see in all postbuckling stress plots of Figs. 5.8, and 5.10 to 5.13, bottom plots. The angle of of the tension bands changes along the postbuckling path and is not the same as the angle of the buckles. From an initial angle equal to 45^0, before and at the critical load, it reduces to about 25^0 to 29^0, in the postbuckling range. The tension strips cross only the outward buckles.

The presence of a truss carrying capacity can be conceived, by using a simple truss panel, shown in Fig. 5.14, with boundary conditions and loads resulting in shear and bending moment diagrams, in an equivalent beam, similar to those of the SR models.

According to a static analysis of this truss panel, the internal forces and the total shear are,

$$V = T \sin\zeta + C \tan\gamma, \qquad [5.1]$$

$$C_T = - \frac{M_L\ C}{(M_L - M_R)\ \cos\gamma}, \qquad [5.2]$$

$$C_B = \frac{M_R\ C}{(M_L - M_R)\ \cos\gamma}, \qquad [5.3]$$

where C, is the horizontal projection of the tensile diagonal force, T, such that

$$C = T \cos\zeta = \frac{M_R - M_L}{L\ (\tan\zeta + \tan\gamma)}, \qquad [5.4]$$

V is the panel shear, M_L and M_R are the bending moments, C_T, C_B, and T are the internal forces, γ is the angle of the top and bottom chords with the horizontal, and ζ is the angle of the diagonal with the horizontal. The variation of internal forces in the top and bottom chords is very sensitive to the variation of $\tan\zeta$.

This analysis is developed to show that the horizontal projection of the diagonal tension is shared by the compressed top and bottom parts of the cylinder. In the numerical analysis this is shown by the shifting of the zero membrane forces at the section of zero bending moment towards the right handside of the top part of the cylinder, previously subject to tensile flexural stresses and towards the left handside of the bottom part of the cylinder, also previously subject to tensile flexural stresses, Figs. 5.8 to 5.13, bottom part.

5.4 The Tension Field Description

An important aspect that can be noted from all principal membrane force plots, Figs. 5.8 to 5.13, is that the shape of the tension strips is helical. In these plots the principal stresses or principal membrane forces are represented on the developed cylinder surface and the tension strips appear as straight lines (only a helix line appears as a straight line on the developed surface of a cylinder). The angle of the tension strips stays almost constant on the horizontal postbuckling equilibrium path. Starting from this observation, an analytical approach is developed considering a helix as the shape of the tension strips.

Other assumptions considered in the development are as follows:

1. The beam shear strength capacity is completely disabled.
2. The top and bottom parts of the cylinder are able to carry the compressive stress resulting from a truss supporting mechanism.
3. The top and bottom parts of the cylinder are not able to carry any transverse stress, or in other words, cannot offer anchorage for the tension strips.
4. The vertical, circumferential thick rings are able to carry the compression induced by a diagonal tension field (i.e., can offer anchorage to the tension strips).

In Fig. 5.15 the elements of the tension field are described by ζ, which is the angle of the tension field,

measured on the cylinder surface, χ, which is the angle due to the helix form of the tension strip, R , which is the radius, dW, which is the elementary width of the tension strip, ϕ and $d\phi$, which are the angle and the elementary angle, and t, the cylinder thickness.

From the parametric equations of a helix on a cylinder (Love, 1944) the angle χ is equal to

$$\chi = \frac{L}{R} \tan\zeta, \qquad [5.5]$$

and, consequently

$$\alpha = \pi - \chi = \pi - \frac{L}{R} \tan\zeta. \qquad [5.6]$$

For an elementary tension strip the component along the Z axis, the vertical direction, is

$$dV_t = \sigma_t \, t \, dW \cos\zeta \sin\zeta \sin\phi = \frac{1}{2} \sigma_t \, R \, t \sin 2\zeta \sin\phi \, d\phi. \qquad [5.7]$$

Further, one may assume that σ_t is constant over the width of the tension field which leads to an upper bound on the tension field capacity in terms of material yielding. However, the carrying mechanism in a stable postbuckling range is complex. After buckling of the compression strip helices, some of the tension strip helices are unloaded. The outward shear buckles help develop the tension membrane forces, but the inward buckles reduce the forces in the

tension strips, because their length is reduced. This leads to a significant reduction of the beam carrying capacity of the cylinder, but with the increase of deformations along the practically horizontal postbuckling path a stabilization of the equilibrium at lower load levels takes place.

It appears that a separation of the compression strips in compression bands also takes place and the supporting structure can be represented by the complex truss of Fig. 5.16. The compression bands are not as clearly defined as the tension bands. However, they influence the value of the yield stress in tension and compression at the points of band intersections, and they also have their contribution to shear capacity.

Assuming that, the increase of the deformations and the deepening of the buckles along the postbuckling path, may cause the disappearance of the inclined compression bands, the ultimate truss supporting structure may be that represented by Fig. 5.17. This banding phenomenon gives rise to a lower bound on the tension field capacity. The lower bound character is achieved by allowing a continued motion at a constant load such that the crests are continually loading at a constant yield stress and the valleys are continually unloading. Thus one may assume a step wave distribution of σ_t with the crests at σ_Y and the valleys constantly at zero stress. Alternativelly, one can assume a sinusoidal σ_t distribution with zero at valleys and σ_Y at the crests. Both distributions have an average σ_t of $\sigma_Y/2$

over the full width of the tension band. Thus Eq. 5.7 may be rewritten as

$$dV_t = \frac{1}{2}\,\eta\,\sigma_Y\,R\,t\,\sin 2\zeta\,\sin\phi\,d\phi, \qquad [5.8]$$

in which $\eta = 1$ for an upper bound and

$\eta = 0.5$ for a lower bound.

For half the cylinder section, the shear capacity due to the tension field is

$$V_t = \frac{1}{2}\,\eta\,\sigma_Y\,R\,t\,\sin 2\zeta\,(-\cos\phi)\Big|_0^{\alpha}$$

or

$$V_t = \frac{1}{2}\,\eta\,\sigma_Y\,R\,t\,\sin 2\zeta\,(1 - \cos\alpha). \qquad [5.9]$$

For an elementary helical tension strip the horizontal projection is

$$dC = dW\cos\zeta\;\eta\,\sigma_Y\,t\cos\zeta = \eta\,\sigma_Y\,R\,t\cos^2\zeta\,d\phi. \qquad [5.10]$$

For half the cylinder cross section the horizontal projection of the tension field is,

$$C = \int_0^{\alpha} dC = \eta\,\sigma_Y\,R\,t\cos^2\zeta\,\phi\Big|_0^{\alpha} \qquad [5.11]$$

Assumming that the angle ζ takes a value such that V_t becomes an extremum, one can find the value of the angle ζ from the identity

$$\tan 2\zeta = \frac{2R}{L} \left(1 + \cos\left(\frac{L}{R}\tan\zeta\right)\right) \left\{\sin\left(\frac{L}{R}\tan\zeta\right) \sec^2\zeta\right\}^{-1}. \qquad [5.12]$$

For L = 381.0mm, and R = 190.0mm, ζ is found equal to 27^0, which is not far from the measured average values (25^0 for SR1, 27^0 for SR4, 28^0 for SR5, SR5TS) on the principal stress plots. The corresponding "α" value is 122^0. This value is very close to the measured value on all principal stress or membrane force plots, which is 125^0.

5.5 Effect of the Cross Bending Moments

As the degree of deformation increases in the postbuckling range, the buckles deepen and the crests become sharp, having a large curvature. According to the numerical analysis the local cross bending moments that take place accross the buckles are in the range of the plate yield bending moment or bigger. Assuming that the tension bands have the same inclination as the buckles, a biaxial stress states results, which may impose a limitation on the development of the tension stress across the thickness of the tension bands. With the increase of the cross bending moments due to the folding of the buckles a uniform uniaxial tension σ_t across the thickness cannot be developed (Fig. 5.19).

The banded tension field stress, σ_t is the stress that can be added to the state of cross bending stress σ_b such that unrestricted yielding takes place in the tension bands. Under these assumptions the von Mises yield condition assumes the form

$$\sigma_t^2 + \sigma_b^2 - \sigma_t \sigma_b - \sigma_Y^2 = 0.0 \ . \qquad [5.13]$$

In the postbuckling range of model SR1 the cross bending moments along the buckle crests are close to the yield moment and do not vary significantly. For example at element 22, Gauss point 2/2 the bending moment is equal to 29.39N.mm/mm, which is the yield bending moment for the thin part of the cylinder. Using von Mises yield criterion (Eq. 5.13) one obtains the yield tension stress distribution across the thickness shown in Fig. 5.20b. The maximum allowable average tension stress across the thickness is equal to 226MPa (Fig. 5.20c). The yield bending moment is present at all buckle crests and valleys.

It is reasonable to consider that far in the postbuckling range the folding continues and that along the buckle crests a plastic bending moment is obtained. Using von Mises yield criterion (Eq. 5.13) one obtains the yield tension stress distribution across the thickness shown in Fig. 5.21b. In this situation the maximum allowable average tension stress across the thickness is 150MPa (Fig. 5.21c).

The variation of the cross bending moments across the buckles is that of Figs. 5.22, which has plastic moments or yield moments at crests and valleys. In this case the average tension field yield stress varies periodically across the width of the tension field. The average is 225MPa($0.75\sigma_Y$) for cross plastic moments and 261MPa($0.875\sigma_Y$) for cross yield moments. Thus it is suggested that Eq. 5.9 be multiplied by a new factor, μ, to account for the cross bending moment effect,

$$V_t = \frac{1}{2}\,\mu\,\eta\,\sigma_Y\,R\,t\,\sin 2\zeta\,(1 - \cos\alpha). \qquad [5.14]$$

Similarly Eq. 5.12, assumes the form,

$$C = \mu\,\eta\,\sigma_Y\,R\,t\,\alpha\cos^2\zeta, \qquad [5.15]$$

with η varying from 0.5 to 1 and μ from 0.875 to 0.75.

The compressive force, C, is carried by two helix compression struts, top and bottom, inclined at an angle ζ to the generator, as one can see in Fig. 5.23. The vertical projections of these struts are inclined at an angle γ to the horizontal, having the value,

$$\gamma = \text{atan}\{\frac{R}{L}(1 + \cos\alpha)\}. \qquad [5.16]$$

If C is the horizontal projection of the force in the

tension bands along the X axis, described by Eq. 5.15, then C_T and C_B, the strut forces projection on the X-Z plane, have similar expressions to those of Eqs. 5.2 and 5.3,

$$C_T = - \frac{M_L\ C}{(M_L - M_R)\ \cos\gamma}, \qquad [5.17]$$

and,

$$C_B = \frac{M_R\ C}{(M_L - M_R)\ \cos\gamma}. \qquad [5.18]$$

The inclined struts contribute to the total shear, such that

$$V = T \sin\zeta + C \tan\gamma. \qquad [5.19]$$

The banding takes place at the begining of the horizontal postbuckling path and at this stage according to the numerical analyses, the yield cross bending moment is present at crests and valleys.

For the upper bound η is equal to 1.0 and μ is equal to 0.75, which corresponds to fully active tension field and plastic cross bending moments at the buckle crests and valleys. In this case using σ_Y equal to to 301MPa, α equal to 122^0, ζ equal to 27^0, γ equal to 13.23^0, and the values of L and R used to calculate ζ, V_t according to Eq. 5.14 equals 20200N and the horizontal projection C equals 55100N. Thus the total shear for half the cross section equals 33100N according to Eq. 5.19. The corresponding values of the

compression top and bottom forces, calculated using Eqs. 5.17 and 5.18, with γ equal to 13.23^0 are 32800N and 23700N respectively, which correspond to an average compression stress of 290MPa at the top compressive strut, averaged over a width equal to 1/4 of half the circumference.

The lower bound corresponds to η equal to 0.5 and μ equal to 0.875 i.e., banded tension field and yield cross bending moments. In this case using the same values for σ_y, a, t, R, L, used in this chapter, and γ equal to 13.23^0, V_t is equal to 11767N and C is equal to 32140N. Thus, the total shear according to Eq. 5.19 is 19500N. The values of C_T and C_B, using Eqs. 5.17 and 5.18, are 19157N and 13834N, respectively. The average compressive stress at the top strut is 169MPa, considering 1/4 of half the circumference in compression.

The value of observed total shear, V, equal to 20270N for half a cylinder is clearly close to that of the lower bound. According to Stephens et al (1982) the local buckling stress for an axially loaded cylinder, having the geometry of model SR1, is 168 MPa. This reference suggests the use of the same procedures to predict bending buckling of thin-walled cylinders. In the finite element analysis performed on model SR1 the maximum observed compression stress is 280 MPa at the left top of the thin cylinder, element 25 (see Fig. 2.1), which is significantly higher than the local buckling under axial load value of 168MPa,

predicted by Mok and Elwi (1986), according to Stephens et al (1982). However, model SR1 is practically a perfect shell, and the local buckling axial compressive stress is very sensitive to the level of the initial imperfections. In the case of transverse shear loading there are stress gradients in both the circumferential direction and along the generator. These gradients may increase the local compression buckling stress value. Thus, at this level of the stress no sign of local buckling is present.

5.6 Existing Banded Tension Field Capacity of the SR1 Model

To evaluate the contribution of the banded tension field to shear capacity Eq.5.7 is directly integrated considering different yielding tension stresses across three different tension bands,

$$V_t = \frac{1}{2}\{R\,\sigma_{t1}\,t\,\sin 2\zeta\,(-\cos\phi)\Big|_{0.164a}^{0.327a} + R\,\sigma_{t2}\,t\,\sin 2\zeta\,(-\cos\phi)\Big|_{0.471a}^{0.758a}$$

$$+ R\,\sigma_{t3}\,t\,\sin 2\zeta\,(-\cos\phi)\Big|_{0.815a}^{1.02a}\}, \qquad [5.20]$$

where σ_{ti} are the average principal tension stresses across the tension bands.

The horizontal projection of the diagonal tension band forces is calculated using a modified form of Eq. 5.12 with different values of tension stresses across the tension bands, as follows,

$$C = R\,\sigma_{t1}\,t\cos^2\zeta\;\phi\Big|_{0.164a}^{0.327a} + R\,\sigma_{t2}\,t\cos^2\zeta\;\phi\Big|_{0.471a}^{0.758a}$$

$$+ R\,\sigma_{t3}\,t\cos^2\zeta\;\phi\Big|_{0.815a}^{1.02a} \qquad [5.21]$$

The evaluation of the shear V_t was carried out, for the SR1 model, along the third column of the Gauss points of elements 13 to 18 at the postbuckling load levels 20.27 kN and 20.50 kN, respectively. The first value, corresponds to the begining of the horizontal postbuckling path and the last one is the last performed analysis in postbuckling. It is noted that the tension bands are fully plastified at a level lower than the uniaxial yield stress of 301 MPa, due to the presence of a compression stress component. From the outputs σ_{t1} is equal to 134.5 MPa, σ_{t2} is equal to 230 MPa, and σ_{t3} is equal to 207 MPa. These values represent the average tension stress across the tension bands. The same values of R, t, ζ as those used above are used in the evaluation of V_t and C.

For both load points V_t, for half the cylinder is equal to 14100 N and the total horizontal projection, C for half the cylinder is around 30316 N. The rest of the shear up to 20.27kN is carried by the inclined compression bands. Using Eqs. 5.17 to 5.18 and the values of bending moments from Fig. 5.18, the value of top compression force, C_T is 20281N, the value of the bottom compression force, C_B is 14643N, and the corresponding compressive stresses are 179MPa, 129MPa, respectively, (only from existing tension field) for a top

or bottom compression area equal to 1/4 of half the circumference.

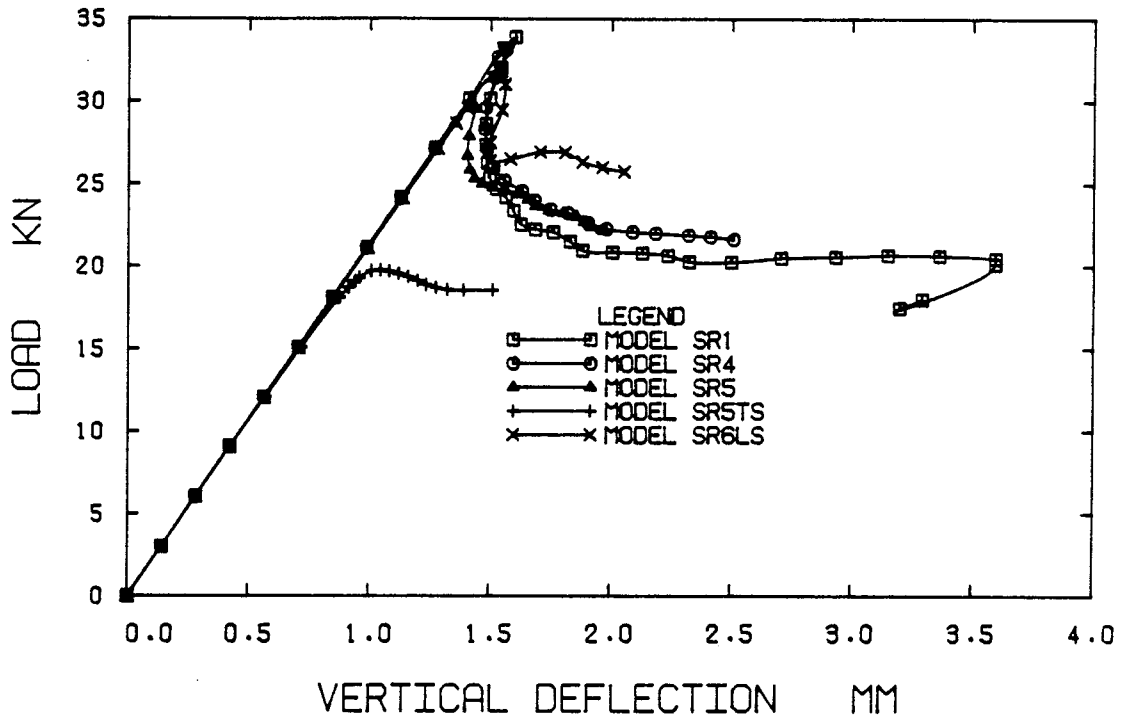

Figure 5.1 Equilibrium Paths for SR Series

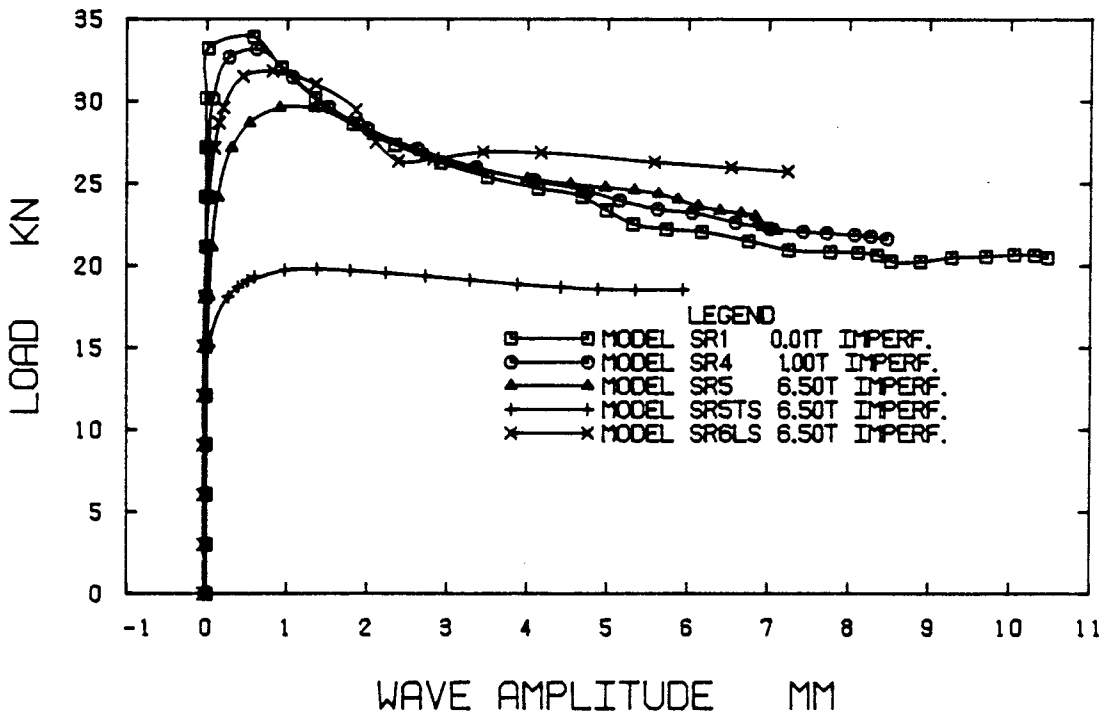

Figure 5.2 Postbuckling Response of SR Models under Transverse Shear

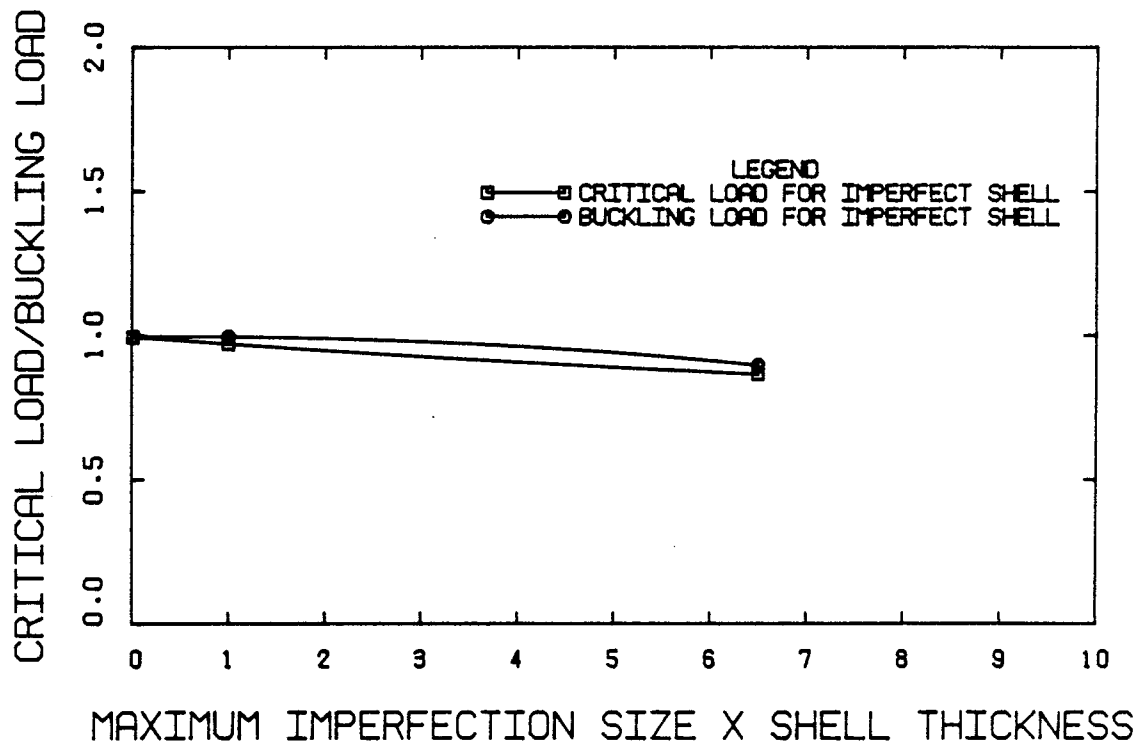

Figure 5.3 Imperfection Sensitivity of the Cylinder under Transverse Shear Loading

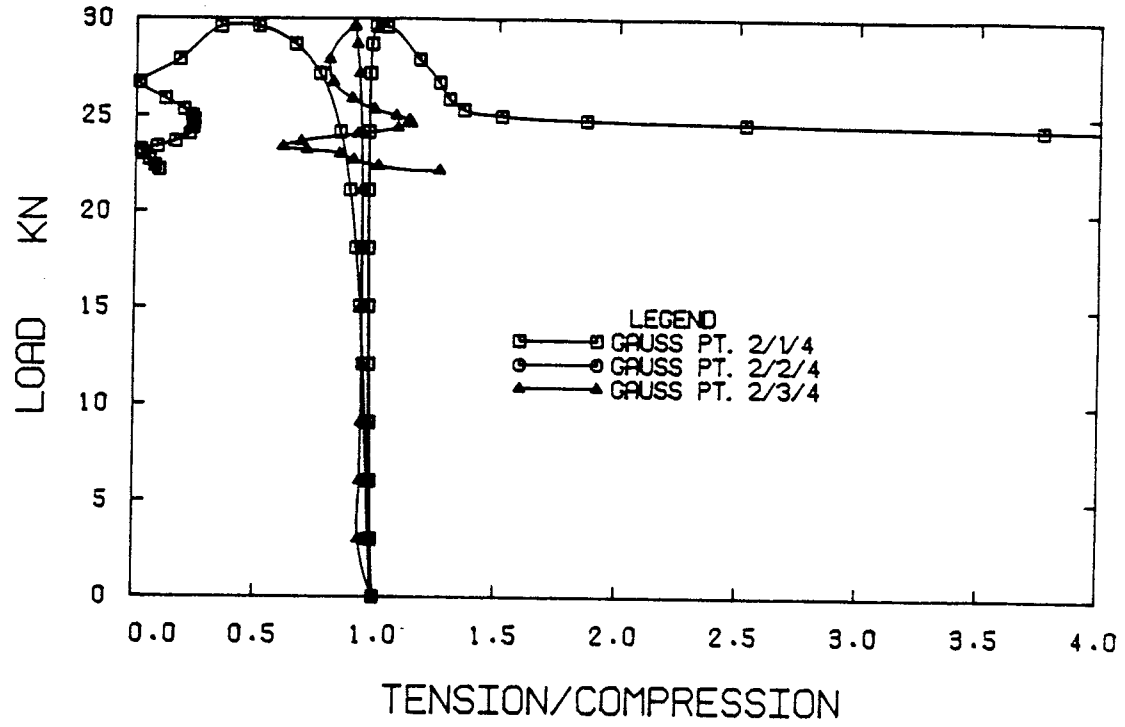

Figure 5.4 Load versus Tension to Compression Stress Ratio for Element 21, SR5 Model

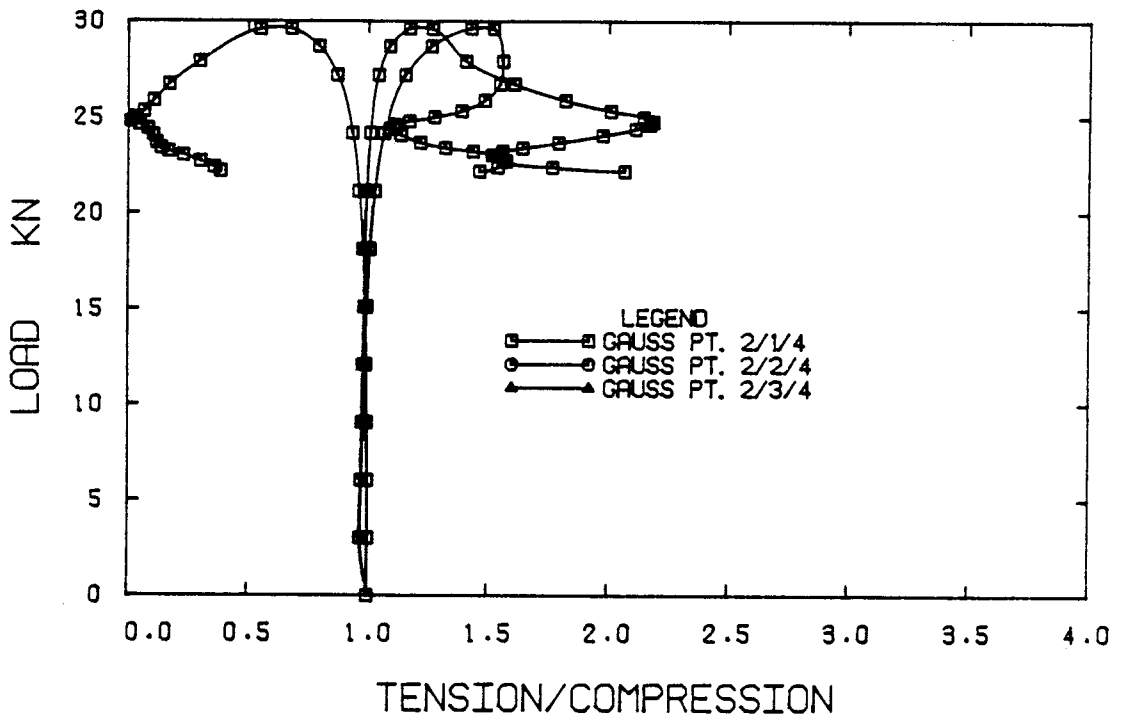

Figure 5.5 Load versus Tension to Compression Stress Ratio for Element 22, SR5 Model

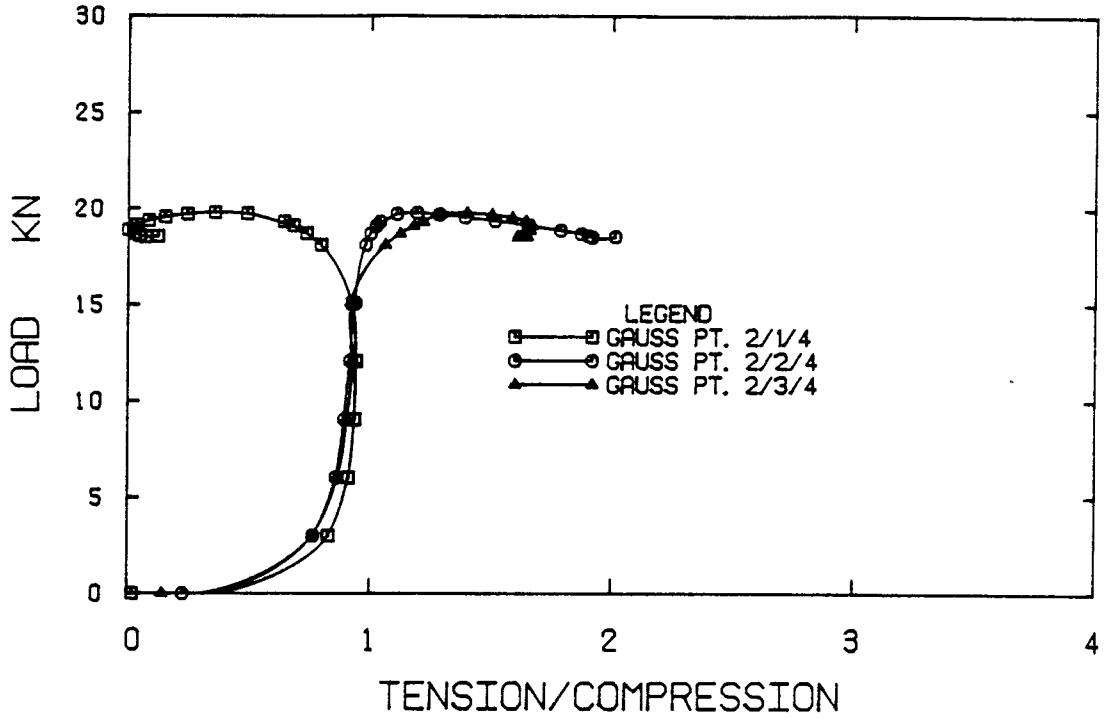

Figure 5.6 Load versus Tension to Compression Stress Ratio for Element 22, SR5TS Model

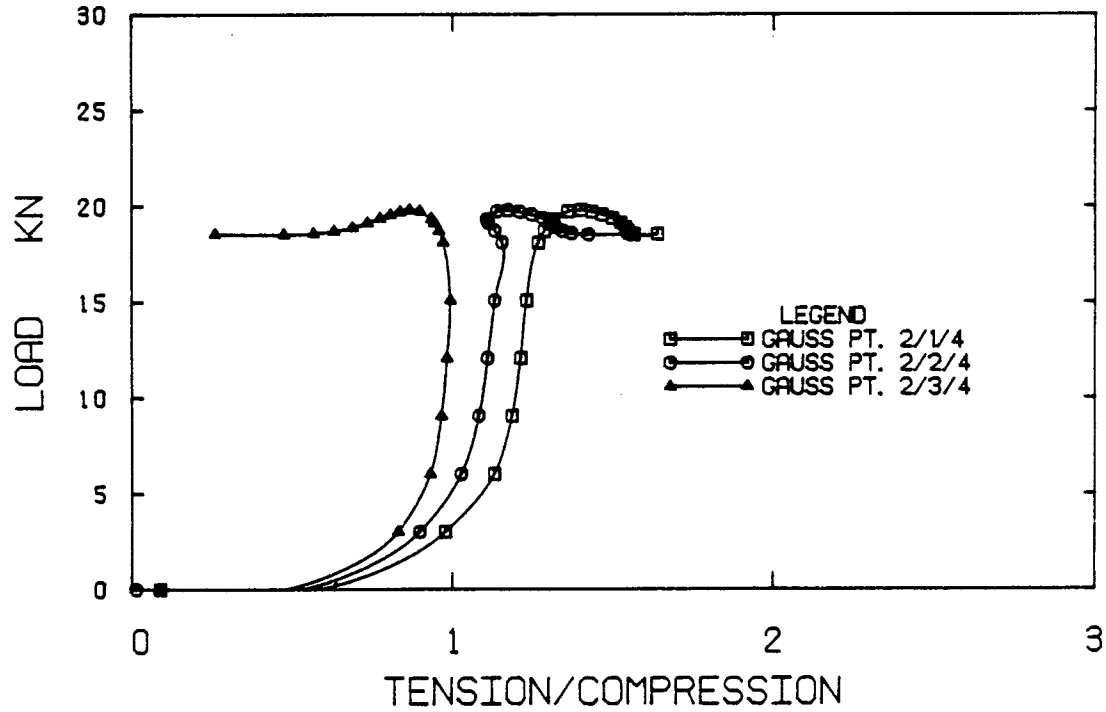

Figure 5.7 Load versus Tension to Compression Stress Ratio for Element 23, SR5TS Model

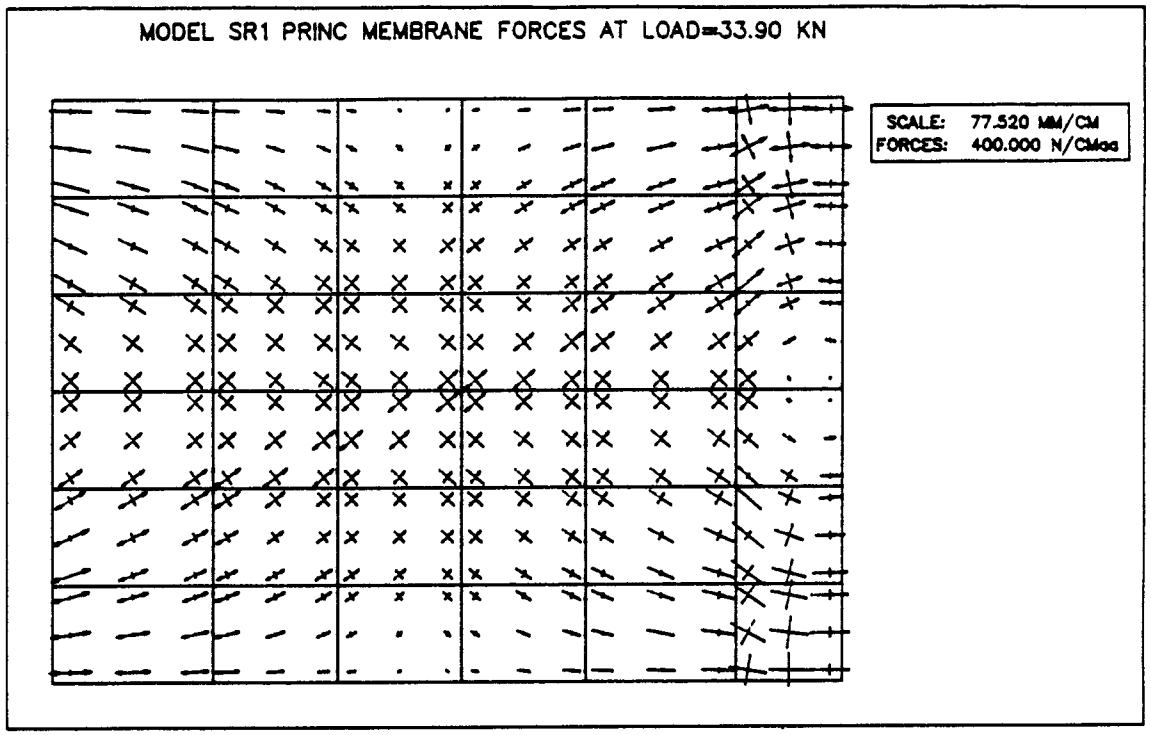

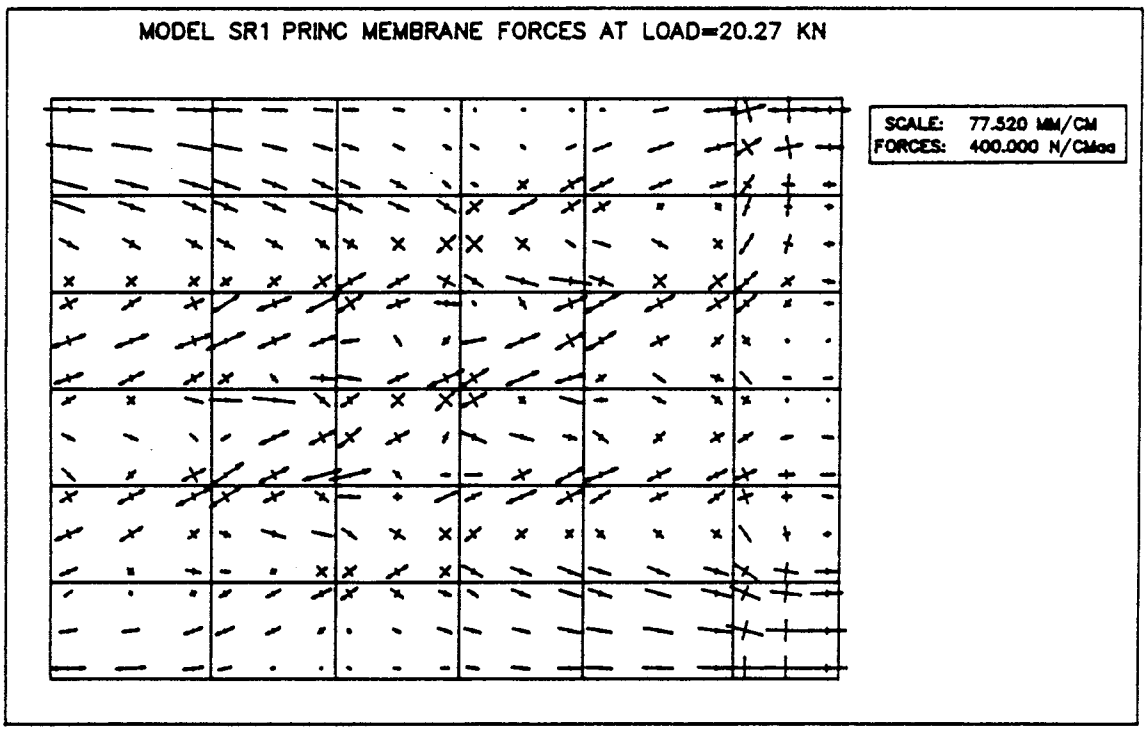

Figure 5.8 Principal Membrane Forces for SR1 Model

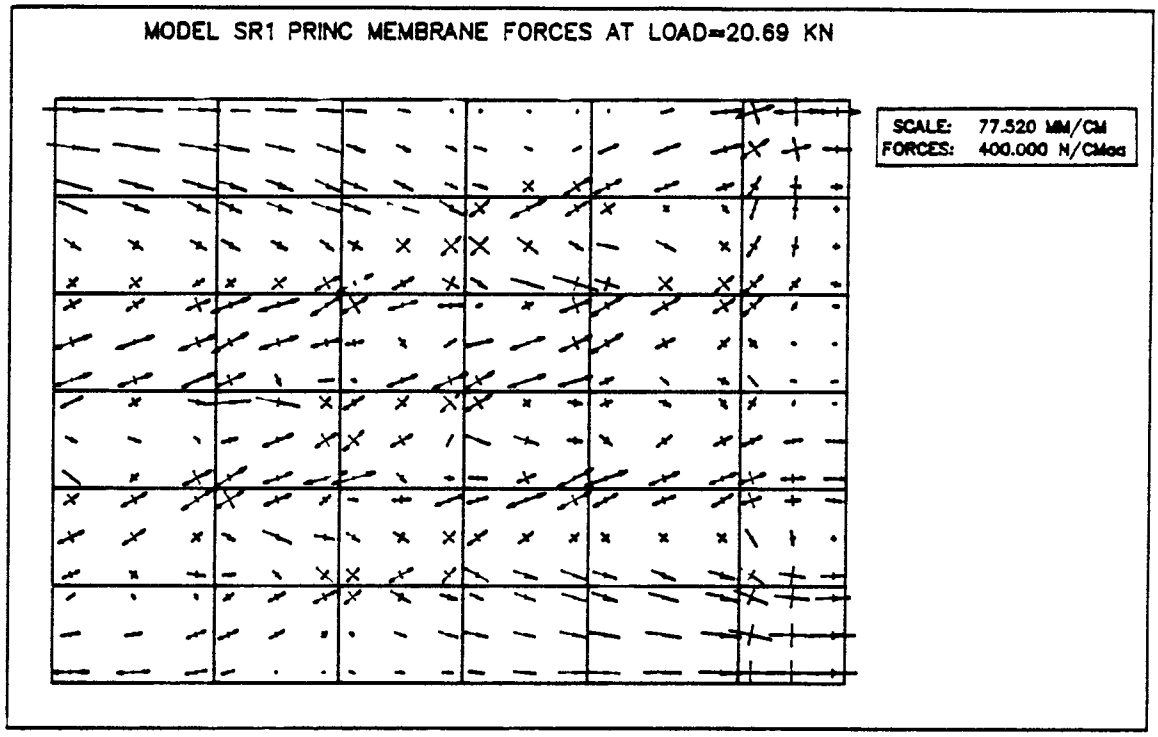

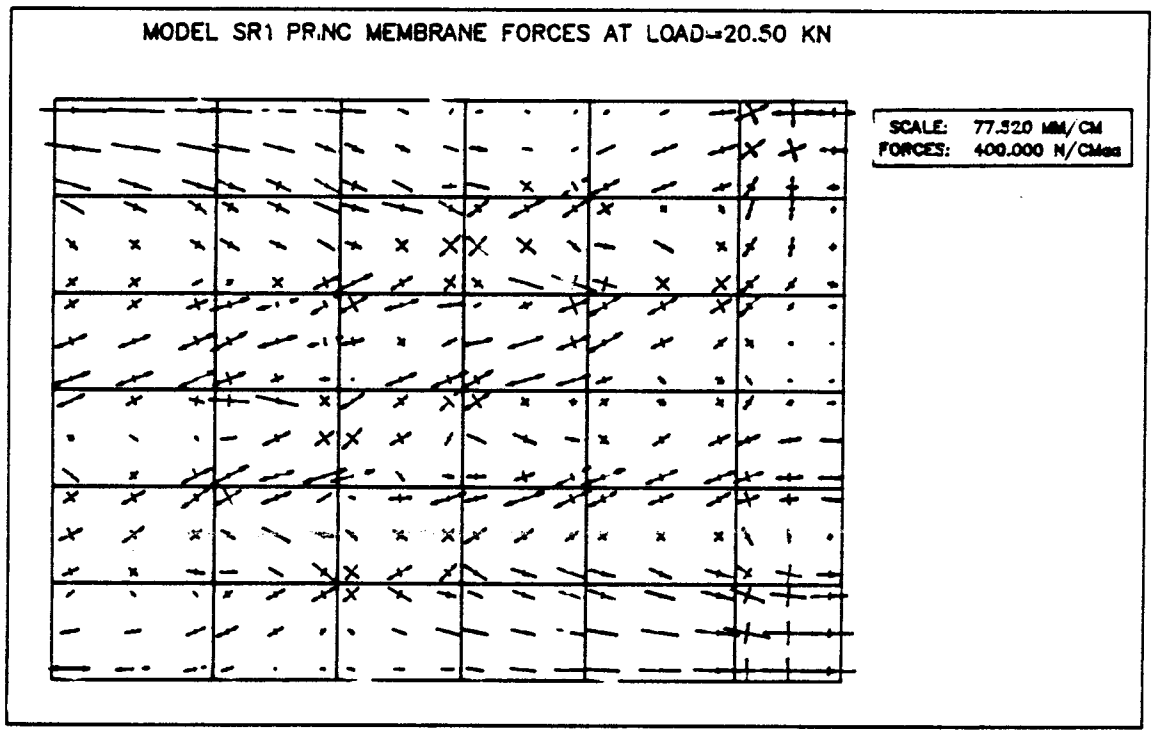

Figure 5.9 Principal Membrane Forces for SR1 Model

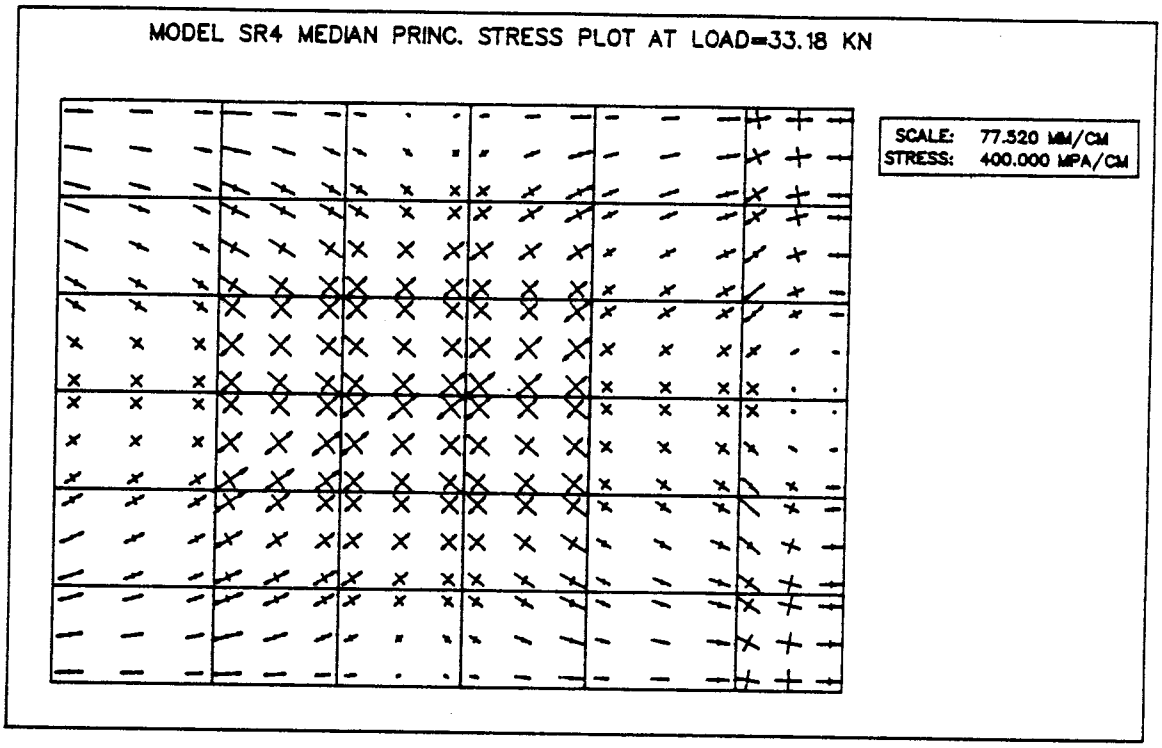

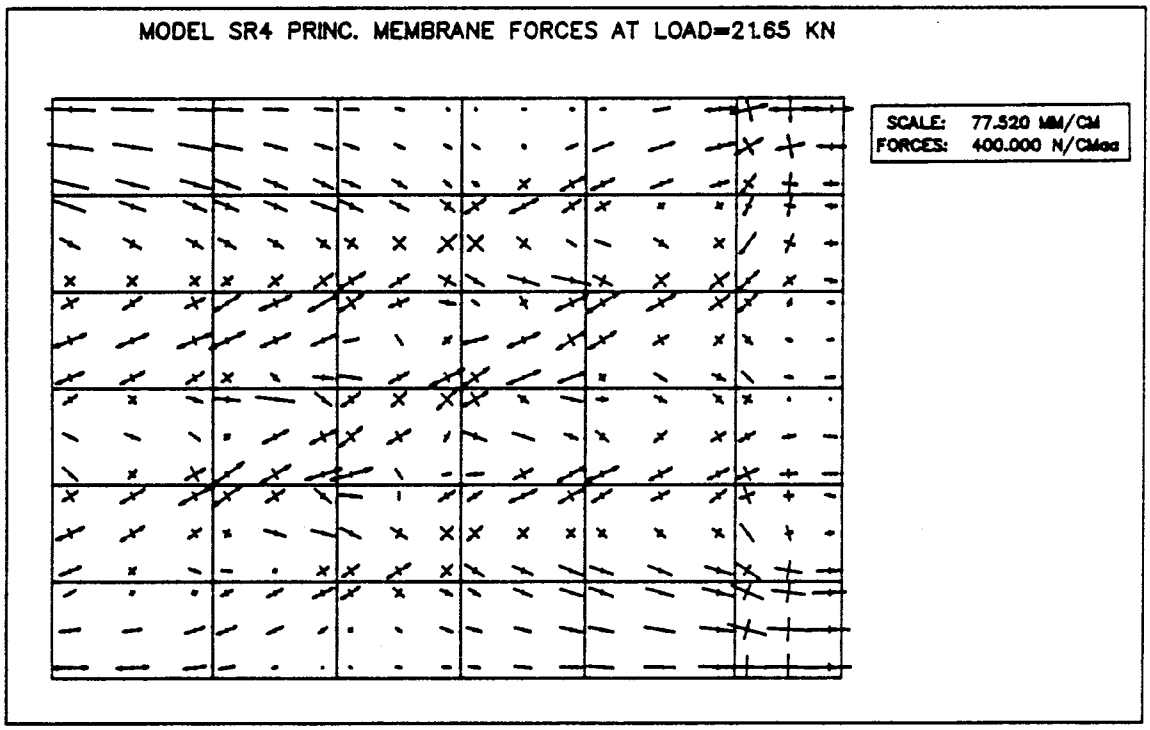

Figure 5.10 Principal Membrane Forces for SR4 Model

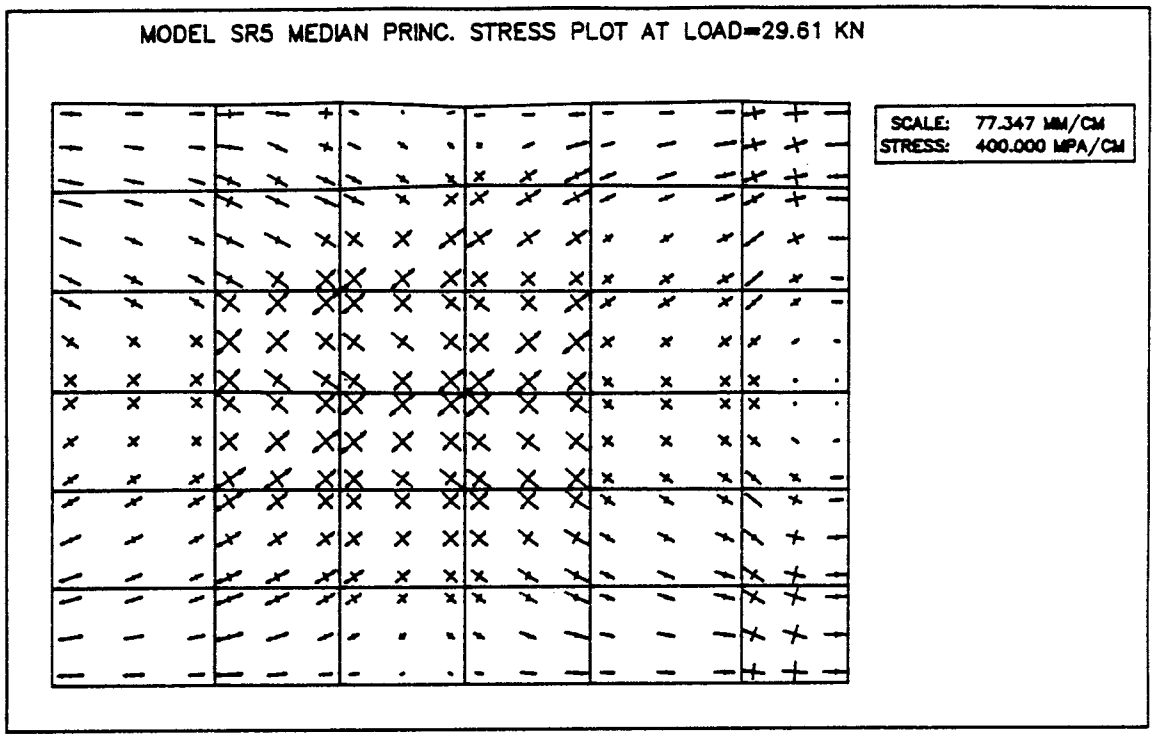

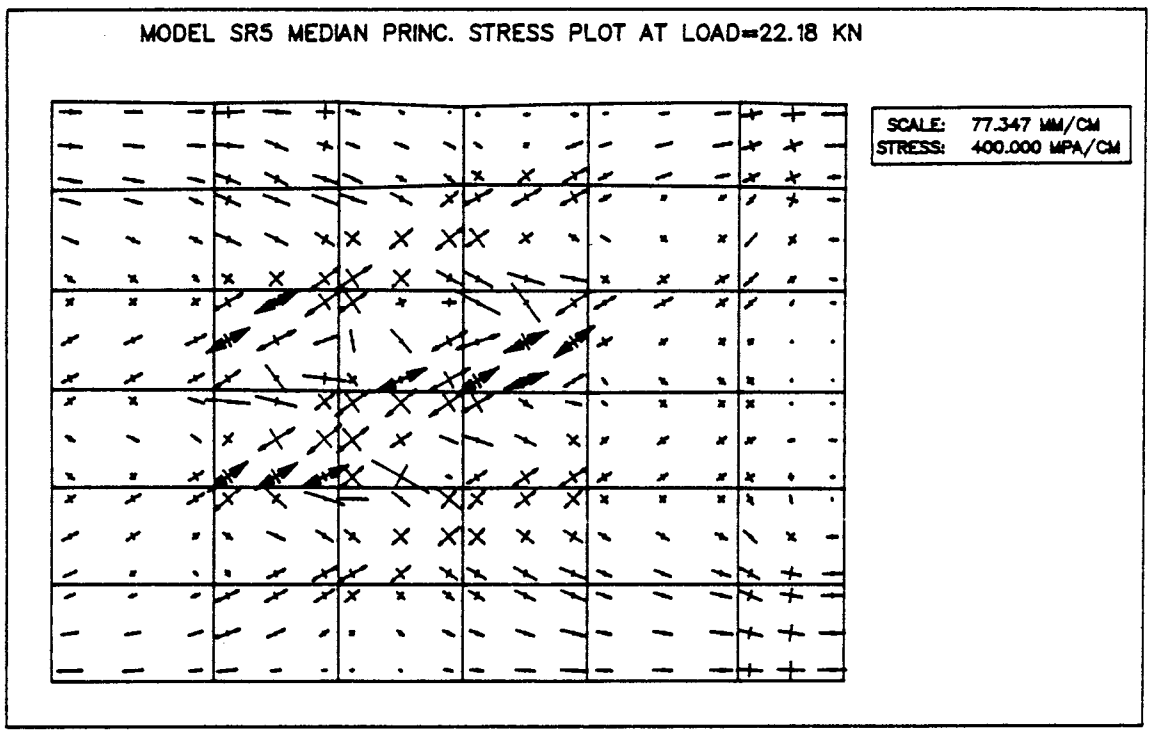

Figure 5.11 Median Principal Stresses for SR5 Model

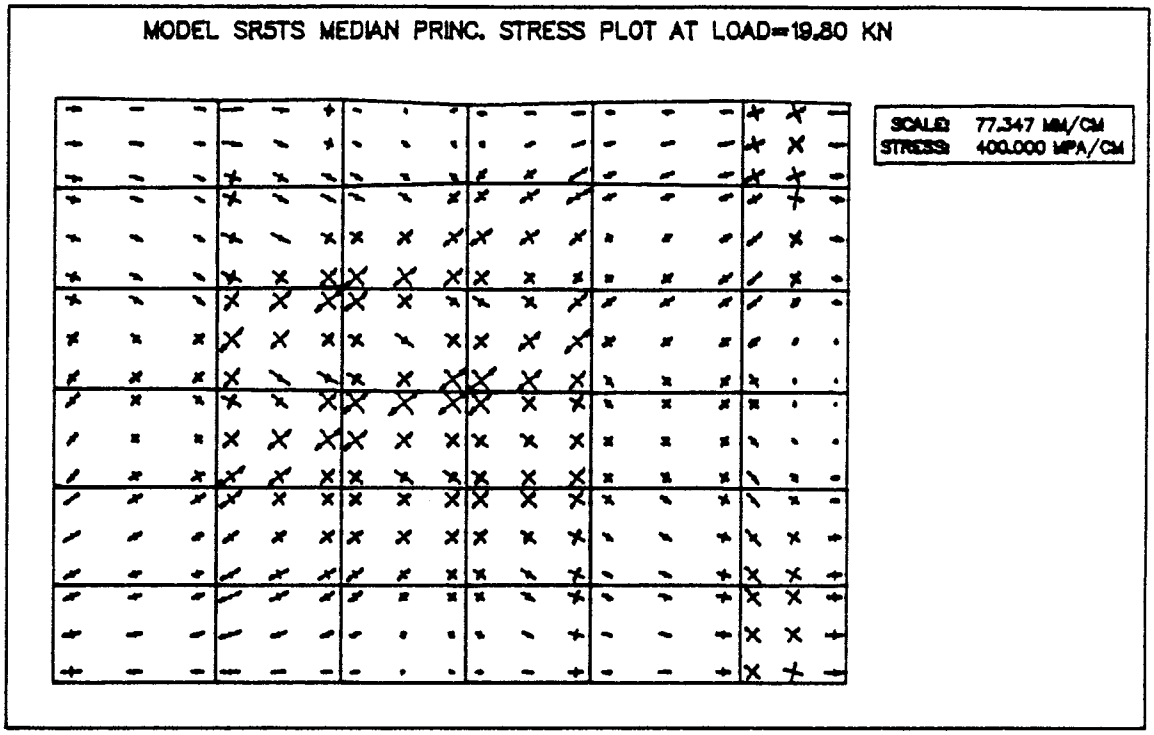

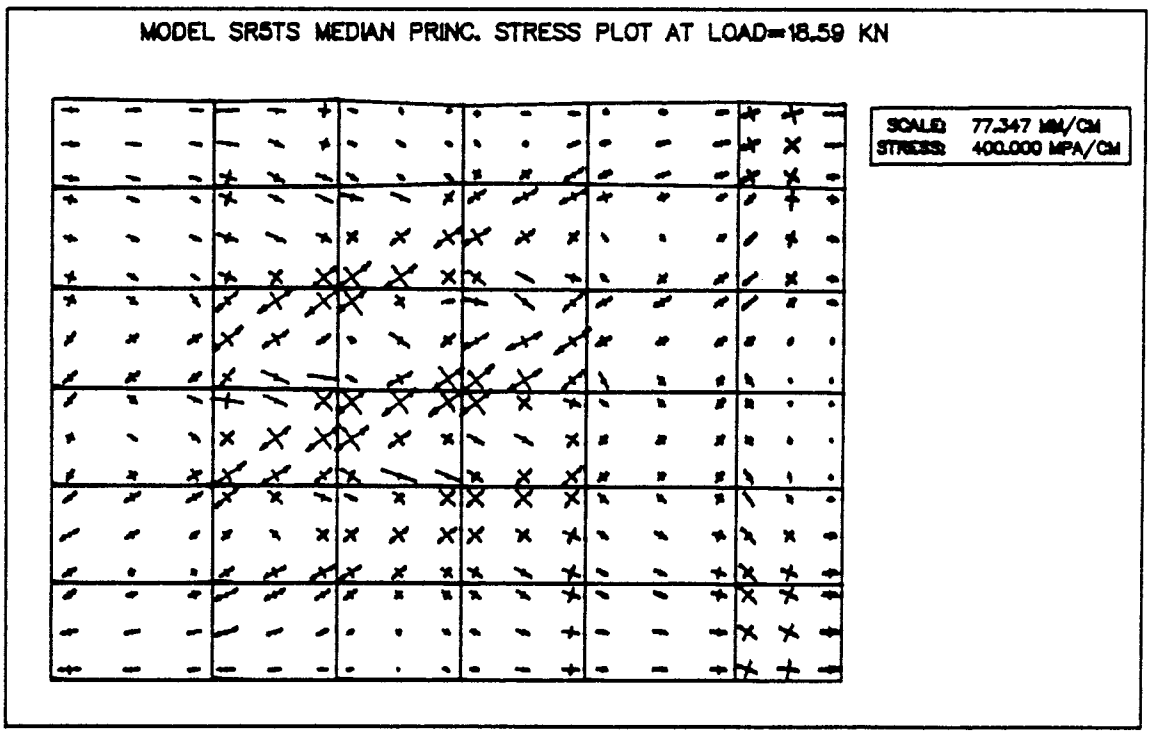

Figure 5.12 Median Principal Stresses for SR5TS Model

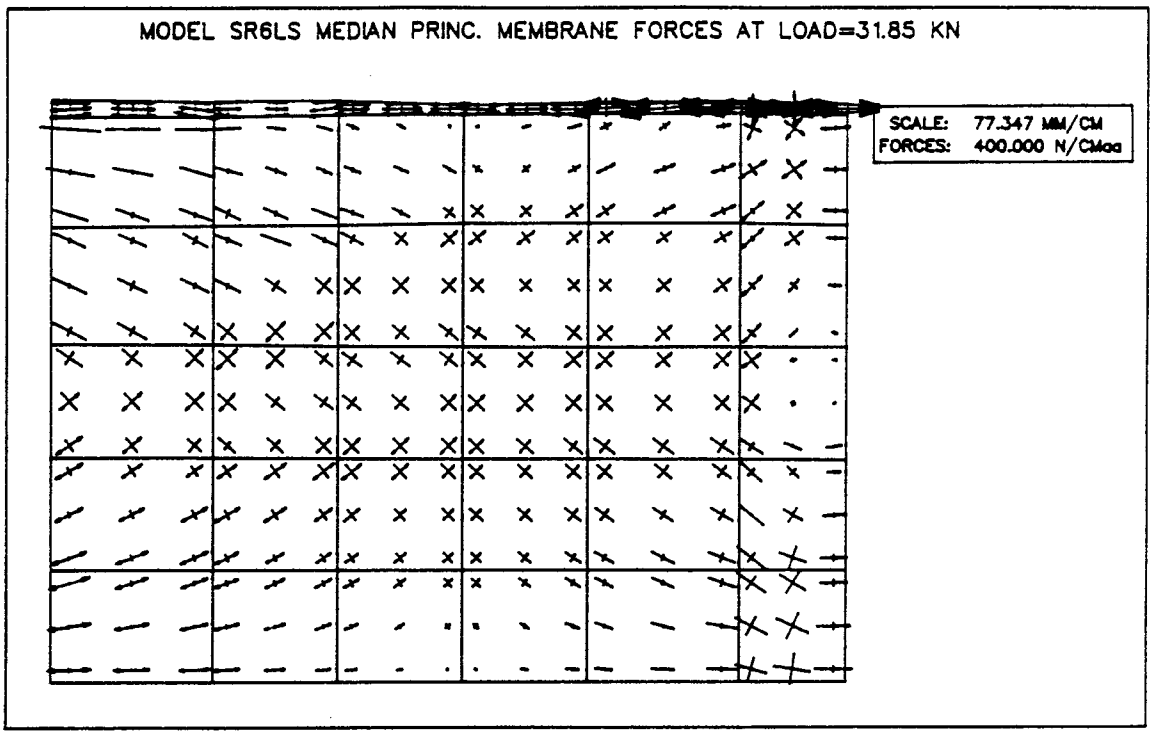

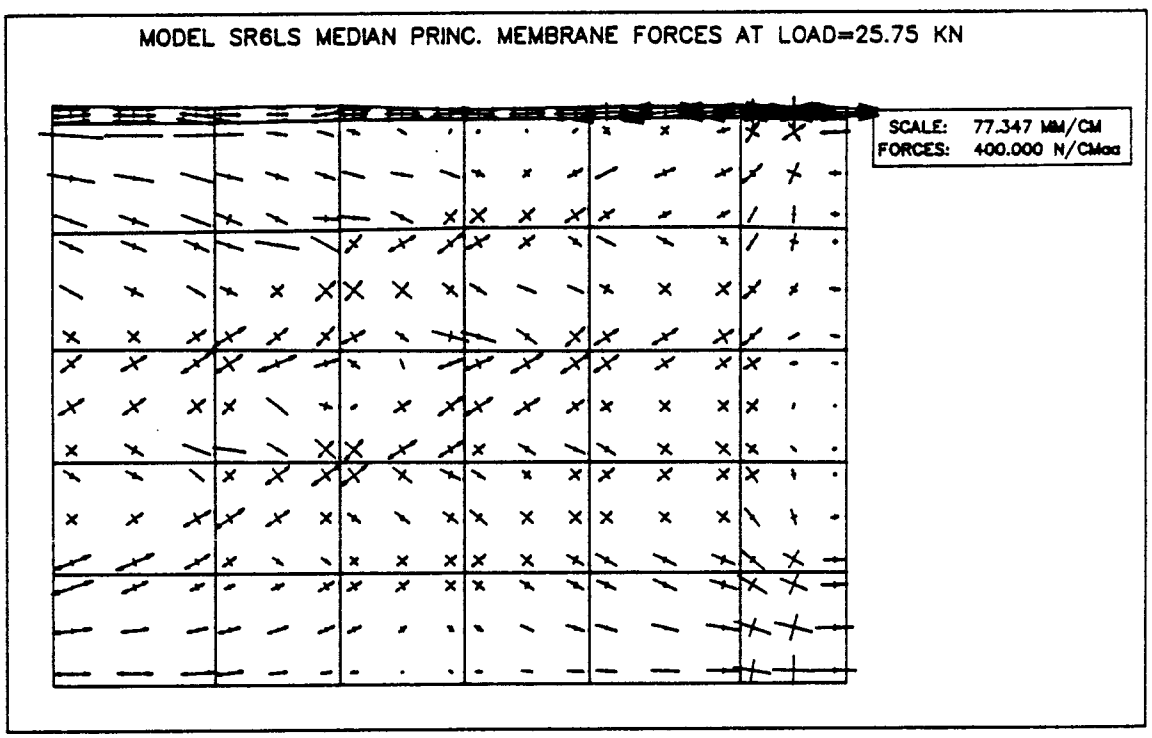

Figure 5.13 Principal Membrane Forces for SR6LS Model

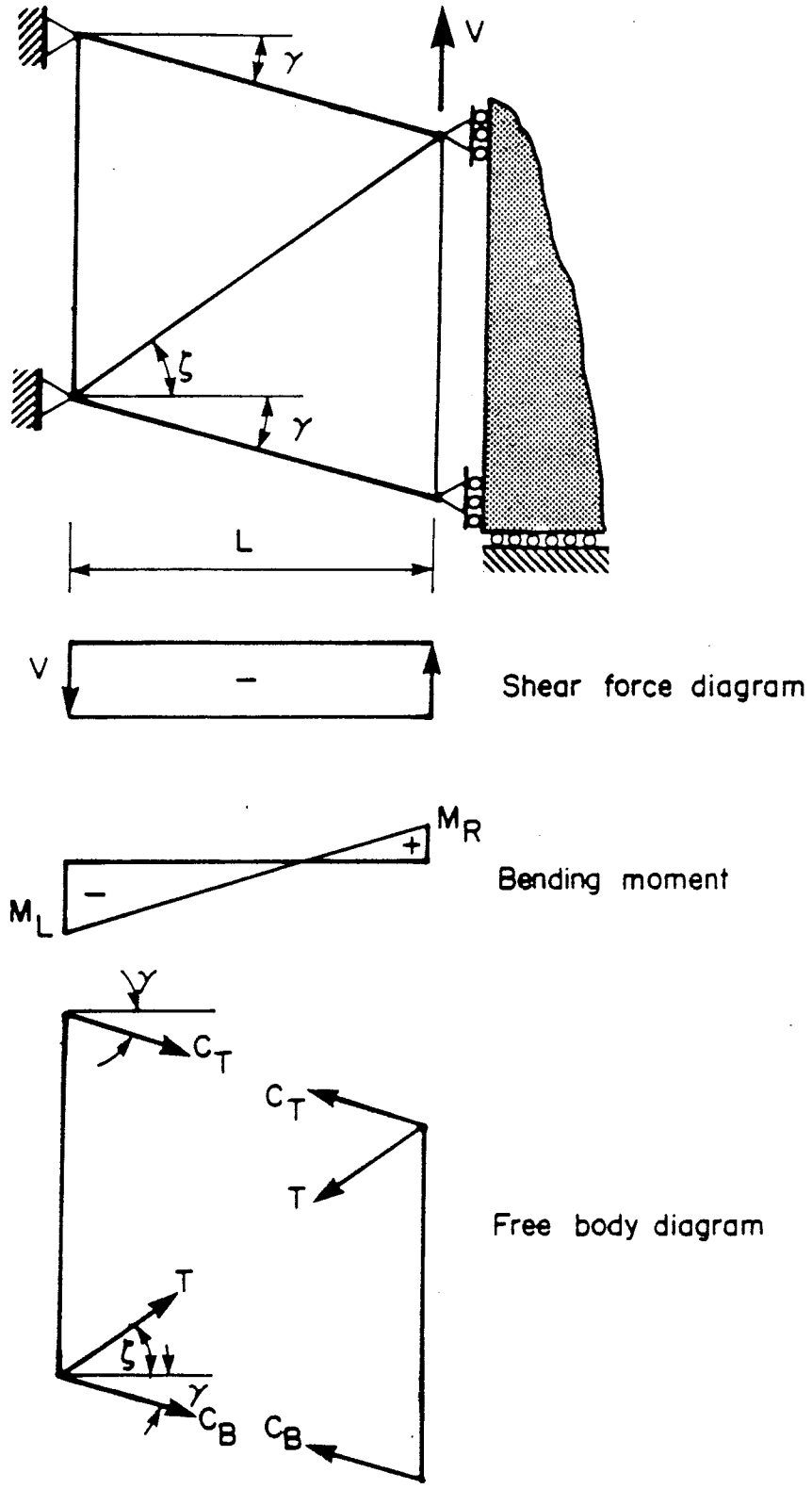

Figure 5.14 Truss Panel

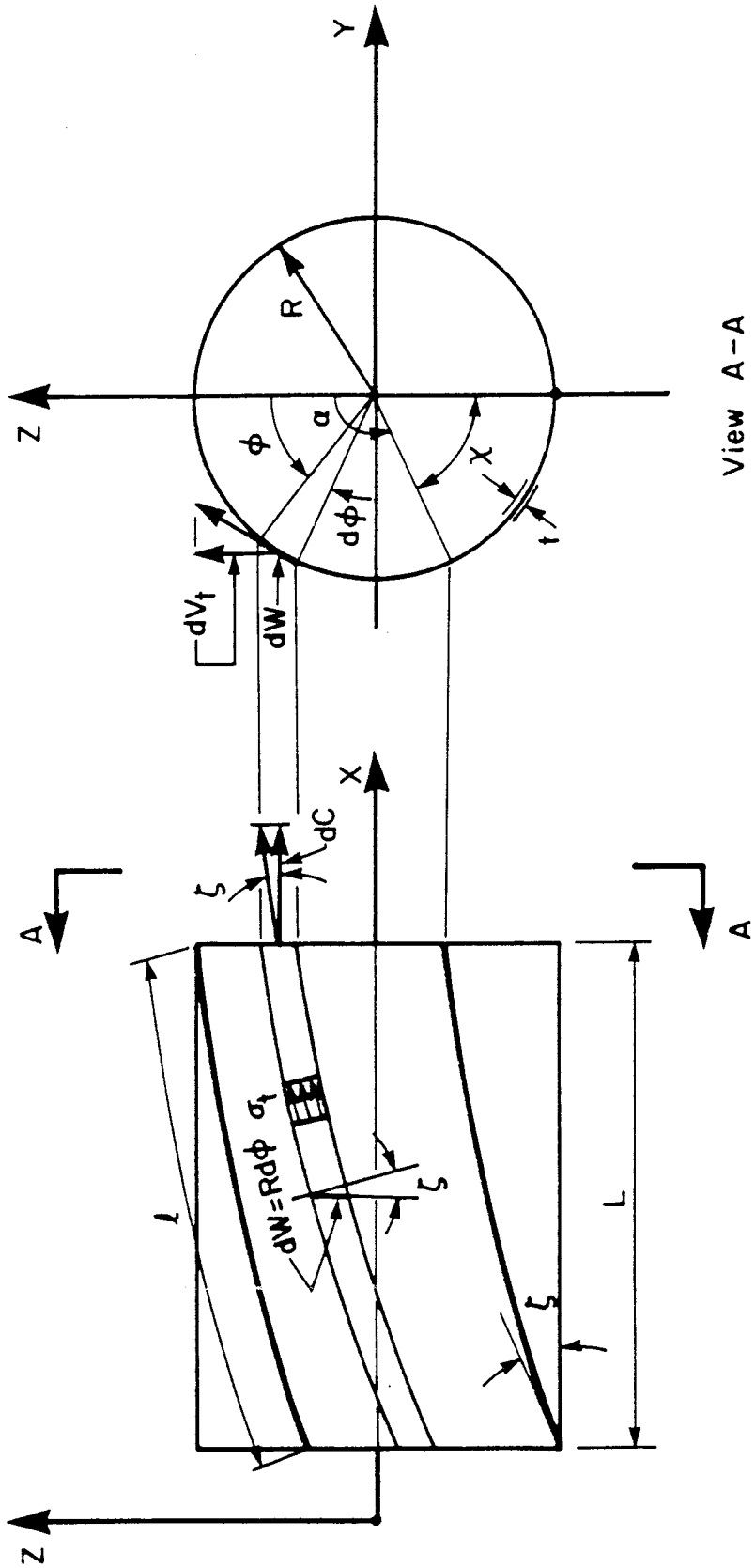

Figure 5.15 Tension Field elements

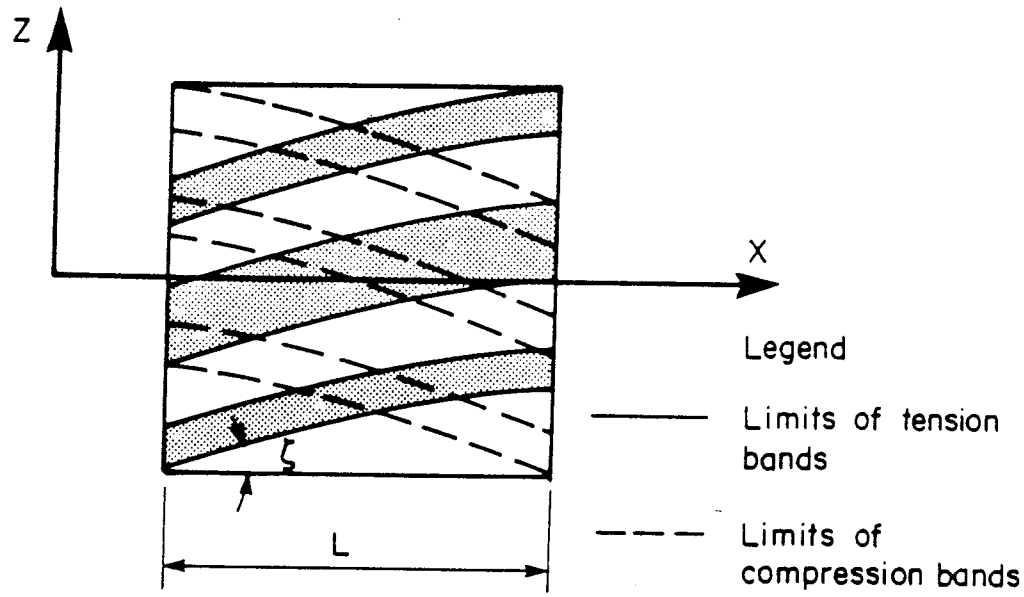

Figure 5.16 Tension and Compression Bands on Cylinder

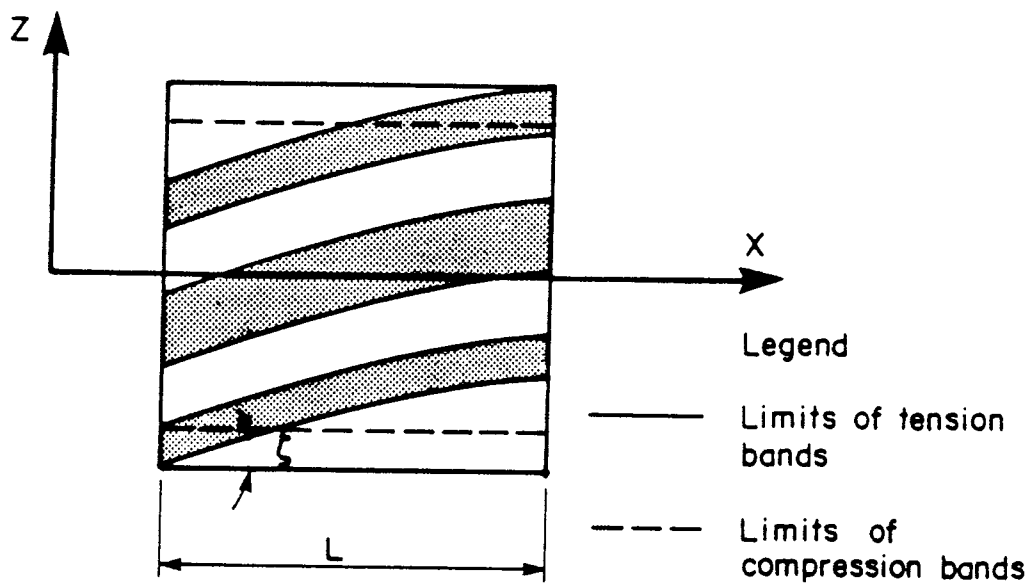

Figure 5.17 Tension Bands on Cylinder

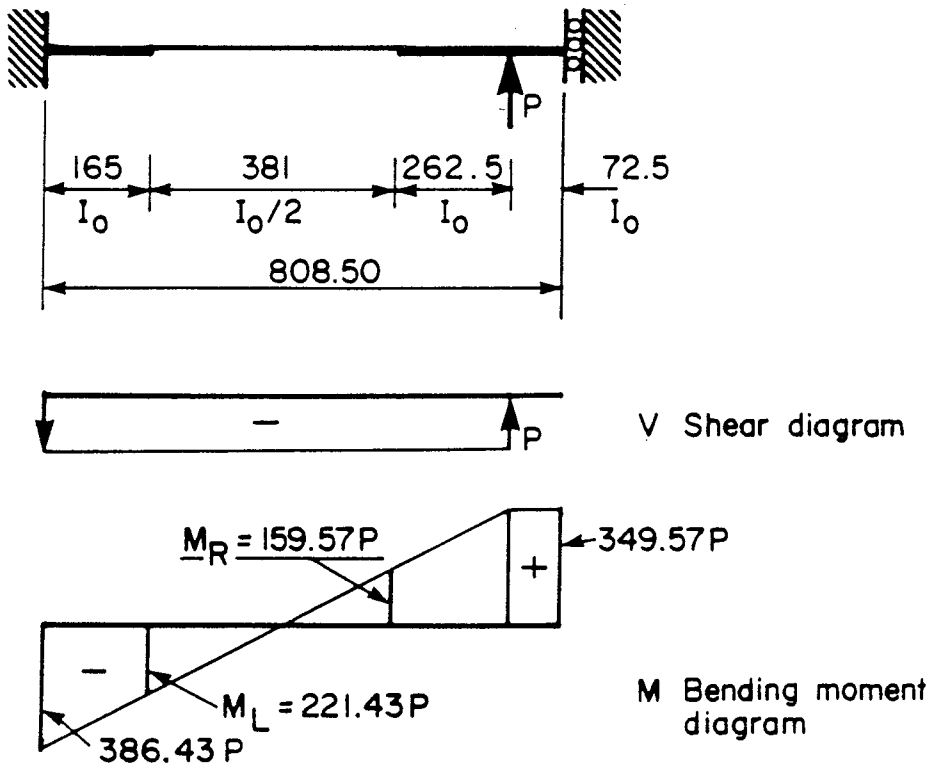

Figure 5.18 Shear and Bending Moment Diagram for Cylinder in Beam Behavior

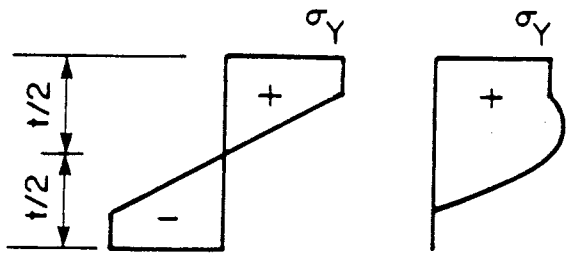

σ_b Stresses due to cross bending

σ_t Tension stress distribution due to cross bending stress presence

Figure 5.19 Tension Stresses Distribution due to Cross Elasto-Plastic Bending Moment

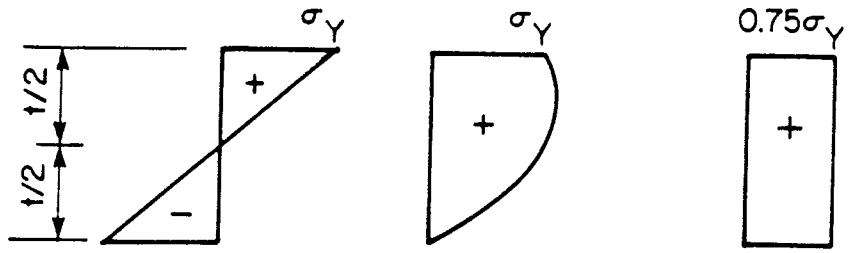

(a) Stress from yield bending moment

(b) σ_t yield tension stress

(c) σ_t average tension stress

Figure 5.20 Tension Stress Distribution due to Cross Yield Moment

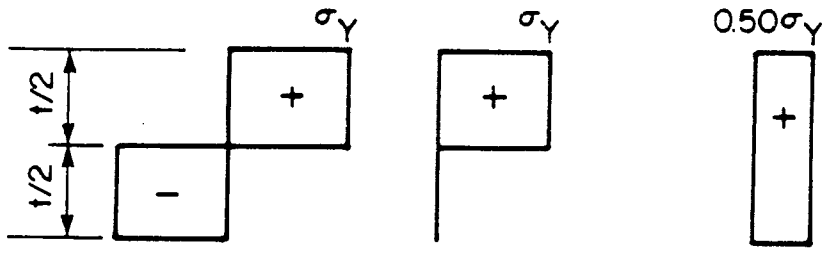

(a) Stress from plastic bending moment

(b) σ_t yield tension stress

(c) σ_t average tension stress

Figure 5.21 Tension Stress Distribution due to Cross Plastic Moment

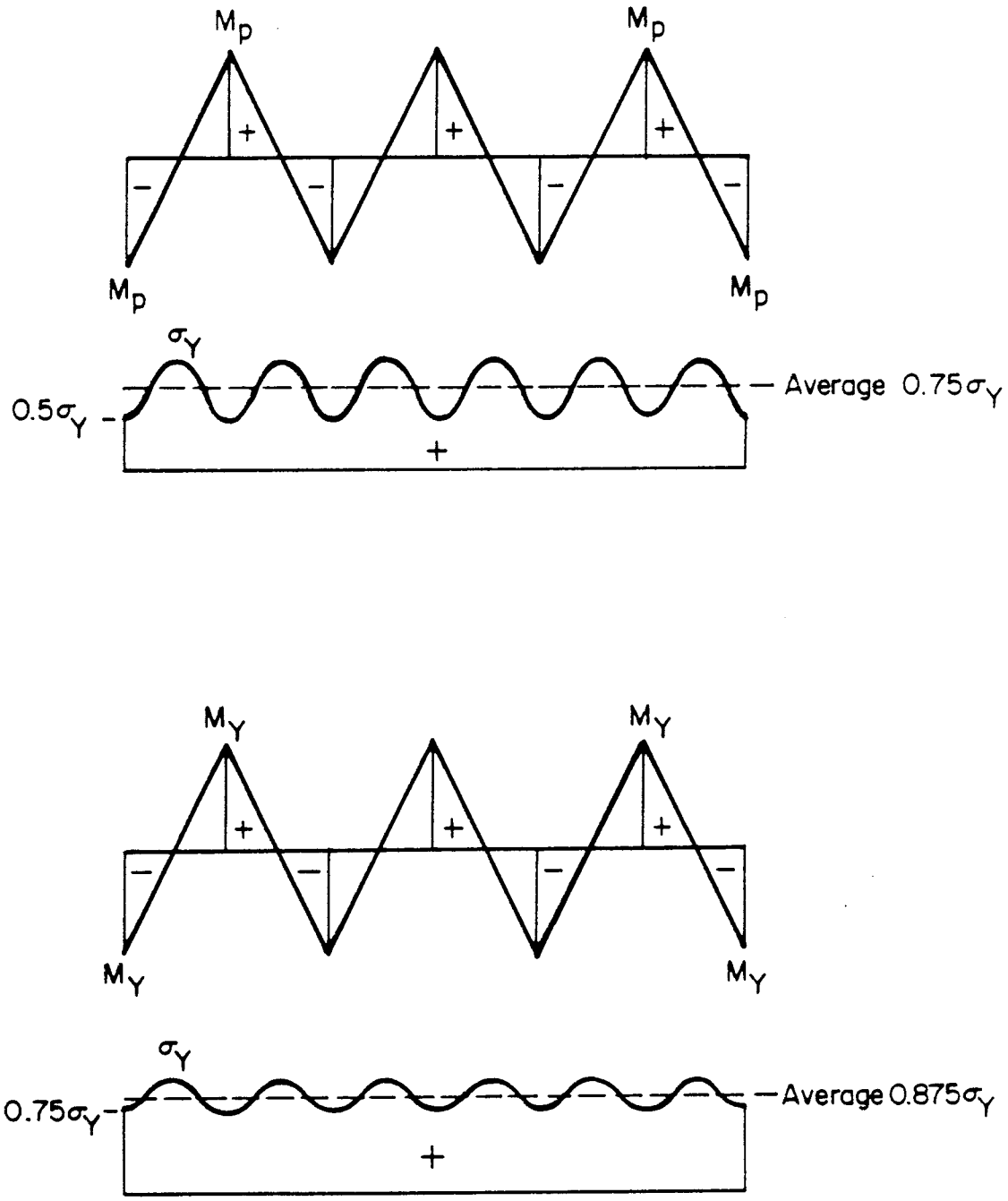

Figure 5.22 Yield Tension Stress Distribution Across the Width of Tension Field

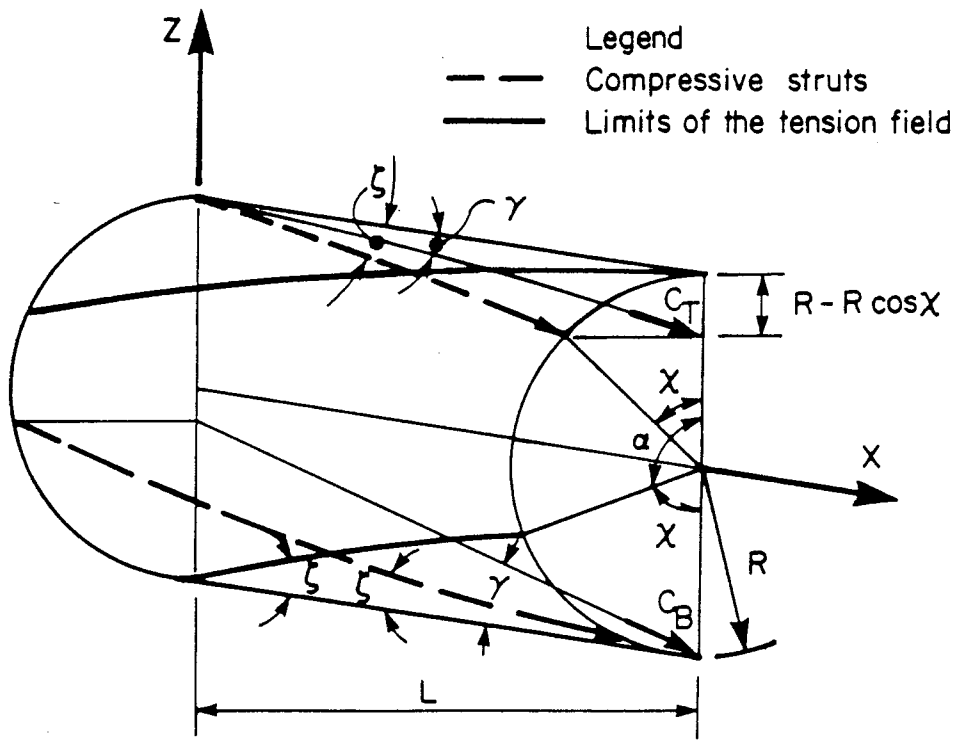

Figure 5.23 Compressive Struts and the Tension Field

6. Summary and Conclusions

The equilibrium path of the cylinders under transverse shear was investigated both in the prebuckling and postbuckling range taking into consideration initial measured imperfections, initial residual stresses due to longitudinal seam weld shrinkage, and initial locked-in stresses due to the cold forming. The numerical analyses were performed using the finite element program NISA80. Boundary conditions, the geometry, and the mesh are similar for all analyses.

Based on the results obtained from numerical analysis the following observations are made,

1. The stiffness of the prebuckling path is independent of the magnitude of the initial measured imperfection (in the limits of 0.01 to 6.5 times the cylinder thickness), the initial residual stress due to the longitudinal weld shrinkage and the locked-in state of stress due to the cold forming.
2. The magnitude of the initial imperfections has a small, about 10% influence on the magnitude of the critical load.
3. A locked-in stress has a significant influence on the magnitude of the critical load.
4. Unloading after reaching the critical load is very sharp, except for the model with initial locked-in circumferetial stress due to the cold forming. For this case the unloading is mild.

5. For all effects the postbuckling paths converge to a common postbuckling path, which decreases and stabilizes rapidly on a constant lower load level. This means that in the postbuckling range the equilibrium is stable at a lower load level than the critical load.
6. The magnitude of the load on the stable postbuckling equilibrium path is independent of the size of the initial measured imperfections, and initial residual stresses. The initial locked-in stresses reduce slightly the load level of the stable postbuckling path.
7. A shear buckling mode is displayed at the critical load by all models, regardless of the size of the initial measured imperfections or the distribution of the initial residual or locked-in stress.
8. The begining of the local buckling of the compressed areas of the cylinder due to the bending moments and the tension field development is noted only in models with relatively large initial measured imperfections (6.5 times the cylinder thickness).

Based on an investigation of the carrying capacity of the postbuckling path the following is stipulated,

1. In the postbuckling range a supporting capacity similar to a truss panel is developed. A diagonal tension field develops, having a helical shape on the cylinder. The lower bound of the tension field is defined by a banded tension field, composed by yielded tension bands

separated by unloaded bands due to the shear buckling occurence. The contribution to the total shear of the inclined compressive struts must be considered. The upper bound of the tension field is defined by a sinusoidal yield stress variation across the whole tension field width.

2. The horizontal projection of the tension field is shared by the top and bottom parts of the cylinder, which are the top and bottom chords of an analogue truss panel. The sharing ratio is a function of the panel end moments.
3. The tension stress which develops on the diagonal tension field is limited by the cross bending moments developed by the buckle formation, and by the compression capacity of the top or bottom parts of the cylinder which share the horizontal projection of the tension field resultant.
4. Equations have been developed to describe the helix angles ζ and α in terms of R, radius, and L, length and the tension field capacity as well. Total shear capacity was also derived in terms of the tension field capacity and the contribution of the corresponding compression struts.

Bibliography

Arbocz, J. and Babcock C. D., "Prediction of Buckling Loads Based on Experimentally Measured Initial Imperfections", Buckling of Structures, Edited by Budiansky, B., Springer-Verlag, New-York, 1976, pp 295-296.

Bailey, W. R. and Kulak, G. L., "Flexural and Shear Behavior of Large Diameter Steel Tubes", Structural Engineering Report No. 119, University of Alberta, Department of Civil Engineering, November 1984.

Basler, K., "Strength of the Plate Girders in Shear", Journal of the Structural Division, Proceedings of the ASCE, Vol. 87, No ST7, October 1961, pp 151-180.

Batdorf, S. B., Stein, M. and Schildcrout, M., "Critical Shear Stress of Curved Rectangular Panels", NACA, TN No. 1348, Washington D.C., May 1947.

Brush, D. O., Almroth, B. O., "Buckling of Bars, Plates and Shells", McGraw-Hill Book Company, 1975.

Bushnell, D., "Computerized Buckling Analysis of Shells", Martinus Nijhoff Publishers, Kluwer Academic Publishers Group, Boston, 1985.

Chen, W. F. and Han, J. D., "Tubular Members in Offshore Structure", Pitman Advanced Publishing Program, Boston, 1985.

Chiarito, P. T., "Some Strength Tests of Stiffened Curved Sheets loaded in Shear", NACA ARR No. L5B10, 1945.

Crisfield, M. A., "Incremental/Iterative Solution Procedures for Nonlinear Structural Analysis", Int. Conf. Num.

Meth. for Nonlinear Problems, Swansea, September 1980.

Donnell, L. H., "Stability of Thin-Walled Tubes under Torsion", NACA Rep. 479, 1933.

Esslinger, M. and Geir, B., "Postbuckling Behavior of Structures", Springer-Verlag, New-York, 1975.

Fersht, S. R., "Buckling of Cylindrical Shells with Random Imperfections", Thin-Shell Structures, Theory, Experiment and Design, Edited by Fung, Y. C. and Sechker, E. E., Prentice-Hall, Inc., Englewood Clifs, N. J., 1974.

Flügge, W., "Stresses in Shells", Springer-Verlag, New-York, 1973.

Flügge, W., "Die Stabilität der Kreiszylinderschale", Ing.-Arch., Vol. 3, 1932, pp 463-506.

Galletly, D. G., Blachut, J., "Plastic Buckling of Short Cylindrical Shells Subjected to Horizontal Edge Shear Loads", Journal of Pressure Vessel Technology, Transactions of the ASME, Vol. 107, May 1985, pp 101-107.

Häfner, L., Ramm, E., Sättele, J. M., and Stegmüller, H., "NISA80 - Programmdokumentation - Programmsystem. Bericht des Institut für Baustatik, Univesrsität Stuttgart, 1981.

Hutchinson, W. J. and Koiter, W. T., "Postbuckling Theory", Applied Mechnics Reviews, December 1970, Vol23, pp 1353-1366.

Hutchinson, J. W., "Post-bifurcation Behavior in the Plastic

Range", J. Mech. Phys. Solids, Vol 21, 1973, pp 163-190.

von Karman, T. and Tsien, S. H., "The buckling of Thin Cylindrical Shells under Axial Compression", J. Aeron. Sci. 8, 1941, pp 303-312.

Koiter, W. T., "On the Stability of Elastic Equilibrium", Thesis, 1945, English Translation, Air Force Flight Dyn. Lab. Tech. Rep. AFFDL-TR-70-25, 1970.

Kuhn, P. and Levin, L. R., "An Empirical Formula for the Critical Shear Stress of Curved Sheets", NACA ARR No. L5A05, 1945.

Lay, M. G., "Structural Steel Fundamentals", Australian Road Research Board, Sidney, 1982.

Love, A. E. H., "A Treatise on the Mathematical Theory of Elasticity", Dover Publications, New-York, 1944.

Lorenz, R., "Die nichtachsensymmetrische Knickung dünnwanger Hohlzylinder", Phys. Z., Vol. 13, 1911, pp 241-260.

Lundquist, E. E., "Strength Tests of Thin-Walled Duraliminum Cylinders in Torsion", NACA TN No. 427, Washington D. C., 1932.

Lundquist, E. E., "Strength Tests of Thin-Walled Duraluminum Cylinders in Pure Bending", NACA TN No. 479, Washington D. C., 1933.

Lundquist, E. E., "Strength Tests of Thin-Walled Duraluminum Cylinders in Combined Transverse Shear and Bending", NACA TN No. 523, Washington D. C., 1935.

Masubuchi K., "Analysis of Welded Structures Residual Stress, Distortion, and Their Consequences", New-York,

1980.

Masubuchi K., "Analytical Investigation of Residual Stress and Distortions due to Welding", Welding Journal, Vol. 39, 1960.

Mok, J. and Elwi, A. E., "Shear Behavior of Large Diameter Fabricated Steel Cylinders", Structural Engineering Report No. 136, Department of Civil Engineering, University of Alberta, Edmonton, Alberta, Canada, June 1986.

von Mises, R., "Der kritische Ausendruck zylindrischer Rohre", Z. Ver. Deutsch. Ing., Vol. 58, 1914, pp 750-755.

Morton, J., Murray, R. P. and Ruiz, C., "Effect of Imperfections on the Buckling Pressure of Complete Spherical Shells", and "Buckling of Spherical Storage Tanks under Vertical and Lateral Acceleration", Stabilty Problems in Engineering Structures and Components, Edited by Richard, H. J. and Stanley, P., Applied Science Publishers Ltd., London, 1979, pp 137-157.

Nagaraja, R. N. and Tall, L., "Residual Stress in Welded Plates", Welding Journal, Vol. 40, 1961, pp 468s-480s.

Queener, C. A. and De Angelis, R. J., "Elastic Springback and Residual Stresses in Sheet Metal Formed by Bending", ASM Transaction Quarterly, Vol. 61, 1961, pp 757-768.

Rafael, N., "Effect of Normal Pressure on the Critical Shear Stress of Curved Sheet", NACA RB, January 1943.

Rafael, N., Sandlin, C. W., "Effect of Normal Pressure on

the Crtitical Compressive and Shear Stress of Curved Sheets", NACA ARR No. L5B10, 1945.

Ramm, E., "A Plate/Shell Element for Large Deformations and Rotations", Formulations and Computational Algorithms in Finite Element Analysis, Edited by Bathe, K. J., Oden, J. T., Wunderlich, W., MIT Press, Boston, 1977.

Ramm, E., "Strategies for tracing the Nonlinear Response near Limit Points", Nonlinear Finite Element Analysis in Structural Mechanics, edited by Wunderlich, W., Stein, E., and Bathe, K. J., Proceedings of the Europe-U.S. Workshop, Ruhr-Universität Bochum, Germany, July 28-31, 1980.

Riks, E., "An Incremental Approach to the Solution of Snapping and Buckling Problems", Int. J. Solids and Structures, Vol. 15, 1979, pp. 529-551.

Sabir, A. B., "Large Deflection and Buckling Behavior of a Spherical Shell with Inward Point Load and Uniform External Pressure", J. Mech. Eng. Sci., Vol. 6, 1964, pp 394-404.

Schilling, C. G., "Buckling Strength of Circular Tubes", Journal of the Structural Division, Proceedings of the ASCE, Vol. 91, No. ST5, October 1965.

Schwerrin, E., "Die Torsions-Stabiltät des Dünnwandigen Rohres", Z. Angew. Math. Mech., Vol. 5, 1925, pp 235-243.

Stegmüller, H., "N I S A - Input Description", April 20, 1984.

Southwell, R. V., "On the Collapse of Tubes by External Pressure", Phil. Mag., Vol. 25, 1913, pp 687-698.

Stephens, M. J., Kulak, G. L. and Montgomery, C. J., "Local Buckling of Thin-Walled Tubular Steel Members", Structural Engineerig Report No. 103, Dept. of Civil Engineering, University of Alberta, February 1982.

Timoshenko, S. and Woinowski, K., "Theory of Plates and Shells, McGraw-Hill, New-York, 1959.

Wempner, G. A., "Discrete Approximations Related to Nonlinear Theories of Solids", Int. J. Solids and Structures, 7(1971), pp. 1581-1599.

Zienkiewicz, O. C. and Irons, B. M., "Matrix Iteration and Acceleration Process in Finite Element Problems of Structural Mechanics", Methods for Nonlinear Algebraic Equations, edited by P. Rabinovitz, Gordon and Breach, London, 1970, pp.183-194.

Yamaki, N., Naito, K. and Sato, "Buckling of Circular Cylindrical Shells under Combined Action of a Transverse Edge Load and Hydrostatic Pressure", Proceedings of the International Conference on Thin-Walled Structures, University of Strathclyde, Glasgow, April 1979.

Appendix A. Notes on Program NISA

Program NISA80 (Ramm, 1977, Häfner et al, 1981, Stegmüller, 1984) is a general nonlinear incremental structural analysis program using finite elements. It has a small displacement infinitesimal strain formulation capability as well as large displacement large strain formulations. The latter are reflected in total and updated Lagrangian formulations.

Material models include an elastic, an elastic-perfectly plastic, an elastic-plastic with strain hardening and a concrete orthotropic biaxial model.

The program can also perform continuous eigenvalue analysis on nonlinear element groups based on the current deformed configuration and stress state using the subspace iterative technique.

Incremental solution strategies are standard and modified Newton-Raphson (Zienkiewicz and Iron, 1970) and Riks-Wempner or constant-arc-length-method (Wempner, 1971, Riks, 1979, Crisfield, 1980, Ramm, 1980). Newton-Raphson (load control) methods diverge in the neighbourhood of limit or critical points, due to the singularity of the stiffness matrix at these points. The Riks-Wempner method (constant arc length) overcomes this problem allowing the equilibrium path to be traced beyond the limit point.

The program evaluates the length of the arc, based on initial displacement increments. However, this parameter can also be controlled by the user. This is important because in

the neighbourhood of the limit or critical points the calculated initial arc length (DS0I) is not suitable and must be reduced to account for the sever increase in the degree of nonlinearity of the problem investigated in this study. Another parameter which is helpful in tracing the equilibrium path is the relative tolerance (RTOL) used to measure equilibrium convergence.

In this investigation a total Lagrangian formulation with a 16 node degenarated shell element and an elastic-perfectly plastic material model were used.

The solution strategy varied with the movement along the equilibrium path. A modified Newton-Raphson method was generally suitable up to 70% of the limit load. Above this level standard Newton-Raphson method was used due to the nonlinear behavior of the structure. Close to and beyond the critical or limit point the constant-arc-length-method combined with standard Newton-Raphson was used. In addition to controlling the arc length (DS0I), the tolerance of convergence of the equilibrium equations (RTOL) was changed in order to reduce the number of the iteration for a displacement step. The convergence criterion compares the magnitude of the change in displacement increment with the magnitude of the accumulated displacement increment. On the prebuckling path the tolerance used was 0.001; giving convergence after 1 to 3 iterations. On the postbuckling path direct control of the arc length, in the sense of reducing it, and increasing the tolerance to a maximum value

of 0.02 gave a reasonable number of iterations per displacement step (4 to 10).

Appendix B. Comment on Comparison with Test Results

There are few experiments related to the thin cylinders under shear. Using Eqs. 5.14 to 5.16 and 5.19 to evaluate the postbuckling strength of different experiments one obtains the following results:

1. For the second shear specimen of Bailey and Kulak (1984) the total predicted shear force is 580kN which represents 85% of the experimental value, 680kN.
2. For the first shear experiment of Bailey and Kulak (1984) the total predicted shear capacity is 38kN which is 152% of the experimental value, 24kN. However, if the contribution to the shear of the compression struts is not considered the predicted shear capacity is close to the experimental value.
3. For the Galletly and Blachut (1985) experiment S3 the total predicted shear is 38kN which is 90% of the estimated experimental value, 41kN.

It must also be noted that:

1. The ultimate strength observed by Bailey and Kulak (1984) for the first shear specimen having the value of 29.4kN, is 74% of the limit load predicted by the numerical analysis of model SR5TS with locked-in stresses.
2. The stiffness of the first shear experiment of Bailey and Kulak (1984) is much less than that of the finite element model but matches the unloading and reloading

stiffness from the postbuckling path of the SR1 model, shown in Fig. 5.1. Therefore it is possible that the specimen was prebuckled in local compression due to the manufacturing procedure (weld succession and internal vacuum due to locking of hot air in a confined space).